Dissertation zur Erlangung des Doktorgrades
der Fakultät für Chemie und Pharmazie
der Ludwig-Maximilians-Universität München

Investigating the role of NMES1 as a modulator of innate immune responses

Julia Maria Kamper

aus

Rottenmann, Österreich

2024

TABLE OF CONTENTS

1. INTRODUCTION

1.1. The immune system

The arms race against pathogens is probably as old as the first living organisms. Many defense mechanisms are evolutionarily conserved, and some of them even exist in prokaryotes. For example, archaeal and bacterial genomes encode components of an antiviral signaling pathway termed cyclic nucleotide-based antiphage signaling system (CBASS), which constitutes the ancestor of the mammalian cGAS-STING pathway (see chapter 1.2.6) [1]. Whereas in unicellular organisms, defense is limited to cell-autonomous mechanisms, multicellular organisms have developed elaborate systems consisting of molecules, cell types and organs specialized in host defense. Importantly, the role of the mammalian immune system extends beyond pathogen removal [2]: It mediates a variety of responses, ranging from tissue remodeling to behavioral adaptations, which collectively aim to maintain or restore homeostasis [2, 3].

The vertebrate immune system can be divided into two branches: the innate and the adaptive immune system. All immune cells are derived from hematopoietic stem cells (HSCs), which reside in the bone marrow, but also can be found in the yolk sac and liver during embryonic development [4]. HSCs give rise to lymphoid and myeloid progenitor cells, which in turn give rise to the different immune cell subtypes [4]. The cells of the innate immune system include natural killer (NK) cells and innate lymphoid cells (ILCs), which are derived from lymphoid progenitor cells, and monocytes, macrophages and granulocytes (eosinophils, basophils and neutrophils), which are derived from myeloid progenitor cells [4]. In addition to these specialized immune cells, the epithelial cells of the skin and mucosa contribute to the innate immune response by providing a physical and chemical barrier to prevent infection [5]. Dendritic cells (DCs), which are mostly derived from myeloid progenitor cells, but can also be derived from lymphoid progenitor cells, are at the interface between the innate and adaptive immune system [4]. The cells of the adaptive immune system are T and B cells, which are derived from lymphoid progenitor cells [4]. T cells are further divided into subgroups based on the receptors ($\alpha\beta$ or $\gamma\delta$ T cell receptor) and co-receptors (e.g., CD4 or CD8) they express, and based on their effector function [6, 7]. There are two subgroups of $\alpha\beta$ T cells, namely cytotoxic T cells and T helper (T_H) cells [7]. The latter can be divided into subgroups based on their effector function, namely T_H1, T_H2 and T_H17 cells, T follicular helper cells (T_{FH}) and regulatory T cells (T_{reg}) [7].

The innate immune system constitutes the first line of defense against pathogens and plays an important role in initiating and steering innate immune responses [8]. Macrophages and DCs constantly surveil tissues for the presence of pathogens,

and proteins of the complement system circulate through the body, ready to be activated in case of an infection [4, 5]. Therefore, the innate immune response is rapidly initiated, usually within minutes to hours after infection [4]. A key prerequisite for the detection of pathogens is that the innate immune system needs to reliably distinguish self from non-self [8]. To meet this challenge, cells of the innate immune system are equipped with so-called pattern recognition receptors (PRRs), which will be described in more detail below [8]. These receptors collectively recognize a finite, predetermined set of ligands, predominantly evolutionarily conserved microbial components [4]. As briefly mentioned above, some molecular mechanisms of the innate immune system are conserved throughout all domains of life.

Macrophages and DCs, along with granulocytes, belong to the group of phagocytes, and can directly remove microbes or virus infected cells [9]. Phagocytes take up pathogens by receptor-mediated endocytosis, which are subsequently killed through the action of lysosomal enzymes, reactive oxygen species (ROS) and nitric oxide [9]. This process is supported by complement proteins, which opsonize pathogens and induce ROS production in phagocytes [5, 9]. In addition, the complement system can directly induce cell lysis of microbial pathogens through formation of a membrane-attack complex [5]. Upon pathogen recognition, innate immune cells also release cytokines and chemokines to recruit other immune cells to the site of infection [4].

For example, macrophages release CXCL8 to recruit neutrophils, which act as early responders in the infection [9]. On one hand, neutrophils phagocytose microbial pathogens, on the other hand, they can undergo NETosis – a specific form of cell death – to form neutrophil extracellular traps, which capture extracellular pathogens [9]. Furthermore, in the context of infection with intracellular pathogens, such as viruses, NK cells play an important role in the early immune response [4, 9]. NK cells sense changes in expression of cell surface proteins through activating and inhibitory receptors. For example, inhibitory receptors recognize major histocompatibility complex (MHC) class I molecules, which are constitutively expressed on the surface of healthy cells, but are downregulated in cells infected by viruses [9]. When signaling through inhibitory receptors is reduced, NK cells release granzymes and perforin to kill the target cell [9]. In addition to their cytotoxic function, NK cells are an important source of IFN-γ in the early stages of infection [9]. IFN-γ is a potent activator of macrophages and also promotes host defense against viruses by inhibiting viral replication and enhancing antigen presentation via MHC class I molecules [7].

If the innate immune response is not sufficient to clear the infection, an adaptive immune response is initiated [4]. Here, DCs play a central role: Unlike macrophages and neutrophils, their main purpose is not to remove microbial

pathogens, but to present pathogen-derived antigens to T cells via MHC molecules [9]. When DCs encounter pathogens, they are activated and migrate to regional lymph nodes, where they activate antigen-specific naïve T cells [4]. Once activated, T cells proliferate and differentiate into effector T cells [4]. This process takes several days, and therefore, it takes days to weeks to mount an adaptive immune response [4]. Whereas innate immune receptors are germline-encoded and therefore recognize a limited set of ligands, the receptors of T and B cells are generated through random recombination of gene segments and can therefore detect virtually any antigen [4]. Hence, while it takes longer to initiate, the adaptive immune response is more specific [4].

There are two main types of effector T cells, cytotoxic T cells and T$_H$ cells [4]. Via their T cell receptor and co-receptor CD8, cytotoxic T cells recognize antigens derived from intracellular pathogens, which are presented via MHC class I molecules [4, 6]. Upon target cell recognition, cytotoxic T cells release granzymes and perforin to kill their target cells, similar to NK cells [7]. Via their T cell receptor and co-receptor CD4, T$_H$ cells recognize antigens presented via MHC class II molecules on the surface of DCs, macrophages or B cells [6]. Naïve CD4 T cells themselves are activated by antigens presented by DCs, and activated T$_H$ cells release cytokines to activate macrophages and B cells upon antigen recognition [4, 6]. Once activated, B cells differentiate to plasma cells that secrete antigen-specific immunoglobulins [10]. Immunoglobulins play an important role in the humoral immune response [4]: They can directly neutralize viruses and toxins, and indirectly contribute to the removal of bacteria through opsonization and complement activation [4].

Importantly, upon activation, some T and B cells differentiate into memory cells which can quickly be reactivated upon re-infection with the same pathogen and confer long-lasting immunity [4]. Immunological memory has long been thought to be a specific characteristic of adaptive immune cells. However, more recent studies showed that innate immune cells can undergo epigenetic reprogramming upon activation, resulting in increased responsiveness upon re-infection [11]. This effect has been termed "trained immunity" [11].

Finally, the various mechanisms employed by the immune system are tightly regulated to minimize tissue damage. Dysregulation of the innate and adaptive immune response can result in autoinflammatory and autoimmune diseases, respectively [12, 13].

1.2. Pattern recognition receptors

The cells of the innate immune system are equipped with pattern recognition receptors (PRRs) which allow them to discriminate between self and non-self. PRRs are sensors for pathogen-associated molecular patterns (PAMPs) and damage-associated molecular patterns (DAMPs), which constitute conserved molecular structures present within microbes but not within the host (e.g., lipopolysaccharide (LPS)) and endogenous molecules released from damaged cells (e.g., endogenous DNA), respectively [14]. Apart from PAMP and DAMP recognition by PRRs – which is a direct ligand-receptor interaction – certain sensors also detect the perturbation of cellular homeostasis rather than a specific molecular pattern [14]. This mechanism, referred to as effector-triggered immunity, is especially common among members of the nucleotide-binding domain, leucine-rich repeat-containing receptor (NLR) family [14]. Since these sensors resemble PRRs in domain architecture, structure and function, they are often categorized as PRRs, even though strictly speaking they do not function as such. One model that explains the mechanism of effector-triggered immunity is the "guard" model: It proposes that certain host proteins act as guards of cellular processes, and that disruption of these processes by pathogen effectors elicits a host response [14].

In the vertebrate system, there are four major PRR families that can be grouped based on protein domain homology: (1) Toll-like receptors (TLRs); (2) C-type lectin receptors; (3) NLRs; and (4) retinoic acid-inducible gene I (RIG-I)-like receptors (RLRs) [15]. In addition, cytoplasmic nucleic acids are sensed by the oligoadenylate synthetase (OAS) protein family, including cyclic GMP-AMP synthase (cGAS) [16, 17]. TLRs and C-type lectin receptors constitute membrane-bound (or, in the case of some C-type lectins, unbound extracellular) receptors which detect PAMPs and DAMPs present in the extracellular space or endosomal compartments [15]. NLRs, RLRs, OAS and cGAS constitute unbound intracellular receptors which detect PAMPs and DAMPs present in the cytosol [15]. Some unbound intracellular PRRs assemble multiprotein complexes termed "inflammasomes", which are described in more detail below. Importantly, PRRs are not only expressed by "classical" innate immune cells such as macrophages, monocytes and DCs, but also by epithelial cells and cells of the adaptive immune system [18].

1.2.1. Toll-like receptor signaling

The human genome encodes 10 TLRs. Activation of TLR1-9 is well studied and has been shown to initiate pro-inflammatory responses. In contrast, the function of TLR10 remains less well characterized, with both pro- and anti-inflammatory functions reported in the literature [19, 20]. TLRs are transmembrane proteins with an extracellular (or luminal) domain consisting of 18-25 leucin-rich repeats (LRRs) and a cytoplasmic Toll-IL-1 receptor (TIR) domain [9]. The family of TLRs can be divided into two subgroups: TLR1, TLR2, TLR4, TLR5 and TLR6 localize to the plasma membrane, whereas TLR3, TLR7, TLR8 and TLR9 localize to endosomal compartments [9]. Of note, TLR3 has also been shown to localize to the plasma membrane [21]. Plasma membrane bound TLRs recognize components of the bacterial cell wall, including diacyl and triacyl lipopeptides (TLR2/6 and TLR1/2, respectively), LPS (TLR4) and flagellin (TLR5) [9]. Endosomal TLRs recognize nucleic acids derived from viruses and/or bacteria, including dsRNA (TLR3), RNA degradation products (TLR7 and TLR8) and unmethylated CpG dinucleotides (TLR9) [9]. Furthermore, endosomal TLRs can be activated by endogenous nucleic acids in the context of autoinflammatory diseases [22]. In contrast to other TLRs, which directly bind their respective ligands, TLR4 indirectly senses LPS in complex with MD2 [9]. This process involves two additional proteins, LPS-binding protein and CD14, which are required for LPS transfer and loading onto the TLR4/MD2 complex [23].

A schematic overview of signaling pathways downstream of TLR activation is shown in Figure 1. Ligand recognition induces formation of homo- or heterodimers (TLR1/2 and TLR2/6), resulting in dimerization of the TIR domains and recruitment of TIR-containing adaptor proteins [9]: TLR1/2 and TLR2/6 recruit the adaptor proteins MyD88 and MAL, TLR3 recruits the adaptor protein TRIF, and TLR5, TLR7, TLR8 and TLR9 recruit the adaptor protein MyD88 [9]. TLR4 recruits either MyD88 and MAL or TRIF and TRAM [9]. Therefore, all TLRs except TLR3 signal through the adaptor protein MyD88.

Via its death domain, MyD88 recruits the serine/threonine kinases IRAK4 and IRAK1, giving rise to the so-called myddosome [24, 25]. Following autophosphorylation of IRAKs, the E3 ubiquitin ligase TRAF6 is recruited to the myddosome [26]. K63-linked polyubiquitin chains generated by TRAF6 serve as a platform for the activation of TAK1, which is recruited to the complex by the adaptor proteins TAB2 and TAB3 [9]. Subsequently, TAK1 phosphorylates IKKβ, a component of the IκB kinase complex, which is recruited to polyubiquitin chains [9]. Once activated, the IκB kinase complex phosphorylates IκBα, which is ubiquitinated and degraded by the proteasome [9]. As a result, the transcription factor NF-κB is released and translocates to the nucleus to activate transcription of pro-inflammatory cytokines, including TNF, IL-6 and pro-IL-1β [9]. It is worth
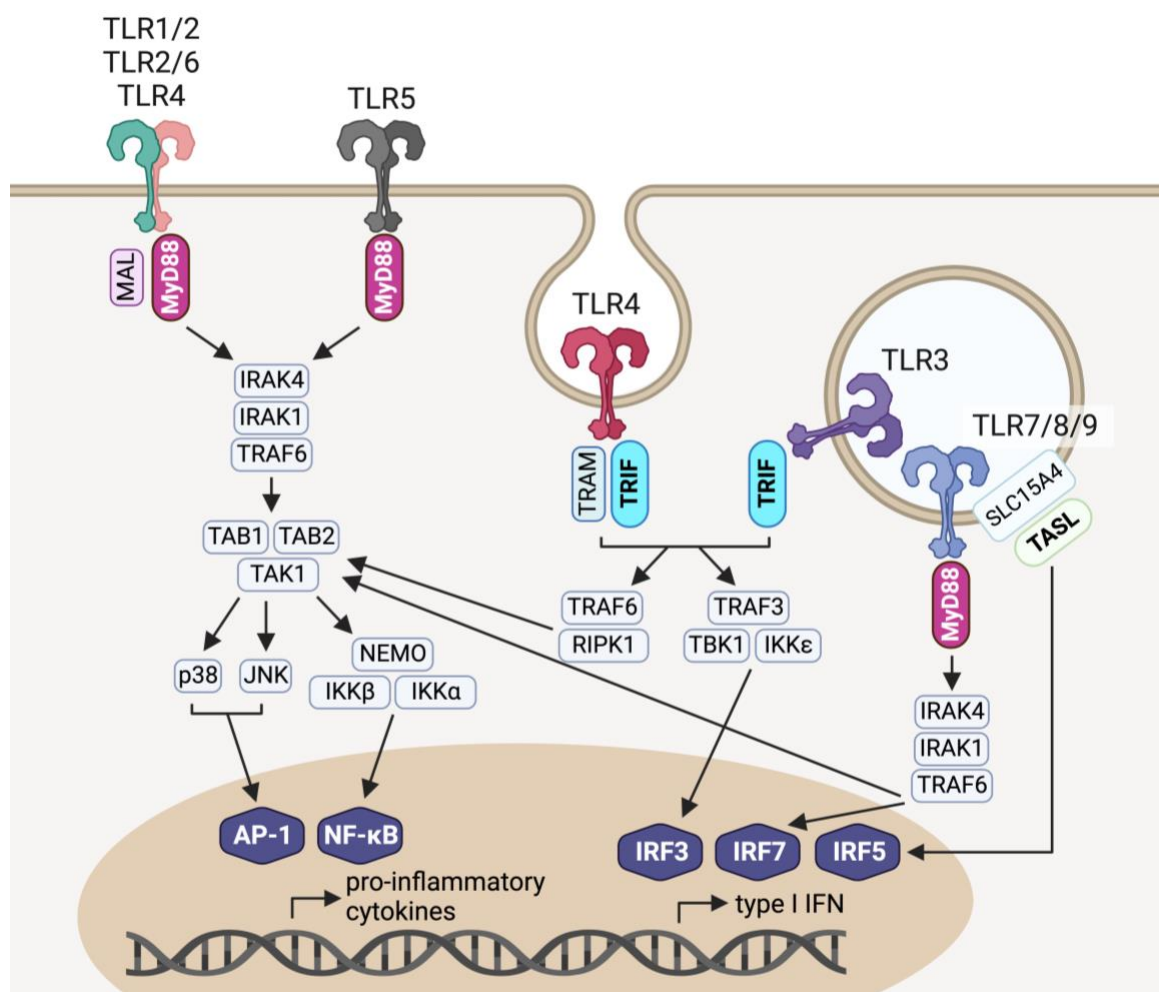
Figure 1. Overview of Toll-like receptor signaling. Upon activation, TLRs recruit different adaptor proteins: TLR1/2 and TLR2/6 recruit the adaptor proteins MyD88 and MAL, TLR3 recruits the adaptor protein TRIF, and TLR5, TLR7, TLR8 and TLR9 recruit the adaptor protein MyD88. TLR4 recruits either MyD88 and MAL (at the plasma membrane) or TRIF and TRAM (upon endocytosis). For simplicity, TLRs are grouped by the adaptor protein(s) used. Signaling through the adaptor protein MyD88 results in the activation of the kinase TAK1, and the downstream activation of the transcription factors AP-1 and NF-κB. These transcription factors drive the expression of pro-inflammatory cytokines. In plasmacytoid DCs, activation of TLR7, TLR8 and TLR9 also results in the activation of the transcription factors IRF5 and IRF7, and the expression of type I interferons. Signaling through the adaptor protein TRIF results in the activation of the kinase TBK1, which activates the transcription factor IRF3. IRF3 drives the expression of type I interferons. In addition, signaling through TRIF results in the activation of TAK1 via TRAF6/RIPK1, and the AP-1 and NF-κB-driven expression of pro-inflammatory cytokines. Created using BioRender.

mentioning that NF-κB has a large number of target genes, ranging from cytokines and chemokines to transcription factors. For example, NF-κB drives the expression of HIF-1α [27], which in turn regulates expression of enzymes involved in glucose metabolism, thereby contributing to the activation of macrophages [28]. Metabolic changes that occur upon macrophage activation are discussed in more detail below (see chapter 1.3.2).

In addition to activation of NF-κB, TAK1 activation results in the downstream activation of the MAP kinases p38 and JNK, which in turn induce AP-1-dependent gene expression [9]. In plasmacytoid DCs, activation of TLR7, TLR8 and TLR9 also

results in the activation of IRF7 and the expression of type I interferons (IFNs) [29-31]. Here, IRF7 is phosphorylated by IRAK1, and this process is dependent on IRAK1, IRAK4 and TRAF6 [32, 33]. Furthermore, in myeloid and plasmacytoid DCs, activation of TLR7, TLR8 and TLR9 results in activation of IRF5 [34]. In a recent study, the adaptor protein TASL was shown to mediate IRF5 activation together with the endolysosomal transporter SLC15A4 [35].

As mentioned above, both TLR3 and TLR4 recruit the adaptor protein TRIF. On one hand, TRIF recruits the E3 ubiquitin ligase TRAF3, which generates a polyubiquitin platform for the activation of TBK1 and IKKε [9]. TRIF contains a pLxIS motif which is phosphorylated by TBK1 [36]. The phosphorylated motif acts as a binding site for the transcription factor IRF3, which, once recruited to the complex, is phosphorylated by TBK1 [36]. Subsequently, phosphorylated IRF3 forms homodimers and translocates to the nucleus to induce expression of type I IFNs [9]. On the other hand, signaling through TRIF results in the activation of TAK1 via TRAF6/RIPK1, and the AP-1 and NF-κB-driven expression of pro-inflammatory cytokines [37].

TLR4 is distinct from other cell surface TLRs in that it undergoes endocytosis upon activation [38, 39]. Upon ligand recognition, signaling at the plasma membrane through the adaptor proteins MyD88 and MAL results in the activation of the transcription factors NF-κB and AP-1, as described above. Subsequently, TLR4 undergoes CD14-dependent endocytosis [40], and TRIF/TRAM-mediated signaling is initiated, resulting in the above-mentioned activation of IRF3 [39].

1.2.2. C-type lectin receptors

C-type lectin receptors are plasma membrane bound or soluble extracellular sensors of carbohydrates [41]. This receptor family comprises a large number of proteins, which have been shown to play a role in the immune response against fungi, bacteria, viruses and parasites [41]. Plasma membrane bound C-type lectin receptors engage in various intracellular signaling pathways: For example, some receptors, including dectin 1 and dectin 2, activate NF-κB by signaling through SYK [41]. Furthermore, several plasma membrane bound C-type lectin receptors, including L-selectin, interact with the cytoskeleton, thereby affecting processes such as migration and phagocytosis [41]. Finally, soluble extracellular C-type lectin receptors, such as mannose binding lectin, opsonize microorganisms and apoptotic cells [42, 43].

1.2.3. The NLR family

In humans, there are 22 NLRs, all of which share a central nucleotide-binding-domain (NACHT) [44]. Furthermore, except for NACHT, LRR and PYD domains-containing protein 10 (NLRP10), all NLRs contain LRRs [44]. The NLR family can further be divided into five subgroups based on the N-terminal domains: (1) 14 NLRPs, which contain a N-terminal pyrin domain (PYD); (2) 5 NLRCs, which contain a N-terminal caspase recruitment domain (CARD) or CARD-like domain; (3) MHC class II transactivator (CIITA), the only NLRA, contains a N-terminal transactivator domain; (4) NAIP, the only NLRB, contains N-terminal baculoviral inhibitor of apoptosis repeat (BIR) domains; and (5) NLRX1, the only NLR containing an N-terminal mitochondrial localization signal [44].

Some members of the NLR family form inflammasomes, which will be described in more detail below. Other NLRs have been shown to positively or negatively regulate different signaling pathways: For example, NOD1 and NOD2, which belong to the sub-family of NLRCs, signal to induce the activation of NF-κB and AP-1 transcription factors [45].

NOD1 and NOD2 sense different fragments of peptidoglycan, a component of the cell wall of both Gram-negative and Gram-positive bacteria [46, 47]. Ligand binding results in conformational changes that allow oligomerization of the sensor, and the subsequent recruitment of the adaptor protein RIPK2 [45]. RIPK2 is ubiquitinated, and the resulting K63-linked polyubiquitin chains serve as a platform for the activation of TAK1 [45]. As described in chapter 1.2.1, TAK1 activation finally results in the activation of AP-1 and NF-κB, and the expression of pro-inflammatory cytokines.

1.2.4. The inflammasomes – regulators of caspase-1 activity

The inflammatory caspases, caspase-1, -4 and -5 (and the murine homolog caspase-11) constitute key regulators of inflammation [48]. Caspase-1 is activated upon the formation of multiprotein complexes termed inflammasomes. These multiprotein complexes are assembled by certain unbound intracellular PRRs, most importantly NLRs: In brief, these PRRs are activated upon detection of certain PAMPs, DAMPs, or perturbations of cellular homeostasis, resulting in the recruitment and oligomerization of apoptosis-associated speck-like protein containing a CARD (ASC), an adaptor molecule which, in turn, recruits pro-caspase-1 [49]. This complex formation is mediated through homotypic interactions of two types of death-fold domains, PYD and CARD [49]. Proximity-induced autocatalytic processing gives rise to catalytically active caspase-1, which mediates the maturation and release of the pro-inflammatory cytokines IL-1β and IL-18, and induces pyroptosis, an inflammatory form of cell death, through gasdermin D (GSDMD) cleavage [49].

First evidence of the existence of inflammasomes was provided in a study by Martinon *et al.* in 2002, in which they described the ability of NLRP1, member of the NLR family, to assemble a caspase-1 activating platform [50]. As yet, eight additional sensors have been shown to assemble inflammasomes: NLRP3, NLRP6, NLRP7, NLRP12 and NLR family CARD domain-containing protein 4 (NLRC4), which belong to the family of NLRs, AIM2, pyrin, and CARD-containing protein 8 (CARD8) [49, 51].

1.2.5. RIG-I like receptor signaling

RIG-I like receptors are cytosolic sensors of viral double-stranded RNA (dsRNA). The RIG-I like receptor family comprises three members: RIG-I, MDA5 and LGP2 [52]. All members of the RLR family share a central helicase domain and a C-terminal domain [52]. In contrast, only RIG-I and MDA5, but not LGP2, have two N-terminal CARDs, which are required for signal transduction [52]. LGP2 seems to play a regulatory role in RLR signaling, and both inhibitory and promoting effects have been reported in the literature [52].

In an inactive state, the CARDs of RIG-I interact with the helicase domain, resulting in autoinhibition [53]. Structural analyses showed that both the central helicase domain and the C-terminal domain (CTD) of RIG-I are required for dsRNA binding [53, 54], with the CTD binding 5'-triphosphates [55]. Both 5'-triphosphorylated and 5'-diphosphorylated dsRNA have been shown to activate RIG-I [56, 57]. Ligand binding, together with ATP hydrolysis, induces conformational changes that make the CARDs accessible for downstream signaling [53]: Both filament formation through oligomerization of RIG-I helicase-CTD and K63-linked polyubiquitin chains induce the oligomerization of the CARDs [58-61]. The RIG-I CARD oligomers recruit the adaptor protein MAVS, which in turn forms filaments that act as a platform for the activation of TBK1 and IKKε [52, 62]. MAVS is a transmembrane protein that is anchored to the outer mitochondrial membrane. Like the TLR signaling adaptor TRIF, MAVS contains a pLxIS motif, which, once phosphorylated by TBK1, recruits IRF3 for activation [36]. Finally, activation of IRF3 and IRF7 by TBK1 and IKKε, as well as activation of NF-κB, results in the expression of type I IFNs [52, 63].

In contrast to RIG-I, ligand binding by MDA5 does not require a 5'-triphosphate group [64]. MDA5 senses long dsRNA, with a length of approx. 2 kb required to induce an MDA5-dependent interferon response [65]. Upon activation, MDA5 wraps around dsRNA to form filaments, and the resulting MDA5 CARD oligomers recruit MAVS, inducing downstream signaling as described for RIG-I [66-68].

1.2.6. The oligoadenylate synthetase family

Similar to RLRs, OASs and cGAS sense cytoplasmic nucleic acids. The members of the OAS family all share a nucleotidyl transferase domain [69]. OAS1, OAS2, OAS3 and oligoadenylate synthetase-like protein (OASL) bind dsRNA, whereas cGAS binds dsDNA [69]. Of note, while OASL is able to bind dsRNA, it has been shown to be catalytically inactive [70].

dsRNA binding activates OASs through inducing conformational changes [71]. Upon activation, OASs generate 2'-5' linked oligoadenylates, which in turn act as a second messenger to activate the endoribonuclease RNase L [71]. RNase L degrades both host- and virus-derived single-stranded RNA, thereby inhibiting protein biosynthesis [71]. In a more recent study, activity of OASs was shown to be dependent on the length of dsRNA fragments, with longer fragments resulting in higher enzymatic activity [72].

For the catalytically inactive OASL, both pro- and antiviral effects have been described in different contexts [73]. On the one hand, OASL has been described to inhibit cGAS, thereby promoting replication of DNA viruses, including Herpes simplex virus-1 [74]. On the other hand, OASL has been shown to enhance RIG-I activity, thereby promoting antiviral responses against RNA viruses, including Sendai virus [75]. Unlike the other OASs, OASL contains two C-terminal ubiquitin-like domains [76], which were shown to mimic polyubiquitin, thus promoting the RIG-I mediated antiviral response [75].

Like OASs, cGAS undergoes conformational changes upon ligand binding that result in its activation [77]. Subsequently, cGAS generates 2',3'-cyclic GMP-AMP (cGAMP), which activates the adaptor protein STING [16]. STING is a transmembrane protein that resides at the endoplasmic reticulum. Once activated, STING translocates to the Golgi and activates TBK1 [78]. Like the adaptor proteins TRIF and MAVS, STING contains a pLxIS motif that is involved in the recruitment and activation of IRF3 [36]. While cGAS-STING signaling primarily drives type I IFN expression via activation of IRF3, it also activates NF-κB, although the underlying mechanism has not yet been fully clarified [78].

1.3. The effects of TLR signaling on macrophages

1.3.1. Cytokines released by macrophages and their function

Signaling induced downstream of PRR activation results, among others, in the expression of pro-inflammatory cytokines. Once released, cytokines act in an autocrine, paracrine and/or endocrine fashion and induce a broad range of specific responses that propagate the immune response [9]. Pro-inflammatory cytokines released by macrophages include tumor necrosis factor α (TNF), interleukin-6 (IL-6), IL-1β, IL-12 and CXCL8 [9].

TNF is arguably one of the most important cytokines of the innate immune system. It belongs to a family of 19 proteins, which, unlike other cytokines, are transmembrane proteins [79]. The release of TNF is mediated by ADAM17 (a disintegrin and metalloproteinase 17) [80]. Both membrane bound and soluble TNF can induce signaling through engaging TNF receptor 1 (TNFR1) or TNFR2 [79]. While TNFR1 is ubiquitously expressed, TNFR2 expression is confined to endothelial cells, immune cells and neurons [79]. TNFR1 and TNFR2 signaling both result in the activation of NF-κB, thereby promoting survival [79]. Additionally, signaling through TNFR1 can induce cell death (apoptosis or necroptosis), owing to its C-terminal death domain [79]. The outcome of TNFR1 signaling depends on the ubiquitination status of the adaptor protein RIPK1, which is recruited to the TNFR1 signaling complex together with other factors [79].

In endothelial cells, TNF induces the cell surface expression of adhesion molecules such as P- and E-selectin and ICAM-1, thereby promoting leucocyte recruitment [9]. Moreover, TNF disrupts endothelial cell-cell junctions, thereby increasing vascular permeability [9, 81]. This promotes the recruitment of leukocytes to the site of infection and the release of plasma proteins into adjacent tissue, and increases drainage of fluids to lymph nodes [9]. Additionally, TNF-mediated signaling results in increased platelet adhesion to the endothelium and subsequent occlusion of blood vessels [9]. While on a local scale, these effects prevent the spread of the infection, systemic release of TNF induces shock [9]. In addition to its effects on endothelial cells, TNF acts in an autocrine fashion to maintain macrophage viability upon activation by T_H1 cells [82]. Furthermore, TNF plays a role in DC maturation and drives IgA switching and secondary expansion of mucosal B cells [9, 83]. Finally, together with IL-6 and IL-1, TNF induces the acute-phase response, which will be described in more detail below [9].

IL-6 belongs to the hematopoietin superfamily, a group of cytokines that signals through tyrosine-kinase-associated receptors [9]. Upon binding of IL-6 to the interleukin-6 receptor (IL-6R), a member of the class I cytokine receptor family, IL-6R associates with glycoprotein 130 kDa (gp130) [84, 85]. The subsequent dimerization of gp130 leads to phosphorylation of Janus kinases (JAKs), which in

turn activate STAT3 (signal transducer and activator of transcription 3) [84]. Dimerized STAT3 then translocates to the nucleus to activate transcription of target genes [84]. Importantly, IL-6R can be processed by ADAM17 into a soluble form, allowing IL-6 to exert pleiotropic functions: While IL-6R expression is restricted to hepatocytes, lymphocytes, and myeloid cells, gp130 is expressed by many cell types, including endothelial cells [84]. Therefore, signaling through soluble IL-6R can be activated in a broad range of cells.

IL-6 induces differentiation of T_H17 and T_{FH} cells, and inhibits the suppressive activity of T_{reg} cells [7, 13, 84]. Moreover, IL-6 drives plasma cell differentiation and antibody production [84]. Finally, IL-6 plays a role in the acute-phase response [9].

IL-1β belongs to the IL-1 cytokine family and is expressed as an inactive precursor, pro-IL-1β [9]. As mentioned in chapter 1.2.4, caspase-1-mediated proteolytic cleavage is required to generate mature IL-1β. Alternatively, extracellular processing of pro-IL-1β can be catalyzed by the neutrophil protease proteinase-3, matrix metalloproteinase 9, elastase and granzyme A [86]. IL-1β signals through a heterodimer consisting of IL-1 receptor 1 (IL-1R1) and its co-receptor IL-1R3 [86]. Downstream signaling is mediated by TIR domains, which recruit MyD88 to induce NF-κB activation, as described for TLR signaling [86].

Together with TGF-β, IL-6 and IL-23, IL-1β is involved in T_H17 differentiation [82]. Furthermore, IL-1β induces the expression of cell adhesion molecules on endothelial cells, thereby facilitating leukocyte recruitment [9, 87]. As already mentioned, IL-1β is also involved in inducing the acute-phase response [9].

In the acute-phase response, TNF, IL-6 and IL-1β act on several cell types and tissues to coordinate the response to infection: Firstly, TNF, IL-6 and IL-1β induce the expression of acute-phase proteins in hepatocytes [9]. These proteins opsonize microorganisms either directly or indirectly, by activating the complement system [9]. Secondly, TNF, IL-6 and IL-1β act on the bone marrow epithelium to induce neutrophil mobilization, thus promoting pathogen removal [9]. Finally, TNF, IL-6 and IL-1β induce expression of prostaglandin E2, which in turn acts on the hypothalamus to induce fever [9].

IL-12 belongs to the hematopoietin superfamily and consists of an α- and β-subunit, which are linked by disulfide bonds [88, 89]. It induces dimerization of IL-12 receptor β1 (IL-12Rβ1) and IL-12Rβ2, and subsequent activation of JAK2, resulting in the downstream activation of the transcription factor STAT4 [88].

Alongside type I IFNs and IL-18, IL-12 is an activator of NK cells [9]. Furthermore, together with IFN-γ, IL-12 stimulates T_H1 cell differentiation by inducing expression of the transcription factor T-bet [7]. Importantly, IL-12 stimulates NK and T_H1 cells to release IFN-γ, which plays an important role in macrophage activation [7, 9].

CXCL8 belongs to the chemokine family, a group of small proteins which serve as chemoattractants [9]. CXCL8 binds to the G-protein coupled receptors CXCR1 and

CXCR2, which are selectively expressed by neutrophils [82]. It carries out several functions that promote the recruitment of neutrophils to the site of infection: Firstly, CXCL8 induces neutrophil mobilization from the bone marrow [9]. Secondly, CXCL8 is released by macrophages at the site of infection and binds to proteoglycans on endothelial cells and in the extracellular matrix, thereby generating a gradient that recruits neutrophils [9]. Finally, CXCL8 increases adhesion of neutrophils to the endothelium by mediating integrin activation [9].

1.3.2. Metabolic reprogramming of macrophages

TLR signaling not only induces the expression of pro-inflammatory cytokines, but also results in metabolic reprogramming of immune cells, including macrophages. First evidence of metabolic changes induced upon macrophage activation was provided in 1970, where activated murine peritoneal macrophages were found to exhibit lower oxygen consumption and higher levels of glycolysis [90]. It was only later that the two populations of classically activated (M1) and alternatively activated (M2) macrophages were defined [91-93], which are now recognized to be two extremes of a broad spectrum of functional states [94]. M1- and M2-polarized macrophages differ with regard to the metabolism of iron, folate and glucose [94].

Along with other stimuli, including poly(I:C) and lipoteichoic acid, LPS induces activation of macrophages via signaling pathways downstream of TLRs, including NF-κB and PI3K, which both result in the oxygen-independent regulation of HIF-1α transcription [95-97]. In macrophages, HIF-1α not only upregulates the expression of inflammatory mediators, but also of several proteins involved in glycolysis [28, 98]. Mechanistically, this increase in glycolysis has been suggested to compensate for the decrease in mitochondrial ATP production: Since complex I (CI) of the electron transport chain (ETC) is required for mitochondrial reactive oxygen species (mtROS) production (discussed in more detail below), mitochondrial metabolism may shift away from oxidative phosphorylation (OXPHOS), and an increase in glycolysis may be required to match the cellular ATP demand [99]. At the same time, pentose phosphate pathway activity is increased, resulting in an increased supply of purines and pyrimidines, and, more importantly, providing NADPH for reactive oxygen species (ROS) production by NADPH oxidase [100, 101]. Furthermore, upon metabolic reprogramming, the TCA cycle is interrupted at several points. This leads to the accumulation of the metabolites citrate, itaconate, and succinate [95]. Citrate is required for sustaining the macrophage inflammatory response via the production of nitric oxide, ROS and prostaglandin E2, itaconate possesses anti-bacterial properties, and succinate inhibits prolyl hydroxylases, which regulate HIF-1α stability in an oxygen-dependent manner [95]. In summary, metabolic reprogramming is required for pro-inflammatory functions of macrophages.

1.4. NMES1 is a largely uncharacterized protein

1.4.1. NMES1 expression is highly upregulated upon LPS stimulation

NMES1 is a 9 kDa protein which is encoded by C15orf48 (human) and AA467197 (mouse). Amino acid sequence alignment using NCBI BLASTp showed that the sequence is conserved between human and mouse (72 % identities, 87 % positives) (Figure 2A) [102, 103]. Intriguingly, NMES1 expression is strongly induced in murine macrophages upon stimulation with LPS [104, 105]. The induction is a late event, with high mRNA expression levels being observed 6-7 hours after stimulation (Figure 2B). Similarly, in human monocytes, NMES1 protein levels are low under steady-state conditions, while a strong increase can be observed upon LPS stimulation (Figure 2C) [106]. Analysis using COXPRESdb revealed that NMES1 is co-expressed with several pro-inflammatory genes, arguing for similar regulation of expression (Figure 2D) [107].
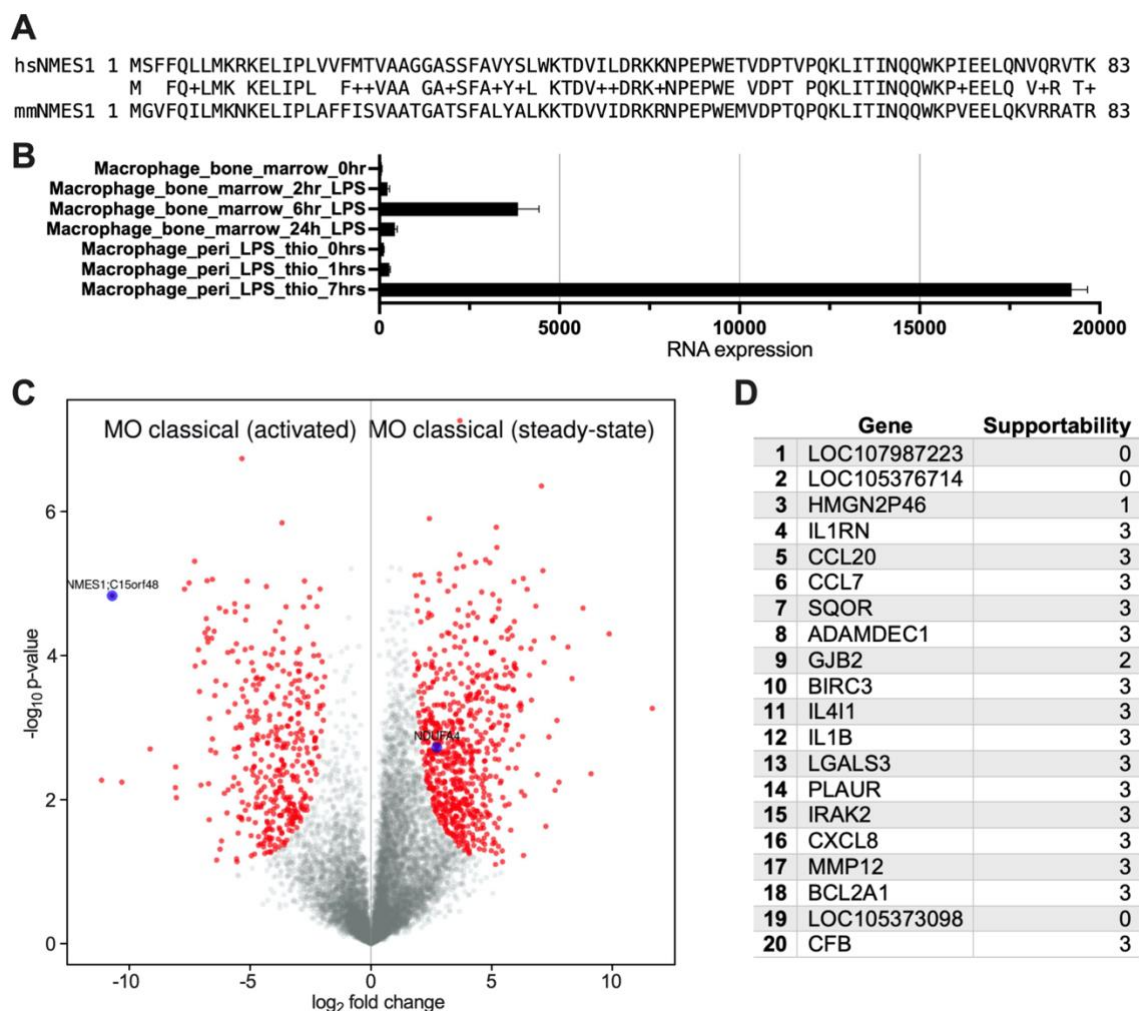
Figure 2. NMES1 expression is induced upon LPS stimulation. (A) Amino acid sequence alignment of human (hs) and mouse (mm) NMES1 (NP_115789.1 and NP_001004174.1, respectively), generated using NCBI BLASTp [102, 103]. **(B)** mRNA expression levels of NMES1 in mouse macrophages. Taken from BioGPS [104, 105]. **(C)** Differential protein expression in human monocytes: steady-state vs. LPS stimulated. T- test differences are plotted as fold-change (x-axis,

in log$_2$) and p-value (y-axis, in -log$_{10}$). Proteins with significantly different expression levels (two-tailed Welch's t-test, S0 = 1, FDR < 5 %) are shown in red. NMES1 and NDUFA4 are highlighted in blue. Taken from ImmProt [106]. **(D)** List of genes which are co-expressed with NMES1. Top 20 co-expressed genes are shown. "Supportability" indicates that co-expression is supported by another platform. Statistical significance was calculated to determine the probability of co-expressed gene lists being similar by coincidence. Three levels of supportability are used: 1, 2 and 3 correspond to p<1E-04, p<1E-16 and p<1E-32, respectively. Data was retrieved from COXPRESdb [107].

The C15orf48 promoter region was reported to contain three potential NF-κB consensus binding motifs and a GAS element, suggesting that NMES1 expression may be regulated by NF-κB and STAT family members [108]. In addition, Liu *et al.* reported an increase in NMES1 mRNA expression in THP-1 cells upon LPS stimulation [108]. In line with these findings, NMES1 protein levels were found to be increased in response to treatment with IL-1β in both human aortic endothelial cells (HAECs) and the lung epithelial cell line A549 in a more recent publication [109]. Furthermore, Sorouri *et al.* showed that NMES1 mRNA expression can be induced by treatment with either IFN-α or IFN-γ in A549 cells, whereas in myeloid HL-60 cells, expression is most strongly induced by treatment with IFN-γ [110]. Experimental evidence regarding the effect of IFN-γ on NMES1 protein levels has, however, not yet been provided. Clayton *et al.* analyzed the effect of IFN-β and LPS on NMES1 expression: While in mouse bone marrow derived macrophages (BMDMs) IFN-β and LPS were both found to be potent activators of NMES1 expression, in human monocyte-derived macrophages (MDMs) NMES1 expression was only strongly induced by stimulation with LPS, but not IFN-β [111]. Interestingly, the expression of mouse and human NMES1 seems to be regulated by different signaling pathways: LPS-induced expression in mouse BMDMs was completely blunted when cells were co-treated with the Janus kinase inhibitor ruxolitinib, while expression in human MDMs was not affected [111]. In line with these findings, NMES1 expression has previously been found to be strongly reduced in BMDMs derived from *Ifnar* [-/-], *Trif* [-/-] and *Irf3* [-/-] mice [112].

1.4.2. NMES1 is a mitochondrial protein

NMES1 has first been identified as a potential tumor suppressor in human esophageal squamous cell carcinoma [113], and was later also shown to be downregulated in colorectal cancer [114]. In humans, NMES1 is mainly expressed in the gastrointestinal tract, male reproductive tissues and lymphoid tissues [115, 116]. Single cell RNA expression data for various tissues, including adipose tissue, esophagus, kidney and lung show high NMES1 expression levels in macrophages [117, 118]. In mice, NMES1 is mainly expressed in the normal adult gut as well as embryonic bone, brain, intestine and stomach [113]. While published immunohistochemistry and immunofluorescence data indicated that NMES1 localizes to the nucleus [113, 119], a more recent study showed that NMES1 localizes to the mitochondria [120]. In a high-throughput screen aiming to identify

mitochondrial protein interactions, NMES1 was found to interact with subunits of CI and complex IV (CIV) of the ETC, suggesting its involvement in the regulation of CI and/or CIV activity [121]. In line with this finding, NMES1 was more recently identified as a novel component of CIV by blue native PAGE (BN PAGE) [120].

A sequence homology search using NCBI BLASTp revealed NDUFA4L2 as top hit (25 % identities, 54 % positives) [102, 103] (Figure 3A), while structural homology analysis using HHpred revealed NDUFA4 as top hit [122-124] (31 % identities, similarity = 0.575) (Figure 3B). AlphaFold predictions for the structure of NMES1, NDUFA4 and NDUFA4L2 are shown in Figure 3C [125, 126].

A

```
NMES1      3 FFQLLMKRKELIPLVVFMTVAAGGASSFAVYSLWKT-DVILDRKKNPEPWETVDPTVPQKLITINQQWKPIEE 74
             F++ + +   +IP++  + +  G A+ + +    ++ DV  DRK NPEPW  + P    K + ++  +K +++
NDUFA4L2  10 FYRQIKRHPGIIPMIGLICLGMGSAALYLLRLALRSPDVCWDRKNNPEPWNRLSPNDQYKFLAVSTDYKKLKK 82
```

B

```
Q ss_pred    cHHHHHhhhhhchhhhheeeeeccCcchhhHHHhhe-eeceeecCCCCCCCcccCCCCCChheeecccccccHH
Q NMES1     2 SFFQLLMKRKELIPLVVFMTVAAGGASSFAVYSLW-KTDVILDRKKNPEPWETVDPTVPQKLITINQQWKPIE 73
Q Consensus 2 sffqllmkrkeliplvvfmtvaaggassfavyslw-ktdvildrkknpepwetvdptvpqklitinqqwkpie 73
              +++..+.+..|++||+++|++|.+||..+.++.+. ..||.++| +|++||+.++++-.+|+.+.|+.|+..+
T Consensus 4 ~~~~~~k~~pel~PL~~~vg~a~~~a~~~~~r~~~~~pdV~~~k~~n~~PW~~~~~~~K~~~~~~~~~~~~~~ 75
T NDUFA4    4 QIIGQAKKHPSLIPLFVFIGTGATGATLYLLRLALFNPDVCWDR-NNPEPWNKLGPNDQYKFYSVNVDYSKLK 75
T ss_pred     HHHHHHhhChhhHHHHHHHHHHHHHHHHHHHHHHHHhcCCCCccCC-CCCCchhhcCCCCCeeceecCCCHHhcc
```

C

Figure 3. NMES1 shares homology with NDUFA4 and NDUFAL2. (A) Amino acid sequence alignment of human NMES1 and NDUFA4L2 (NP_115789.1 and NP_001381889.1, respectively), generated using NCBI BLASTp [102, 103]. **(B)** Homology detection and structure prediction by HMM-HMM comparison using HHpred [122-124]. Query (Q): human NMES1 (NP_115789.1), Target (T): human NDUFA4 (NP_002480.1). ss_pred: secondary structure prediction based on PSI-PRED, C/c: coil, H/h: α-helix, E/e: β-sheet. Symbols indicate the quality of the column-column match: "|" = very good, "+" = good, "·" = neutral, "−" = bad, "=" = very bad. **(C)** AlphaFold predictions for the structure of human NMES1, NDUFA4 and NDUFA4L2 [125, 126].

NDUFA4 was originally believed to be a component of CI of the ETC [127]. However, biochemical assays and structural analysis confirmed that NDUFA4 is rather a component of CIV [128, 129]. Interestingly, NDUFA4 was reported to play an important role in maintaining CIV stability [129]. Furthermore, Tello *et al.* observed a decrease of NDUFA4 protein levels under hypoxia, whereas NDUFA4L2 expression is upregulated under these conditions [130]. A similar effect

can be observed for NDUFA4 and NMES1 upon LPS stimulation: Published proteomics data generated using primary human monocytes show that NDUFA4 protein levels are decreased upon LPS stimulation compared to steady-state conditions (Figure 2C) [106]. This inverse regulation of NMES1 and NDUFA4 has also recently been described by Clayton *et al.* and Lee *et al.* [109, 111].

NDUFA4L2 has been reported to inhibit CI activity, thereby decreasing oxygen consumption, membrane potential and mtROS production under hypoxic conditions [130]. It is well established that HIF-1α, the transcription factor driving NDUFA4L2 expression, is stabilized downstream of TLR signaling, allowing expression of target genes independent of oxygen levels (see chapter 1.2). Recently, NDUFA4L2 was found to decrease mtROS production in dendritic cells, thereby limiting autoimmunity in an experimental model of autoimmune encephalomyelitis [131].

In a recent study, Sorouri *et al.* found that several viruses acquired the genes encoding NMES1 and NDUFA4 by horizontal gene transfer [110]. Viral homologs of NMES1 exist in squirrel pox virus and Namao virus [110]. Furthermore, phylogenetic analysis of primate genomes revealed that the genes encoding NMES1 and NDUFA4 rapidly evolved, indicating that these proteins may be targeted for inactivation by pathogens and thus play a role in host defense processes [110]. Interestingly, data published by Sorouri *et al.* suggest that loss of NDUFA4 increases the susceptibility to apoptotic triggers, while loss of NMES1 conferred resistance to apoptosis [110]. Similar to loss of NMES1, overexpression of the squirrel pox homolog of NMES1 rendered cells less susceptible to apoptotic triggers [110]. Based on these findings, Sorouri *et al.* suggested that replacement of NDUFA4 by NMES1 may promote apoptosis in response to stress [110]. In addition to NDUFA4, NMES1 and NDUFA4L2, two miRNAs, miR-210 and miR-147b, were identified as part of this new mitochondrial stress response network [110]. The latter will be discussed in more detail below.

1.4.3. NMES1 gene transcript gives rise to miR-147b

The human NMES1 gene also encodes a microRNA, miR-147b, which corresponds to miR-147 in mice. This miRNA is derived from NMES1 gene transcripts, which serve as pri-miRNA [108]. The sequence of pre-miR-147b/miR-147 is located in exon 5 (human) or exon 4 (mouse) within the 3' UTR of the NMES1 gene transcript (Figure 4A) [108].

The microRNA target site prediction tool TargetScan lists NDUFA4 as the top hit for both miR-147b and miR-147 (Figure 4B), supporting the hypothesis that there exists a negative feedback loop linking NMES1 and NDUFA4 [132]. As already mentioned above, most recently, Sorouri *et al.* suggested that NMES1, NDUFA4 and miR-147b are part of a mitochondrial stress response network [110], and Lee

et al. could show that NMES1 and miR-147b both contribute to the decrease in NDUFA4 protein levels [109]. Furthermore, miR-147b has been suggested to be part of a network regulating glucose metabolism in colorectal cancer cells [133]. In addition, miR-147b has been described to confer resistance to Osimertinib treatment through targeting VHL and succinate dehydrogenase [134]. Downregulation of these factors induces a pseudo-hypoxic state through activation of HIF-1α and thus shifts metabolism towards glycolysis [134]. In summary, there seems to be a regulatory function of miR-147b in cancer cell metabolism.
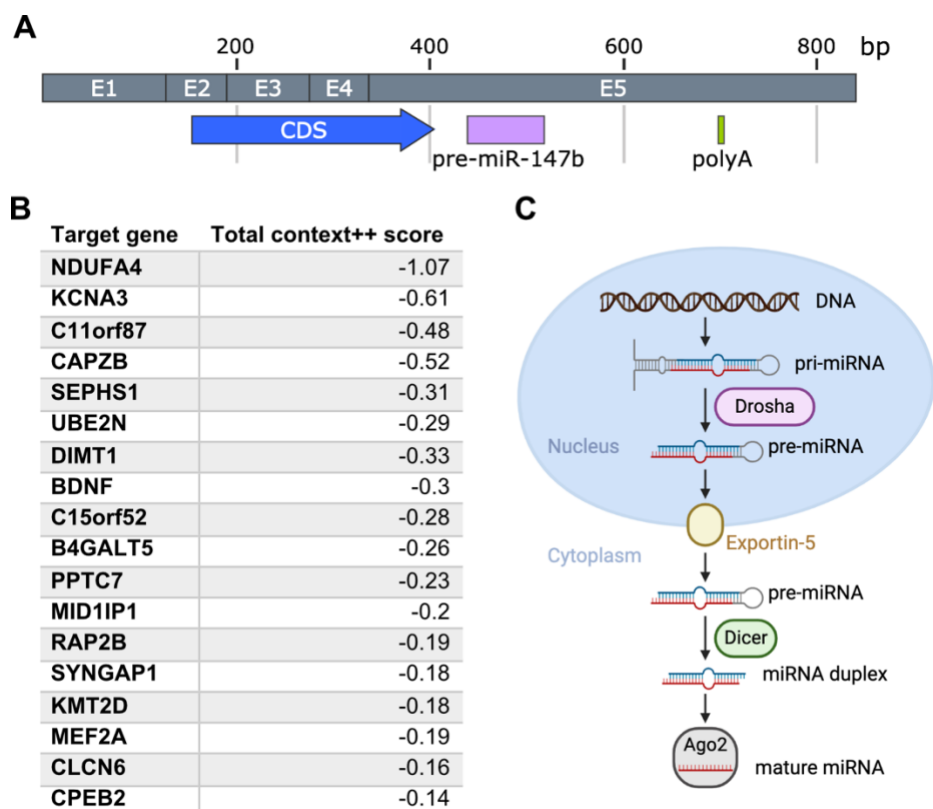
Figure 4. miR-147b is encoded in the 3' UTR of NMES1 mRNA and targets NDUFA4. **(A)** Schematic representation of the human NMES1 mRNA. Coding sequence, pre-miR-147b and poly(A) signal are annotated in blue, lavender and green, respectively. Created using SnapGene. E1-5 = exon 1-5, CDS = coding sequence. **(B)** Target genes of miR-147b predicted using TargetScan 7.0 [132, 135]. Target genes are ranked by total context++ score. **(C)** Schematic representation of canonical miRNA processing. pri-miRNA is processed to pre-miRNA by Drosha in the nucleus, followed by export of pre-miRNA into the cytoplasm. pre-miRNA is then further processed by Dicer to give rise to a miRNA duplex. Strands are separated and the mature miRNA is loaded into argonaute (Ago) proteins. Adapted from Martier & Konstantinova [136]. Created using BioRender.

Liu *et al.* found that the mouse homolog miR-147 is induced upon TLR stimulation and regulates murine macrophage inflammatory responses by acting as negative regulator of TLR signaling [108]. Transfection with miR-147 mimics was shown to decrease TLR-stimulation induced inflammatory cytokine expression and, conversely, knock-down of miR-147 increased TLR stimulation-induced cytokine expression [108]. Therefore, there seems to be a negative feedback loop in which miR-147 is induced upon LPS stimulation to prevent excessive inflammation [108].

The first steps of miRNA processing are carried out in the nucleus, where pri-miRNA is processed by Drosha into 60-70 nt long pre-miRNA (Figure 4C). Since NMES1 mRNA serves as pri-miRNA for miR-147b [108], the generation of miR-147b and export of mRNA for translation are mutually exclusive, and therefore, miR-147b and NMES1 could be expected to show inverse expression patterns. However, it has been shown that both miR-147b and NMES1 mRNA expression levels are increased upon stimulation with LPS in human MDMs [111], and upon IFN-γ treatment in A549 cells [110]. The regulatory mechanisms governing the fate of NMES1 mRNA remain elusive. Importantly, the fact that NMES1 mRNA can be processed by Drosha to give rise to pre-miR-147b may explain potential discrepancies between NMES1 mRNA and protein levels.

1.4.4. NMES1 expression is upregulated in various types of cancer

A tumor suppressive role has been suggested for NMES1 in the early literature [113, 114]. In contrast, a recent study reported upregulated NMES1 expression in various cancers, including esophageal squamous cell carcinoma and colon adenocarcinoma as well as breast, ovarian, pancreatic and lung cancer [137]. The effect of copy number variation differs between cancer types: While in renal clear cell carcinoma, sarcoma and thyroid carcinoma, deletion mutations of C15orf48 were found to be associated with poor prognosis, amplification mutations of C15orf48 were found to be associated with poor prognosis in low-grade glioma and uterine corpus endometrial carcinoma [137]. In addition, high NMES1 expression was found to be associated with poor prognosis in glioma and lung cancer patients [137, 138]. Interestingly, NMES1-high expressing thyroid carcinomas showed a significant increase in macrophage infiltration [137]. Furthermore, in various cancers, including thyroid carcinoma, lung adenocarcinoma and glioma, NMES1 expression positively correlated with the expression of inhibitory immune checkpoint molecules, such as CTLA4 [137]. Of note, this was not the case for any of the gastrointestinal cancers [137]. In line with higher expression levels of inhibitory immune checkpoint molecules, patients with NMES1-high expressing thyroid carcinomas responded significantly better to immune checkpoint blockade therapy than patients with NMES1-low expressing tumors [137]. Overall, the role of NMES1 in cancer seems to vary between different kinds of tumors, and recent data does not support its initially suggested role as a tumor suppressor. Due to the lack of appropriate healthy controls, it remains unclear whether NMES1 is differentially expressed in myeloid cancers. Furthermore, it remains to be investigated whether NMES1 expression is differentially regulated in tumor-infiltrating macrophages and, if so, whether this affects anti-tumor immune responses.

1.5.   The electron transport chain

As already mentioned, NMES1 has recently been identified as a component of CIV of the electron transport chain (ETC). The ETC consists of four protein complexes which are located in the inner mitochondrial membrane, and the electron carriers coenzyme Q and cytochrome c (Figure 5) [139]. It is required to build up a proton gradient, which is used by ATP synthase (complex V; CV) to generate ATP [139]. In mammals, the subunits of CI, CIII, CIV and CV are encoded in part by the nuclear and in part by the mitochondrial genome [140]. The expression of the different subunits is regulated on a post-transcriptional level by miRNAs and RNA-binding proteins to coordinate expression from both genomes [141]. The complexes of the electron transport chain predominantly localize to cristae membranes [142, 143], with CV localizing to the curved cristae edges [144, 145].
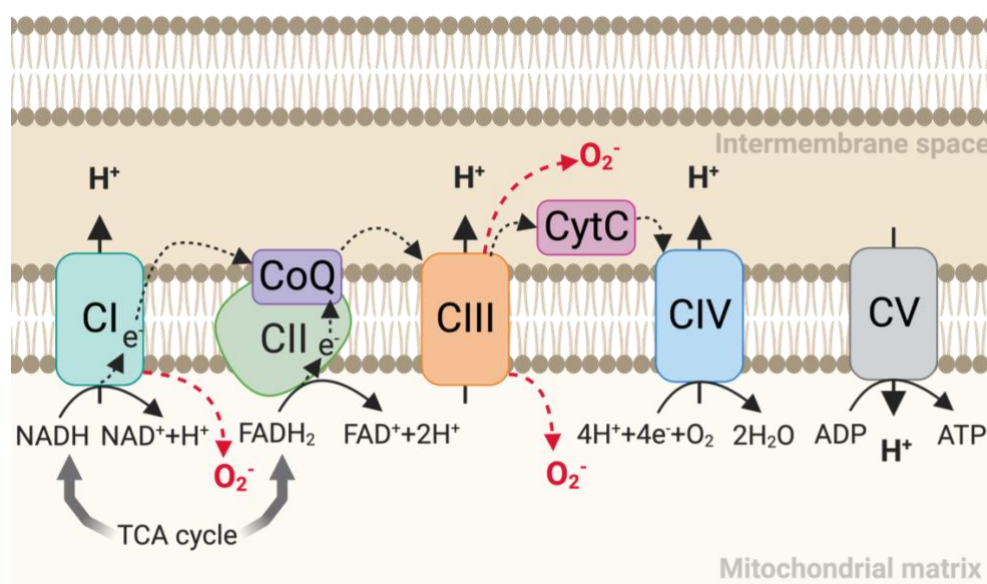
Figure 5. Overview of the electron transport chain. The electron transport chain consists of four protein complexes which reside in the inner mitochondrial membrane, and the two electron carriers coenzyme Q (CoQ) and cytochrome c (CytC). NADH and FADH$_2$ are byproducts of the TCA cycle and serve as electron donors for complex I (CI) and complex II (CII), respectively. The energy released upon electron transport is used to generate a proton gradient, which is used by ATP synthase (complex V, CV) to generate ATP. CI and CIII are the main source of mitochondrial ROS. Created using BioRender.

1.5.1. CIV of the electron transport chain consists of 14 subunits

CIV of the electron transport chain consists of three mitochondrially encoded subunits, MTCO1, MTCO2 and MTCO3, and 11 nuclear-encoded subunits [128]. Out of all mammalian electron transport chain complexes, CIV exhibits the highest level of complexity: Tissue-specific isoforms exist for subunits COX4, COX6A, COX6B, COX7A, and COX8 [146]. In addition, the expression of isoforms of COX4 and NDUFA4 is dependent on oxygen levels [146]. Interestingly, the liver-specific isoforms COX6A2, COX7A1 and COX8B were detected in CIV dimers, whereas CIV monomers were found to exclusively contain the heart-specific isoforms

COX6A1, COX7A2, and COX8A [128]. Therefore, it was suggested that these subunits may regulate the transition between monomeric and dimeric CIV [147]. Even though it has been proposed that monomeric CIV constitutes the active form [148], it remains unclear how higher-order complex formation affects CIV activity.

1.5.2. Complexes I-IV form mitochondrial supercomplexes

Mammalian complexes I-IV of the electron transport chain have been reported to assemble into higher-order complexes, so-called supercomplexes [149, 150]. A schematic overview of the composition of different supercomplexes is shown in Figure 6. The current model suggests that both the individual complexes and supercomplexes coexist, with supercomplex composition varying based on bioenergetic demand [151]. How supercomplex assembly is regulated is still under investigation: Supercomplex assembly factor 1 (SCAF1) was shown to mediate the interaction between CIII and CIV and is required for the formation of the supercomplex III_2+IV [152]. Furthermore, supercomplex assembly has been shown to be dependent on cristae shape, which is modulated by OPA1 [153]. Conversely, cristae remodeling, which occurs during apoptosis, leads to the disassembly of supercomplexes [153].

Whether the formation of supercomplexes has biologically relevant effects on OXPHOS remains to be determined. Since CI almost exclusively exists as a part of assembled supercomplexes [149], it has been suggested that supercomplex formation increases CI stability [154]. In addition, supercomplexes were proposed to increase electron transfer efficiency through substrate channeling [149], although this hypothesis has been challenged in the more recent literature [155]. Furthermore, it has been suggested that supercomplex formation may prevent aggregation and the resulting loss of function of ETC components [156]. Recently, supercomplexes were shown to enhance electron transfer by limiting cytochrome c diffusion distance [157]. Finally, experimental evidence suggests that supercomplex assembly decreases mitochondrial ROS production [158, 159], which will be discussed in more detail below.
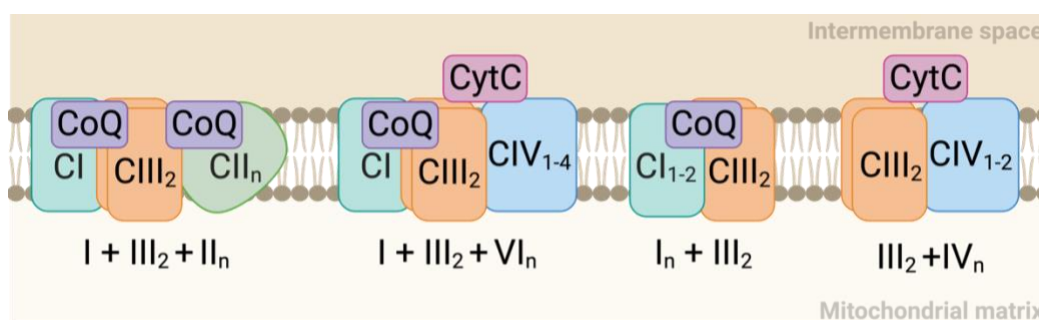
Figure 6. Schematic representation of mitochondrial supercomplexes. CI-IV = complex I-IV. CoQ = coenzyme Q; CytC = cytochrome C. Adapted from Jha *et al.* and Kohler *et al.* [150, 160]. Created using BioRender.

1.5.3. CI and CIII give rise to mitochondrial ROS

In addition to its role in ATP production, the ETC is a major source of ROS: electrons leaking from the ETC are transferred to molecular oxygen, resulting in superoxide formation (see Figure 5) [161]. CI and CIII of the ETC are the main source of mitochondrial ROS (mtROS) [162]. Both mtROS and ROS produced by NADPH oxidase contribute to microbial killing by macrophages [163]. While mtROS were originally thought to be mere byproducts of OXPHOS, a study by West *et al.* suggests that mtROS production in macrophages may be regulated through TLR1/2/4, which predominantly recognize bacterial components [163]. Furthermore, it has been proposed that mtROS production in macrophages is induced upon LPS stimulation by triggering reverse electron transport [164]. Mechanistically, reverse electron transport occurs when the coenzyme Q pool is highly reduced with electrons from CII and there is high proton motive force driving reverse catalysis at CI [165]. Mills *et al.* showed that upon LPS stimulation, succinate levels increase, and increased succinate oxidation by CII results in elevated mtROS production [164]. CII inhibition resulted in a decrease in pro-IL-1β mRNA and protein levels, suggesting that mtROS drive pro-IL-1β expression [164]. In addition to their role in microbial killing, mtROS also act as signaling molecules: mtROS have been shown to drive pro-inflammatory signaling in DCs through activating the unfolded protein response [166]. Furthermore, mtROS have been implicated in NLRP3-mediated pyroptosis: Wang *et al.* found that mtROS promote GSDMD cleavage through oxidation of GSDMD [167].

Of note, mtROS have been reported to exert different functions depending on mtROS levels. While intermediate levels of mtROS are required to sustain the inflammatory response, low levels of mtROS play a role in adaptation to hypoxia [168]. In the context of hypoxia, mtROS were found to induce HIF-1α, which in turn inhibits mtROS production via negative feedback [169]: HIF-1α induces the transcription of NDUFA4L2, which was shown to inhibit CI of the ETC, thereby reducing mtROS levels [130].

2. AIMS

Intriguingly, expression of NMES1 is strongly induced in macrophages upon LPS stimulation, suggesting a role for this largely uncharacterized protein in inflammation. NMES1 shares amino acid sequence homology with NDUFA4L2, a hypoxia-induced negative regulator of the electron transport chain. Therefore, we hypothesized that NMES1 exerts a similar function in the context of inflammation, acting as an NF-κB-inducible negative regulator of the electron transport chain: NMES1 might be incorporated into complex IV of the electron transport chain instead of NDUFA4, thereby giving rise to a nonfunctional complex. Furthermore, induction of NMES1 expression is a late event, with high expression levels observed 6-7 hours after stimulation. Therefore, we hypothesized that NMES1 might dampen the inflammatory response through negative regulation of pro-inflammatory signaling.

As such, the overarching goal of this project was to analyze the role of NMES1 in the TLR-ligand-induced inflammatory response and characterize its effect on the electron transport chain.

3. MATERIALS AND METHODS

3.1. List of materials

Table 1. List of reagents.

Reagent	Supplier	Product no.
0.05 % Trypsin-EDTA	Gibco	25300-054
0.9 % NaCl solution	ABC Arznei	08609261
10x Fast Digest Green buffer	Thermo Scientific	B72
2-mercaptoethanol, Liquid, ≥99.0 %	Sigma-Aldrich	M6250-10ML
2-Deoxy-D-glucose, ≥98% (GC), crystalline	Sigma-Aldrich	D8375-5G
5x GC buffer	Thermo Scientific	F519
5x green GoTaq Reaction buffer	Promega	M791A
96-well High Binding Standard ELISA Microplates	Greiner Bio-One	655081
Acetic acid 99 %	Carl Roth	7332.2
ADP	Jena Bioscience	NU-1198-1G
Agilent Seahorse XFE96 FluxPaks	Agilent Technologies	102416-100
Alt-R® CRISPR-Cas9 tracrRNA, 100 nmol	IDT	1072534
Alt-R® S.p. Cas9 Nuclease V3, 100 µg	IDT	1081058
Amersham Protran Premium 0.2 µm nitrocellulose	GE Healthcare	10600004
Ampicillin	Carl Roth	K029.3
AnalaR NORMAPUR EDTA dihydrate	VWR	2032.293
Anti-DYKDDDDK G1 Affinity Resin	Genscript	L00432-5
Antimycin A aus Streptomyces sp.	Sigma-Aldrich	A8674
Ascorbate	Sigma-Aldrich	A5960
BD Micro-FineTM, U-100 insulin, 0.33 mm (29 G)×12.7 mm	VWR	BDAM324891
Biocoll® separating solution	Bio&SELL	BS.L 6115
Biozym LE Agarose	Biozym Scientific	840004
Blasticidin S HCl (10 mg/ml)	Thermo Scientific	A1113903
Bovine Serum Albumin	Sigma Aldrich	A7906-100G
Braun Sterican® Needles Gr. 18 - G 26 x 1'', 0,45 x 25 mm	neoLab	TZ-1447
Buffer PB	Qiagen	19066
Buffer RLT	Qiagen	79216
Buffer RLT plus	Qiagen	1053393
Carbonyl cyanide 4-(trifluoromethoxy)phenylhydrazone (FCCP)	Sigma-Aldrich	C2920
CD14 MicroBeads, human	Miltenyi Biotec	130-050-201
cOmplete protease inhibitor tablet	Roche	25735720
Coomassie brilliant blue	Thermo Scientific	20278
Cornig 100 µm cell strainer	Sigma Aldrich	431752
D-Mannitol, BioXtra, ≥98 % (HPLC)	Sigma Aldrich	M9546-1KG
Deoxynucleotide triphosphate (dNTP) set	Genaxxon	M3015.4100

Reagent	Supplier	Product no.
Detachin™ Cell Detachment Solution	Genlantis	T100100
DL-Dithiothreitol, ≥98 % (HPLC), ≥99.0 % (titration)	Sigma Aldrich	D0632-100G
DMEM (1x)	Gibco	41965-039
DMSO	Sigma Aldrich	D8418-250ML
Doxycycline hyclate	Sigma Aldrich	D9891-1G
DPBS (1x)	Gibco	14190-094
EconoSpin spin columns for DNA	Epoch Life Science	1920-250
EcoSpin columns	Epoch Life Science	1910-250
Electroporation cuvettes, 4 mm gap size	VWR	732-1137
EMSURE sodium chloride for analysis	Merck	1.06404.5000
Ethanol 99.8 %	Carl Roth	K928.4
Ethylene glycol-bis(2-aminoethylether)-N,N,N′,N′-tetraacetic acid	Sigma-Aldrich	03777-10G
FastAP Thermosensitive Alkaline phosphatase	Thermo Scientific	EF0654
FastDigest BamHI	Thermo Scientific	FD0054
FastDigest BglII	Thermo Scientific	FD0083
FastDigest NheI	Thermo Scientific	FD0973
Fatty acid free BSA	Sigma-Aldrich	10775835001
Fetal calf serum (FCS)	Thermo Scientific	10270106
Filtropur S 0.2	Sarstaedt	83.1826.001
GeneJuice	Merck	70967-1mL
GeneRuler 1 kb DNA ladder	Thermo Scientific	SM0311
GeneRuler 1 kb plus DNA ladder	Thermo Scientific	SM1331
GeneRuler 100 bp DNA ladder	Thermo Scientific	SM0241
Gibson assembly master mix	MPI core facility	n.a.
Glycerol Rotipuran® >99,5 % p.a. wasserfrei	Carl Roth	15725350
GoTaq G2 DNA Polymerase	Promega	M7845
HEPES	Sigma Aldrich	H0887-100ML
Human IFN alpha 2a reseach grade	Miltenyi Biotec	130-093-873
Human IL-6 ELISA Set	BD Biosciences	555220
Human Serum	Sigma Aldrich	H5667-100ML
Human TNF ELISA Set	BD Biosciences	555212
IDT duplex buffer	IDT	1072570
IMDM	Thermo Scientific	12440-053
Imiquimod	Sigma Aldrich	I5159-200MG
Immobilon Forte Western HRP Substrate	Merck	WBLUF0500
Immobilon-PSQ PVDF Membrane, 0.2 µm	Sigma Aldrich	ISEQ00005
Invitrogen Novex NuPAGE LDS Sample Buffer (4X)	Thermo Scientific	NP0007
Invitrogen™ UltraPure™ 0.5M EDTA, pH 8.0	Thermo Scientific	15575020
Isopropanol	Sigma-Aldrich	278475-1L
LPS EB ultrapure	InvivoGen	tlrl-3pelps
Magnesium chloride hexahydrate	Sigma-Aldrich	M2393-100G

Reagent	Supplier	Product no.
Methanol	Sigma Aldrich	32213-1L
Milk powder, blotting grade	Carl Roth	T145.2
MiSeq reagent kit v2	Illumina	MS-102-2002
Mitochondria isolation kit, human	Miltenyi Biotec	130-094-532
MitoSOX™ Mitochondrial Superoxide Indicator	Thermo Scientific	M36008
N,N-Dimethylacrylamide, 99 %	Sigma Aldrich	274135-5ML
NativePAGE™ 5 % G-250 Sample Additive	Thermo Scientific	BN2004
NativePAGE™ Cathode Buffer Additive (20X)	Thermo Scientific	BN2002
NativePAGE™ Sample Buffer (4X)	Thermo Scientific	BN2003
NORMAPUR NaOH	VWR	28244.295
Novex™ Digitonin (5 %)	Thermo Scientific	BN2006
Novex™ NativeMARK™ unstained protein standard	Thermo Scientific	LC0725
Novex™ NativePAGE™ 4-16 % Bis-Tris gel, 10 well	Thermo Scientific	BN1002BOX
Novex™ NativePAGE™ running buffer (20x)	Thermo Scientific	BN2001
NuPAGE 12 % Bis-Tris Gel, 15 well	Thermo Scientific	NP0343BOX
NuPAGE 12 % Bis-Tris Gel, 17 well	Thermo Scientific	NP0349BOX
NuPAGE 4-12 % Bis-Tris Gel, 15 well	Thermo Scientific	NP0323BOX
NuPAGE 4-12 % Bis-Tris Gel, 17 well	Thermo Scientific	NP0329BOX
NuPAGE MOPS SDS running buffer (20X)	Thermo Scientific	NP0001
Nupage™ 12 % Bis-Tris Protein Gels, 1.0 mm, 2D-well	Thermo Scientific	NP0346BOX
ODN2006 (ODN 7909)	InvivoGen	tlrl-2006
Oligomycin A ≥99 % (HPLC)	Sigma-Aldrich	75351-5MG
Omnifix solo 50 mL	B. Braun	4616502F
OptiMEM	Gibco	31985-070
P3 Primary Cell 96-well Nucleofector™ Kit	Lonza	V4SP-3096
PAGERuler Prestained Protein Ladder	Thermo Scientific	26616
Pam_3CSK_4	InvivoGen	tlrl-pms
Pan monocyte isolation kit, human	Miltenyi Biotec	130-096-537
Penicillin-Streptomycin (10,000 U/mL)	Thermo Scientific	15140163
Phorbol 12-myristate 13-acetate (PMA)	Enzo Life Sciences	BML-PE160-0005
Phusion high-fidelity DNA polymerase	Thermo Scientific	F530L
Pierce ECL Western blotting substrate	Thermo Scientific	32106
Pierce Hoechst 3342 Fluorescent Stain	Thermo Scientific	62249
Pierce™ BCA Protein Assay Reagent A	Thermo Scientific	23228
Pierce™ BCA Protein Assay Reagent B	Thermo Scientific	23224
Pierce™ Bovine Serum Albumin Standard Ampules	Thermo Scientific	23209
Poly-L-ornithine, 0.01 %	Sigma Aldrich	P4957-50ML
poly(I:C) (high molecular weight)	InvivoGen	tlrl-pic
Polyethylenimine HCl MAX, Linear, Mw 40,000 (PEI MAX 40000)	Polysciences	24765-1
Ponceau S solution	Sigma Aldrich	P7170-1L

Reagent	Supplier	Product no.
Potassium azide	Sigma-Aldrich	740411
Potassium hydroxide solution,45 wt. % in H2O	Sigma-Aldrich	417661-500ML
Potassium phosphate monobasic, ≥99.0 %	Sigma-Aldrich	P5655-100G
Protamine sulfate salt from salmon	Sigma-Aldrich	P4020-1G
Proteinase K	VWR	0706-500MG
PureLink™ HiPure Plasmid Filter Midiprep Kit	Thermo Scientific	K210015
Puromycin dihydrochloride	Carl Roth	0240.4
QIAquick Gel Extraction Kit	Qiagen	28706
QIAquick PCR Purification Kit	Qiagen	28106
R848	InvivoGen	tlrl-r848-5
RBC Lysis Buffer (10X)	BioLegend	420301
Recombinant human IFN-γ	Peprotech	300-02
Recombinant human M-CSF protein	MPI, core facility	n. a.
RevertAid Reverse transcriptase	Thermo Scientific	EP0441
Ribolock RNAse inhibitor	Thermo Scientific	EO0381
RPMI 1640	Gibco	21875-034
Seahorse XF 1.0 M Glucose Solution, 50 mL	Agilent Technologies	103577-100
Seahorse XF 100 mM Pyruvate Solution, 50 mL	Agilent Technologies	103578-100
Seahorse XF 200 mM Glutamine Solution, 50 mL	Agilent Technologies	103579-100
Seahorse XF Calibrant Solution	Agilent Technologies	100840-000
Seahorse XF DMEM Medium pH 7.4	Agilent Technologies	103575-100
Seahorse XF RPMI Medium, pH 7.4	Agilent Technologies	103576-100
Serva DNA stain clear G	Serva	39804.01
SG cell line 4D-Nucleofector X Kit S	Lonza	V4XC-3032
Sodium azide, 99.5 % Reagent Plus®	Sigma Aldrich	S2002-25G
Sodium Pyruvate	Gibco	11360-039
Sterican® Gr. 18, G 26 x 1""/ ø 0,45 x 25 mm	B. Braun	4657683
Sucrose, ≥99.5 % (GC)	Sigma-Aldrich	S1888-500G
Sulfuric acid 50 %	Carl Roth	4318.1
T4 DNA ligase	Thermo Scientific	EL0014
T4 ligase buffer (10x)	Thermo Scientific	B69
Takyon No ROX SYBR 2X MasterMix blue dTTP	Eurogentec	UF-NSMT-B0710
TL-8-506	InvivoGen	tlrl-tl8506
TMB substrate reagent set	BD Biosciences	555214
TMPD	Sigma-Aldrich	T7394
Total RNA Purification Mini Spin Kit PLUS	Genaxxon	S5309.0010
Tween 20	Carl Roth	9127.2
Water Ecotainer®	B. Braun	0082479E
XF Cell mito stress test kit	Seahrorse Bioscience	103015-100
XF plasma membrane permeabilizer	Agilent Technologies	102504-100
Zombie Aqua™ Fixable Viability Kit	BioLegend	423102

Table 2. List of buffers and solutions.

Buffer/solution	Ingredients
Coomassie destain solution	50 % methanol 25 % acetic acid
Coomassie staining solution	45 % ethanol 10 % acetic acid 0.1 % Coomassie R-250
Direct lysis buffer	1 mM $CaCl_2$ 3 mM $MgCl_2$ 1 mM EDTA 1 % Triton X-100 10 mM Tris (pH 7.5) 0.2 mg/mL proteinase K
ELISA coating buffer	7.13 g $NaHCO_3$ 1.59 g Na_2CO_3 add ddH_2O to total volume 1 L pH 9.5 storage at 4 °C
FACS buffer	2 % FCS in DPBS
Guanidinium chloride buffer (10×)	6 M guanidium chloride 10 mM TCEP 40 mM 2-chloroacetamide 0.1 M Tris/HCl, pH 8 Freeze in aliquots Before use, dilute 1:10 in 0.1 M Tris/HCl, pH 8
Laemmli sample buffer (6×)	450 mM Tris-HCl pH 6.8 12 % SDS 0.03 % bromphenol blue 60 % glycerol 600 mM DTT
LB agar	20 g LB broth base 15 g agar add ddH_2O to total volume 1 L autoclave before use 100 µg/mL ampicillin
LB medium	20 g LB broth base add ddH_2O to total volume 1 L autoclave before use
Low pH elution buffer	0.1 M glycine pH 2.5
MACS buffer	2 mM EDTA 2 % FCS in DPBS
MAS buffer (3×)	660 mM mannitol 210 mM sucrose 30 mM KH_2PO_4 15 mM Mg_2Cl 6 mM HEPES 3 mM EGTA pH 7.4

Buffer/solution	Ingredients
Miniprep buffer N3	4.2 M guanidine hydrochloride 0.9 M potassium acetate pH 4.8
Miniprep buffer P1	50 mM Tris (pH 8.0) 10 mM EDTA 100 µg/mL RNase A
Miniprep buffer P2	200 mM NaOH 1 % SDS
Miniprep buffer PE	10 mM Tris (pH 7.5) 80 % ethanol
Mito co-IP lysis buffer	50 mM HEPES-KOH, pH 7.4 150 mM NaCl 1 mM EDTA 0.16 % digitonin
Mito co-IP wash buffer	50 mM HEPES-KOH, pH 7.4 150 mM NaCl 1 mM EDTA
NuPAGE transfer buffer (20$\times$)	500 mM Bicine 500 mM Bis-Tris (free base) 20 mM EDTA
Neutralization buffer	1 M Tris pH 8.5
PBS (10$\times$)	1.37 M NaCl 27 mM KCl 100 mM Na_2HPO_4 18 mM KH_2PO_4
PBS-T	1$\times$ PBS (pH 7.4) 0.5 % Tween-20
Peptide separation buffer A	0.1 % (v/v) formic acid
Peptide separation buffer B	80 % (v/v) acetonitrile 0.1 %(v/v) formic acid
RIPA buffer	50 mM Tris (pH 7.3) 150 mM NaCl 1 % NP-40 substitute 0.1 % SDS 1 mM EDTA
Stage tip loading buffer	10 % (v/v) Acetonitrile 3 % (v/v) trifluoroacetic acid
Tris-glycine buffer (10$\times$)	285 mM Tris 1.92 M glycine
TAE buffer	40 mM Tris (pH 8.0) 20 mM acetic acid 1 mM EDTA
TBS (20$\times$)	400 mM Tris 3 M NaCl
TBS-T	1$\times$ TBS (pH 7.6) 0.5 % Tween-20

Table 3. List of DNA oligonucleotide sequences. All DNA oligonucleotides were ordered from IDT.

Name	Sequence	Used for
EF-1alpha_F	TCATTCTCAAGCCTCAGACAGTGG	colony PCR/Sequencing, pEF-BOS
pEF-BOS_R	GGTAGGCGTGTACGGTGGG	colony PCR/Sequencing, pEF-BOS
PKG_R	GTTTCCCGGAACCACGCC	colony PCR/Sequencing, pLI
TRE_F	GTATGTCGAGGTAGGCGTGTACG	colony PCR/Sequencing, pLI
U6_F	GAGGGCCTATTTCCCATGATT	sequencing, pmini
Seq_mScarlet_F	CTGGAAGATGGCACCCTGATCT	sequencing
MiSeq adapter fwd	ACTCTTTCCCTACACGACGCT	sequencing
Oligo dT	TTTTTTTTTTTTTTTTTTTTVN	cDNA synthesis
NheI_hNMES1_F	ATTAGCTAGCATGAGCTTTTTCCAACTCCTGATGAAAAG	cloning
hNMES1_FLAG_BglII_R	TAATAGATCTTCACTTATCATCATCATCCTTGTAGTCCGCACTCCCCCCACCTTTGGTCACCCTTTGGACATTTTGC	cloning
hNMES1_BglII_R	TAATAGATCTTCATTTGGTCACCCTTTGGACATTTTG	cloning
NheI_NDUFA4_F	ATTAGCTAGCATGCTCCGCCAGATCATCG	cloning
BamHI_NDUFA4_R	ATTAGGATCCTTAGAAATCTGGACGTTCCTTCTTCAGC	Cloning
BamHI_NDUFA4_FLAG_R	ATTAGGATCCTCACTTATCATCATCATCCTTGTAGTCCGCACTCCCCCCACCGAAATCTGGACGTTCCTTCTTCAGC	cloning
mCherry_BamHI_R	GGATCCTCACTTGTACAGCTCGTCCATGCC	cloning
NheI_mCherry_F	GCTAGCATGGTGAGCAAGGGCGAG	cloning
MLS_mCherry_F	GATCCACCGGTAATGGTGAGCAAGGGCGAG	cloning
pLI_FLAG_mCherry_R1	ATCATCATCCTTGTAGTCCGCACTCCCCCACCCTTGTACAGCTCGTCCATGCC	cloning
pLI_FLAG_mCherry_R2	GCGCAACCCCAACCCCGGATCCTCACTTATCATCATCATCCTTGTAGTCCGCACT	cloning
FLAG_BglII_R2	TAATAGATCTTCACTTATCATCATCATCCTTGTAGTCCGCACTCCCCCCA	cloning
MiSeq_hs_NMES1_F	ACACTCTTTCCCTACACGACGCTCTTCCGATCTGATGGCACAGATTTTGAACA	genotyping
MiSeq_hs_NMES1_R	TGACTGGAGTTCAGACGTGTGCTCTTCCGATCTAACCCTGACTCCCAGTTCAC	genotyping

Name	Sequence	Used for
MiSeq_hs_NDUFA4_F	ACACTCTTTCCCTACACGACGCTCTTCCGATCTCCCTAATGTTATCGCCCTACA	genotyping
MiSeq_hs_NDUFA4_R	TGACTGGAGTTCAGACGTGTGCTCTTCCGATCTTGAGACTTGGAAATCAATGTGC	genotyping
MiSeq_hs_NMES1_F2	ACACTCTTTCCCTACACGACGCTCTTCCGATCTTTGAAGTGTCCAAATGTGTCC	genotyping
MiSeq_hs_NMES1_R2	TGACTGGAGTTCAGACGTGTGCTCTTCCGATCTTCTGACCCATTGGTAGACAATATC	genotyping
MiSeq_hs_TBX21_F	ACACTCTTTCCCTACACGACGCTCTTCCGATCTCTGTCAAGCTGGAGCTGATG	genotyping
MiSeq_hs_TBX21_R	TGACTGGAGTTCAGACGTGTGCTCTTCCGATCTGAATTAGGGGTAGGGGCTTG	genotyping
MiSeq_hs_NDUFA4_R2	TGACTGGAGTTCAGACGTGTGCTCTTCCGATCTATCTCTCGTTGGCCAGTGTT	genotyping
MiSeq_hs_NDUFA4_g4g5_F	ACACTCTTTCCCTACACGACGCTCTTCCGATCTGGTCTGACGGACGGTAAGTG	genotyping
MiSeq_hs_NDUFA4_g4g5_R	TGACTGGAGTTCAGACGTGTGCTCTTCCGATCTGGGTCCTTCAGGTAGGAGGT	genotyping
ICE_NMES1_F	ACACTCTTTCCCTACACGACGCTCTTCCGATCTTGAGCTTTTTCCAACTCCTGA	genotyping
ICE_NDUFA4_F	ACACTCTTTCCCTACACGACGCTCTTCCGATCTCCAAAGAGAAAACGAGACTCAGA	genotyping
ICE_TBX21_F	ACACTCTTTCCCTACACGACGCTCTTCCGATCTGGTTCTTGTGAGTGGGAGGA	genotyping
oligo dT	TTTTTTTTTTTTTTTTTTVN	cDNA synthesis
LICsgRNA_rev	AACGGACTAGCCTTATTTTAACTTGCTATTTCTAGCTCTAAAAC	Ligation independent cloning
LIC_NDUFA4_g3	GGAAAGGACGAAACACCGTAAGTACTTACCAAACATCGTTTTAGAGCTAGAAATAGCAAGTTAAAATAAGG	Used to clone NDUFA4_g3 into pmini
BamHI_HA_GGGS_R	ATTAGGATCCTCAAGCGTAATCTGGTACGTCGTATGGGTAACTCCCCCCACC	cloning MPC2-HA
BamHI_MPC2_R	ATTAGGATCCTTATTTGTGTGCTTTAGCTTTTAGTTCTTGGT	cloning MPC2-HA
CRISPRa_NMES1_g1_F	CACCGCGGGAGTCGCGTGCCCAACG	cloning gRNAs into pLenti for CRISPRa
CRISPRa_NMES1_g1_R	AAACCGTTGGGCACGCGACTCCCGC	cloning gRNAs into pLenti for CRISPRa
CRISPRa_NMES1_g2_F	CACCGTGACGTGAAGCGCCCGAACG	cloning gRNAs into pLenti for CRISPRa
CRISPRa_NMES1_g2_R	AAACCGTTCGGGCGCTTCACGTCAC	cloning gRNAs into pLenti for CRISPRa
Seq_dCas9-VPR_F0	CGCCTGGAGCAATTCCACA	sequencing

Name	Sequence	Used for
Seq_dCas9-VPR_F1	ATCTCGACAATCTGCTGGCC	sequencing
Seq_dCas9-VPR_F2	AGTGGAGGATCGCTTCAACG	sequencing
Seq_dCas9-VPR_F3	GCTGAACGCCAAACTGATCACA	sequencing
Seq_dCas9-VPR_F4	AAACCCCATCGACTTTCTCGAG	sequencing
Seq_dCas9-VPR_F5	GCATCATGAAGAAGTCCCCCTTC	sequencing
Seq_dCas9-VPR_F6	ACCTGTTGGAGGATCCCGATG	sequencing
sqpNMES1_F	ATTAGCTAGCATGGCTCGGCTGCTTACAC	cloning sqpNMES1(-Strep)
sqpNMES1_R	TAATGGATCCTCAGGAGCCCCTTGGTCCTTC	cloning sqpNMES1
Strep-tag_R	TAATGGATCCTCACTTTTCGAACTGCGGGTG	cloning sqpNMES1(-Strep)
dCas9-VPR_F1_fwd	CGTCAGATCGCCTGGAGAATTGGGCTAGCGAATTCGAATTTGCCAC	cloning dCas9-VPR
dCas9-VPR_F1_rev	CCCCTTATCCACGACTTCCTCGA	cloning dCas9-VPR
dCas9-VPR_F2_fwd	TCGAGGAAGTCGTGGATAAGGGG	cloning dCas9-VPR
dCas9-VPR_F2_rev	GTGTCTCAACAAGCTGCCTTTTGATG	cloning dCas9-VPR
dCas9-VPR_F3_fwd	CATCAAAAGGCAGCTTGTTGAGACAC	cloning dCas9-VPR
dCas9-VPR_F3_rev	CGTCACTTCCCAGCATATCCAGAT	cloning dCas9-VPR
dCas9-VPR_F4.1_fwd	GATCTGGATATGCTGGGAAGTGACG	cloning dCas9-VPR
dCas9-VPR_F4.1_rev	CTGCTGGAACTCGCTGTTGTC	cloning dCas9-VPR
dCas9-VPR_F4.2_fwd	GACAACAGCGAGTTCCAGCAG	cloning dCas9-VPR
qPCR_ADAMTS1_f	CGTCAATGCTTTCCAACCTG	qPCR
qPCR_ADAMTS1_r	TGTATGGGATTCTGAGGCTTG	qPCR
qPCR_CENPT_f	GGAAACAGAGGCTGAGACTG	qPCR
qPCR_CENPT_r	TGAAGAGGTGTGGCAAAGG	qPCR
qPCR_LOXL4_f	GTGGCAGAGTCAGATTTCTCC	qPCR
qPCR_LOXL4_r	TTGTTCCTGAGACGCTGTTC	qPCR
qPCR_MT1E_f	ACTGCTTGTTCGTCTCACTG	qPCR
qPCR_MT1E_r	GCTCTTCTTGCAGGAGGTG	qPCR
qPCR_MT1X_f	CTGCGTGTTTTCCTCTTGATC	qPCR
qPCR_MT1X_r	CAGCTCTTCTTGCAGGAGG	qPCR
qPCR_MT2A_f	CAACCTGTCCCGACTCTAG	qPCR
qPCR_MT2A_r	GCAGCTTTTCTTGCAGGAG	qPCR
qPCR_NTS_f	TCTGACTTTTACGGACTTGGC	qPCR
qPCR_NTS_r	TCTGCTTCTAATGCTTTCATTTCC	qPCR

Name	Sequence	Used for
qPCR_SLC40A1_f	GGGTGGACAAGAATGCTAGAC	qPCR
qPCR_SLC40A1_r	ATGGTACATGGTCAGAAGCTC	qPCR
qPCR_TXN_f	ATCCATTTCCATCGGTCCTTAC	qPCR
qPCR_TXN_r	CGTGGCTGAGAAGTCAACTAC	qPCR
qPCR_C21orf91_F2	ATAGTCACAACCAGGCACAG	qPCR
qPCR_C21orf91_R2	CAGTTGCTCTACCTCACCAAG	qPCR
qPCR_CDH2_f	CCCAAGACAAAGAGACCCAG	qPCR
qPCR_CDH2_r	GCCACTGTGCTTACTGAATTG	qPCR
qPCR_FABP4_f	CATGTGCAGAAATGGGATGG	qPCR
qPCR_FABP4_r	AACTTCAGTCCAGGTCAACG	qPCR
qPCR_MEPE_F2	ACTCCTTTTCAGTGTGACCTG	qPCR
qPCR_MEPE_R2	GCTCTTGATTTATTCTCTTGCCC	qPCR
qPCR_MMP7_f	TTCCAAAGTGGTCACCTACAG	qPCR
qPCR_MMP7_r	AGTTCCCCATACAACTTTCCTG	qPCR
qPCR_MT1E_f2	ACAACCTGCACAACCTGG	qPCR
qPCR_MT1E_r2	AGTCAAAATTGTTTTTATTGTCAGTCAC	qPCR
qPCR_HPRT_F	TGACCTTGATTTATTTTGCATACC	qPCR
qPCR_HPRT_R	CGAGCAAGACGTTCAGTCCT	qPCR
qPCR GAPDH_F	CTTTGTCAAGCTCATTTCCTGG	qPCR
qPCR_GAPDH_R	TCTTCCTCTTGTGCTCTTGC	qPCR
qPCR_TNFAIP3_F	GATAGAAATCCCCGTCCAAGG	qPCR
qPCR_TNFAIP3_R	CTGCCATTTCTTGTACTCATGC	qPCR
qPCR_CD54_F	CAATGTGCTATTCAAACTGCCC	qPCR
qPCR_CD54_R	CAGCGTAGGGTAAGGTTCTTG	qPCR

Table 4. List of DNA fragments. All DNA fragments were ordered from IDT.

Name	DNA fragment sequence	Description
MLS_COX8	CGTCAGATCGCCTGGAGAATTGGCTAGCATGTCCGTCCTGACGCCGCTGCTGCTGCGGGGCTTGACAGGCTCGGCCCGGCGGCTCCCAGTGCCGCGCGCCAAGATCCATTCGTTGGGGGATCCACCGGTAATGGTGAGCAA	DNA fragment encoding the mitochondrial localization signal (MLS) of COX8
sqpNMES1_Strep	ATGGCTCGGCTGCTTACACTCATAGGCAAGCATAAGGAACTGATCCCCCTTGTAGCAGCCGTCGGCGGCGCAGCCGTCGGAGCAACATCTTTTGCACTCTATTCACTCGGGAAGCCGGGTCTTGTCGCTAGACGGGATGGAGGCGATTTGTGGGAAGACGTAGACCCAGAGCGACCGCAGAAATTGCTCACAGTGCACCAACTTTGGCGAGCTATTCCGGAACTGGAGGAAGTGAGAAGGATCGAGCGAGGTGTAGAAGGACCAAGGGGCTCCGGTGGGGGGAGTTGGAGCCACCCGCAGTTCGAAAAGTGA	DNA fragment encoding sqpNMES1-Strep (codon optimized for expression in human cells)

Table 5. List of plasmids.

Plasmid name	Used for
pEF-BOS_FLAG_mScarlet	co-IP (transfection experiments)
pEF-BOS_MPC2-HA	co-IP (transfection experiments)
pEF-BOS_NDUFA4-FLAG	co-IP (transfection experiments)
pEF-BOS_NMES1-FLAG	co-IP (transfection experiments)
pEF-BOS_HA_mScarlet	co-IP transfection experiments
PB-TRE-dCas9-VPR	electroporation of BLaER2 cells
pTwist_CMVbg_mCherry_T2A_FLAG-hypPB_Neo	electroporation of BLaER2 cells
pMini_U6_NDUFA4g3_CMV_mCherry_T2A_Cas9	genome editing in HEK293T/BLaER2
pCMV-VSVg	lentiviral particle production
pMDLg/pRRE	lentiviral particle production
pRSV-rev	lentiviral particle production
pLenti_CRISPRa_hsNMES1_g1_puro	transduction of BLaER2 and THP-1 cells for CRISPRa
pLenti_CRISPRa_hsNMES1_g2_puro	transduction of BLaER2 and THP-1 cells for CRISPRa
pLI_dCas9_VPR_blast	transduction of THP-1 cells
pLI_hs_NMES1_FLAG_puro	transduction of THP-1 cells and other cell lines
pLI_hs_NMES1_puro	transduction of THP-1 cells and other cell lines
pLI_hsNDUFA4_FLAG_puro	transduction of THP-1 cells and other cell lines
pLI_hsNDUFA4_puro	transduction of THP-1 cells and other cell lines
pLI_mCherry_puro	transduction of THP-1 cells and other cell lines
pLI_MLS_mCherry_FLAG_puro	transduction of THP-1 cells and other cell lines

Table 6. List of crRNA sequences. All crRNAs were ordered from IDT. When using a pool of edited cells instead of single cell clones, two or three crRNAs were used in combination as indicated in this table.

Target gene	crRNA number	crRNA sequence	PAM sequence
C15orf48 (NMES1)	1	ACAGUCAUGAACACCACCAA	GGG
	2	AAAACCGAUGUGAUGUAAGU	AGG
NDUFA4	1	UUUAUUGGAACUGGAGCUAC	TGG
	2	AACACUGUAUCUCUUGCGUC	TGG
	3	UUAAGUACUUACCAAACAUC	TGG
NDUFA4	4	ACUUACGCUCGGAUGCUUCU	TGG
	5	UUGCGGCAGAGGUCUCCGAC	TGG
TBX21	1	GCGGUACCAGAGCGGCAAGU	GGG
	2	CGUCCACAAACAUCCUGUAG	TGG

Table 7. List of antibodies and HRP conjugates. mAb = monoclonal antibody, pAb = polyclonal antibody, RT = room temperature.

Antibody	Supplier	Product no.	Additional information
Anti-beta actin (C4), HRP conjugated, mouse mAb	Santa Cruz Biotechnology	SC-47778 HRP	1:1000 dilution in 3 % milk-PBS-T, incubate at RT for 1 h
Anti-C15orf48, rabbit pAb	Sigma Aldrich	HPA012943-100 uL	1:500 dilution in 3 % milk-PBS-T, incubate at 4 °C overnight
Anti-FLAG® M2-Peroxidase (HRP conjugated), mAb	Sigma Aldrich	A8592-1MG	1:1000 dilution in 3 % milk-PBS-T, incubate at RT for 1 h
Anti-human IL-1 beta, goat pAb	R&D Systems	AF201NA	1:1000 dilution in 3 % milk-PBS-T, incubate at 4 °C overnight
Anti-mCherry, rabbit pAb	Novus Biologicals	NBP2-25157	1:1000 dilution in 3 % milk-PBS-T, incubate at 4 °C overnight
Anti-MTCO1 (1D6E1A8), mouse mAb	Thermo Scientific	459600	1:1000 dilution in 3 % milk-PBS-T, incubate at 4 °C overnight
Anti-NDUFA4 (2G7), mouse mAb	Santa Cruz Biotechnology	sc-517091	1:1000 dilution in 5 % BSA-PBS-T, incubate at 4 °C overnight
Anti-phospho-STAT1 (Tyr701) (D4A7), rabbit mAb	Cell Signaling	7649S	1:1000 dilution in 5 % BSA-TBS-T, incubate at 4 °C overnight
Goat anti-rabbit IgG-HRP	Cell Signaling	7074S	1:1000 dilution in 3 % milk-PBS-T, incubate at RT for 1 h
Horse anti-mouse IgG-HRP	Cell Signaling	7076S	1:1000 dilution in 3 % milk-PBS-T, incubate at RT for 1 h
Mouse anti-goat IgG-HRP	Santa Cruz Biotechnology	SC2354	1:1000 dilution in 3 % milk-PBS-T, incubate at RT for 1 h
Strep-Tactin®-HRP conjugate	IBA Lifesciences GmbH	2-1502-001	1:1000 dilution in 5 % BSA-PBS-T, incubate at RT for 1 h; Blocking in 5 % BSA-PBS-T
Anti-Strep-tag, mouse mAb	Qiagen	34850	1:1000 dilution in 5 % BSA-PBS-T, incubate at 4 °C overnight; Blocking in 5 % BSA-PBS-T Secondary antibody in 3 % milk-PBS-T
anti-VDAC1/2, rabbit mAb	Abcam	ab154856	1:1000 dilution in 5 % BSA-PBS-T, incubate at 4 °C overnight

Table 8. List of Laboratory Equipment.

Equipment	Supplier
NanoDrop 1000 spectrophotometer	PeqLab
FusionCapt Advance FX7 16.15 imaging system	Vilber
ChemiDoc MP imaging system	Bio-Rad
BioTek 405 Touch microplate washer	BioTek
C1000 Touch Thermal Cycler	Bio-Rad
4D-Nucleofector X Unit	Lonza
FACSAria Fusion	BD
LSRFortessa	BD
Spark20M microplate reader	Tecan
TC20 automated cell counter	Bio-Rad
Gen5-Epoch microplate reader	BioTek
Seahorse XFe96 extracellular flux analyzer	Agilent
Cytation 1 cell imaging multimode reader	BioTek
Gene Pulser Xcell Electroporation System	Bio-Rad
Biomek FX Automated Liquid Handler	Beckman Coulter
Biomek i7 Automated Workstation	Beckman Coulter
MiSeq™ system	Illumina
CFX96 Touch Real-Time PCR Detection System	Bio-Rad

3.2.   Cell Culture

3.2.1. Isolation of PBMCs and primary human monocytes

Peripheral blood mononuclear cells (PBMCs) were isolated from heparinized blood donated by consenting healthy volunteers. 10 mL of heparinized blood were diluted with 0.9 % NaCl solution to achieve a final volume of 100 mL. 13 mL of Biocoll® separating solution were put into a 50 mL falcon tube and 35 mL of diluted blood was added on top of the Biocoll® layer. Then, samples were centrifuged at 800×g for 15 minutes with the deceleration ramp set to 1. The layer containing the cells was collected into clean falcon tubes and washed once with 0.9 % NaCl, filling the tubes to a final volume of 50 mL. Samples were centrifuged at 450×g for 10 minutes and the supernatant was discarded. 10 mL of 1× RBC lysis buffer were added and samples were incubated for 5 minutes to allow lysis of erythrocytes. Cells were washed with ice-cold Dulbecco's Phosphate Buffered Saline (DPBS), filling the tubes to a final volume of 50 mL. Samples were centrifuged at 4 °C at 450×g for 10 minutes and the supernatant was discarded. The cell pellet was resuspended in ice-cold MACS buffer. Monocytes were isolated using CD14 MicroBeads (positive selection) or the Pan Monocyte Isolation kit (negative selection), according to the manufacturer's instructions [170, 171].

3.2.2. Isolation and differentiation of bone marrow-derived macrophages

Bone marrow cells were kindly isolated by Dr. Carlos Gomez Diaz and Dr. Ciana Diskin (AG Hornung, Ludwig-Maximilians-Universität München). Bone marrow cells were flushed from femur and tibia of wildtype C57BL/6J mice with DPBS using a syringe. The suspension was passed through a 100 µm cell strainer to remove debris. Samples were centrifuged at 400×g for 10 min. Thereafter, pellets were resuspended in 2 mL of 1× RBC lysis buffer and incubated for 2 minutes at room temperature to allow lysis of erythrocytes. Samples were centrifuged at 400×g for 10 minutes and cells were resuspended in Dulbecco's Modified Eagle Medium (DMEM) supplemented with 10 % FCS, 1 mM sodium pyruvate, 30 % L929 conditioned medium,100 U/mL penicillin and 100 µg/mL streptomycin. Cells were differentiated in non-treated culture dishes for 6 days. On the 6th day of differentiation, BMDMs were detached using DPBS containing 2 mM EDTA and re-plated for experiments.

3.2.3. Cell culture conditions

Cells were maintained in a humidified incubator at 37 °C with a CO_2 content of 5 %. Fetal calf serum (FCS) was heat-inactivated at 55 °C for 1 hour before use.
HEK 293T cells were cultivated in DMEM supplemented with 10 % FCS, 1 mM sodium pyruvate, 100 U/mL penicillin and 100 µg/mL streptomycin. BLaER2, KBM-7, THP-1 and U-937 cells were cultivated in Roswell Park Memorial Institute (RPMI) 1640 Medium supplemented with 10 % FCS, 1mM sodium pyruvate, 100 U/mL penicillin and 100 µg/mL streptomycin. HL-60 cells were cultivated in RPMI 1640 Medium supplemented with 10 % FCS, 10 mM HEPES, 1 mM sodium pyruvate, 100 U/mL penicillin and 100 µg/mL streptomycin. HMC-1.1 cells were cultivated in Iscove's Modified Dulbecco's Medium (IMDM) supplemented with 10 % FCS, 100 U/mL penicillin and 100 µg/mL streptomycin. Primary human monocytes were cultivated in RPMI 1640 medium supplemented with 2.5 % human serum, 10 mM HEPES, 1mM sodium pyruvate, 100 U/mL penicillin and 100 µg/mL streptomycin.
Cell lines were passaged every 2-3 days. THP-1, U-937 and HL-60 cells were kept at a density of $0.1\text{-}1\times10^6$ cells/mL. BLaER2 cells were kept at a density of $0.15\text{-}2\times10^6$ cells/mL. HMC-1.1 were kept at a density of $0.35\text{-}1\times10^6$ cells/mL. HEK293T cells were detached from culture vessels using 0.05 % Trypsin-EDTA.
To prepare frozen stocks, $2\text{-}5\times10^6$ cells were pelleted by centrifugation and taken up in FCS containing 10 % DMSO.

3.2.4. Differentiation of myeloid cell lines and primary human monocytes into macrophages

HL-60 and THP-1 cells were differentiated into macrophages by treating cells with 100 ng/mL phorbol 12-myristate 13-acetate (PMA) for 16 h. Undifferentiated cells were washed off using DPBS. Then, differentiated cells were detached using 2 mM EDTA/DPBS and plated for experiments. Unless indicated otherwise, cells were left to rest for 3 days before stimulation. Alternatively, cells were subjected to starvation for approx. 8 hours prior to stimulation, using culture medium containing 0.3 % FCS instead of 10 %.

U-937 cells were differentiated into macrophages by treating cells with 10 ng/mL PMA for 72 hours. 0.2×10^6 cells were plated per well on a 6-well plate. After 72 hours, medium was replaced with fresh culture medium without PMA and cells were left to rest for 1 day. Thereafter, cells were subjected to starvation for approx. 8 hours prior to stimulation, using culture medium containing 0.3 % FCS instead of 10 %.

BLaER2 cells were transdifferentiated into macrophages using 20 ng/mL IL-3, 20 ng/mL M-CSF and 100 nM β-estradiol for 5 days. To this end, cells were either directly plated in a 96-well plate using 80,000 cells/well or plated in non-treated dishes, using 5×10^6 cells per 10 cm dish. Thereafter, medium was exchanged and cells were stimulated as described below. When differentiating cells in bacterial dishes, cells were collected, pelleted and medium was replaced by regular culture medium (without cytokines and β-estradiol). Thereafter, cells were plated onto a 96-well plate for subsequent experiments, using 80,000 cells/well.

Primary human monocytes were differentiated into monocyte-derived macrophages (MDMs) using 10 ng/mL macrophage colony-stimulating factor (M-CSF) unless otherwise indicated. Non-treated 6-well plates or 10 cm dishes were used, plating 1×10^6 cells per well or $8\text{-}12 \times 10^6$ cells per dish. Fresh M-CSF was added every 2-3 days and cells were plated for experiments after 5-7 days of differentiation. To this end, cells were detached using Detachin™ Cell Detachment Solution according to the manufacturer's instructions.

3.2.5. Stimulation

HL-60 cells were stimulated as follows: Where indicated, cells were primed with 100 ng/mL IFN-γ for 2 hours. Thereafter, cells were stimulated with 200 ng/mL lipopolysaccharide (LPS) from *E. coli* or 2 µg/mL Pam$_3$CSK$_4$.

THP-1 cells were stimulated as follows: Where indicated, cells were primed with 100 ng/mL recombinant human IFN-γ for 2 hours, or with 10 ng/mL recombinant human IFN-γ for 6 hours. After priming, cells were washed once with DPBS and then stimulated with the indicated TLR-ligands for 14 hours as follows: 1 µg/mL

LPS from *E. coli*, 0.33 μg/mL Pam$_3$CSK$_4$, 2 μg/mL R848, 15 μg/mL imiquimod and 20 μg/mL poly(I:C) (high molecular weight).

U-937 cells were stimulated as follows: Where indicated, cells were pre-treated with 100 ng/mL IFN-γ for 2 hours. Thereafter, cells were stimulated using 200 ng/mL LPS or 20 μg/mL Pam$_3$CSK$_4$.

BLaER2 cells were stimulated using 200 ng/mL LPS, 2 μg/mL Pam$_3$CSK$_4$, 1 μg/mL R848, 5 μg/mL Imiquimod, 20 μg/mL poly(I:C) 6000 U/mL IFN-α2a or 10 ng/mL IFN-γ.

KBM-7 cells were stimulated using 200 ng/mL LPS or 2 μg/mL Pam$_3$CSK$_4$.

HMC-1.1 cells were stimulated using 200 ng/mL LPS, 2 μg/mL Pam$_3$CSK$_4$, 10 ng/mL IFN-γ or 6000 U/mL IFN-α2a.

MDMs were stimulated using 200 ng/mL LPS, 2 μg/mL Pam$_3$CSK$_4$, 1 μg/mL R848, 20 μg/mL poly(I:C) (HMW), 200 ng/mL TL8-506, 5 μM ODN 2006, 6000 U/mL IFN-α2a or 10 ng/mL IFN-γ.

For cytokine release measurements using ELISA and MitoSOX flow cytometry, 80,000 differentiated THP-1 cells were plated per well on a 96-well plate. Cells were left to rest for 3 days before stimulation. Where applicable, expression of transgenes was induced by adding 1 μg/mL doxycycline on the day prior to stimulation. BLaER2 cells were transdifferentiated into macrophages in non-treated 10 cm dishes and subsequently replated. Stimulation was carried out approx. 6-8 hours after re-plating. When using MDMs, 70,000 cells were plated per well on a 96-well plate. MDMs were stimulated on the day after re-plating.

THP-1 cells and BLaER2 cells were stimulated for 14 hours, MDMs were stimulated for 16 hours. Thereafter, supernatants were transferred to a 96-well U-bottom plate centrifuged at 500×g for 5 minutes to remove residual cells, transferred to a clean 96-well U-bottom plate and inactivated using 0.5 % Triton-X 100. Supernatants were either directly used or stored at -80 °C until measuring cytokines by ELISA.

For analysis by western blotting, cells were harvested in RIPA lysis buffer supplemented with cOmplete protease inhibitor. Lysates were incubated on a rotating wheel at 4 °C for 30 min, followed by centrifugation at 20,000×g at 4 °C for 5 minutes to remove debris. Alternatively, cells were harvested in 1× Laemmli buffer.

3.3. Cloning

3.3.1. RNA extraction

The coding sequence of NMES1 and NDUFA4 was cloned from cDNA derived from human MDMs. To this end, isolated human monocytes were differentiated as described in chapter 3.2.4, using 1×10^6 cells per well on a 6-well plate. Following differentiation, cells were stimulated with 200 ng/mL LPS for 14 hours to induce NMES1 expression. For cloning of NDUFA4, RNA was extracted from unstimulated MDMs. Supernatant was removed and cells were lysed in 300 µL of RLT buffer. After addition of RLT buffer, plates were sealed and frozen at -80 °C overnight. RNA extraction was performed using the Total RNA Purification Mini Spin Kit PLUS (Genaxxon). All steps were carried out at room temperature. In brief, lysates were thawed and collected into 1.5 mL tubes. Then, 300 µL of 70 % ethanol were added to the lysates, and mixtures were loaded onto RNA purification columns. Thereafter, spin columns were centrifuged at 15,000×g for 2 minutes, discarding the flow through. Spin columns were transferred to a clean collection tube and washed with 500 µL of buffer RW2, repeating the centrifugation step. DNase treatment was carried out by adding 95 µL of 1× DNase I in DNase I reaction buffer, followed by incubation at room temperature for 10 minutes. Columns were washed with 600 µL of buffer RW1 and centrifuged at 15,000×g for 30 seconds. Then, columns were washed with 500 µL of buffer RW2, repeating the centrifugation step. Columns were washed with buffer RW2 a second time, this time using 300 µL of buffer RW2 and centrifuging at 15,000×g for 2 minutes. Finally, spin columns were transferred to clean 1.5 mL tubes for elution. After applying 30 µL of water to the center of the columns, columns were incubated at room temperature for 5 minutes. Eluates were collected by centrifugation at 8,000×g for 2 minutes.

RNA concentrations were determined using a NanoDrop 1000 spectrophotometer. RNA was used directly for cDNA synthesis or stored at -80 °C until further use.

3.3.2. cDNA synthesis

cDNA synthesis reactions were set up as described in Table 9. Reactions were incubated in a thermocycler at 42 °C for 1 hour. Thereafter, enzymes were inactivated by incubation at 70 °C for 10 minutes. cDNA was stored at -20 °C until further use.

Table 9. cDNA synthesis reaction.

Reagent	Volume
Water	To make 10 µL total volume
Template RNA	Up to 5.5 µL, maximum 1 µg of RNA
Oligo dT primer	0.5 µL
5× reaction buffer	2 µL
RiboLock RNase Inhibitor (20×)	0.5 µL
dNTP mix (10 µM)	1 µL
RevertAid reverse transcriptase	0.5 µL

3.3.3. Polymerase chain reaction (PCR)

Insert DNA was amplified from cDNA or purified plasmid DNA. To this end, PCR reactions were set up as described in Table 10. Primer sequences are listed in Table 3. PCR was carried out using a C1000 Touch Thermal Cycler (BioRad), using the settings described in Table 11.

Table 10. PCR reaction.

Reagent	Volume
Water	To make 60 µL total volume
Buffer GC	12 µL
dNTPs (10 mM)	1.2 µL
Forward primer (10 µM stock)	3 µL
Reverse primer (10 µM stock)	3 µL
Phusion high-fidelity DNA polymerase	0.6 µL
cDNA template/plasmid DNA (1 ng/µL)	1 µL/10 µL

Table 11. PCR settings.

Step	Temperature	Duration	Cycles
Initial denaturation	98 °C	3 min	1×
Denaturation	98 °C	10 sec	30×
Annealing	60 °C	30 sec	
Extension	72 °C	30 sec/1kb	
Final extension	72 °C	7 min	1×
Hold	12 °C		1×

PCR products were mixed with 6.6 µL of 10× FastDigest Green buffer and loaded onto a 0.8-2 % agarose gel, depending on the size of the PCR product. Agarose gels were analyzed using a ChemiDoc MP imaging system (Bio-Rad). DNA was purified from gel using the QIAquick gel extraction kit (Qiagen) according to the manufacturer's instructions [172].

3.3.4. Restriction enzyme cloning

Insert and target vector were digested using FastDigest enzymes for 3 hours at 37 °C. NheI and BamHI were used, or, if necessary, inserts were digested using enzymes generating compatible ends. Digested vectors were applied onto a 0.8 % agarose gel. Agarose gels were analyzed using a ChemiDoc MP imaging system (Bio-Rad). Bands were excised and DNA was purified from gel using the QIAquick gel extraction kit (Qiagen) according to the manufacturer's instructions [172]. Digested inserts were purified using the QIAquick PCR purification kit (Qiagen) according to the manufacturer's instructions [172]. Ligation was carried out using T4 ligase. The components of the ligation reaction are listed in Table 12. Ligation mixes were incubated in a PCR cycler using the settings described in Table 13. The resulting product was used to transform competent *E. coli* as described below (see 3.3.7).

Table 12. Ligation reaction using T4 ligase.

Reagent	Volume
Digested vector	50 ng
Digested insert	x µL (1:3 molar ratio vector:insert)
T4 ligase buffer (10×)	2 µL
T4 ligase	1 µL
Water	x µL (to make 20 µL final volume)

Table 13. Ligation reaction settings.

Step	Temperature	Duration	Cycles
Step 1	16 °C	15 min	2×
Step 2	22 °C	15 min	
Step 3	70 °C	5 min	1×
Hold	12 °C		1×

3.3.5. Gibson assembly

The target vector was digested as described above (see chapter 3.3.4). PCR products were generated and gel purified as described in chapter 3.3.3. The Gibson assembly reaction was set up as described in Table 14 and incubated at 50 °C for 1 hour. The resulting product was used to transform competent *E. coli* as described below (see chapter 3.3.7).

Table 14. Gibson assembly reaction.

Reagent	Volume
Digested vector	75 ng
Insert	x µL (1:2 molar ratio vector:insert)
Gibson Master mix	15 µL
Water	x µL (to make 20 µL final volume)

3.3.6. Ligation independent cloning

Vectors for plasmid-mediated CRISPR/Cas9 genome editing were generated by ligation independent cloning (LIC). gRNAs were designed using the online tools provided by Synthego, IDT, or Benchling [173-175]. DNA oligos consisting of the gRNA sequence flanked by adapters for LIC were ordered from IDT. pMini_U6_gRNA_CMV_mCherry_T2A_Cas9 was digested using SpeI and ApaI, run on an agarose gel and purified using the QIAquick gel extraction kit (Qiagen) according to the manufacturer's instructions [172]. Overhangs were generated making use of the 3'-5' exonuclease activity of T4 DNA polymerase in presence of dTTP. The reaction components are listed in Table 15.

Table 15. Reaction to generate overhangs using T4 DNA polymerase.

Reagent	Volume
Digested vector	700 ng
dTTP (100 mM)	1 µL
BSA (10 mg/mL)	1 µL
10× NEB2 Buffer	10 µL
T4 DNA polymerase (3 U/µL)	3.33 µL
Water	x µL (to make 100 µL final volume)

The reaction was incubated at 27 °C for 5 minutes and then put on ice, followed by inactivation at 75 °C for 5 minutes. Thereafter, a master mix for ligation independent cloning was generated, using the components listed in Table 16.

Table 16. Components of the master mix for ligation independent cloning.

Reagent	Volume
Digested vector (with overhangs)	10 µL
10× NEB2 Buffer	20 µL
LICsgRNA_rev (100 µM; PAGE purified)	0.5 µL
Water	69.5 µL

2.5 µL of this master mix were mixed with 2.5 µL of the desired gRNA sequence containing oligo (0.25 µM). Assembly was carried out using the settings described in Table 17. The resulting product was used to transform competent *E. coli* as described below (see chapter 3.3.7).

Table 17. Assembly of plasmids using ligation independent cloning.

Temperature	Duration	Ramp	Cycles
70 °C	1 min	0.1 °C/sec	1×
65 °C	1 min	0.1 °C/sec	1×
60 °C	30 min	0.1 °C/sec	1×
55 °C	2 min 30 sec	0.1 °C/sec; -1 °C/cycle	29×
25 °C	hold		1×

3.3.7. Transformation into E. coli

Newly generated plasmids were transformed into Dh5α competent *E. coli*. In the case of pLI_dCas9-VPR_hygro, the TOP10 strain was used. A 20 µL aliquot of competent bacteria was thawed on ice. Thereafter, 4 µL of ligation mix were added, followed by incubation on ice for 30 minutes. Heat shock was carried out at 42 °C for 45 seconds, followed by incubation on ice for 2 minutes. 180 µL of LB medium without antibiotics were added and samples were incubated on a shaker at 37 °C for 45-60 minutes. Finally, bacteria were plated onto LB agar plates containing the appropriate antibiotic. Plates were incubated at 37 °C overnight.

3.3.8. Colony PCR

Colony PCR was carried out using GoTaq® G2 DNA Polymerase. PCR tubes containing 6.75 µL of water were prepared. Colonies were picked using a pipette tip and partially transferred to the PCR tubes by stirring briefly. Pipette tips were then transferred to tubes containing LB medium supplemented with the appropriate antibiotic. Tubes were incubated in a bacterial shaker at 120 rpm at 37 °C overnight. A master mix was prepared using primers complementary to the backbone of the vector used. Components of the master mix are listed in Table 18. Primer sequences are listed in Table 3. 3.25 µL of master mix were added per tube and PCR was performed as described in Table 19.

Table 18. Colony PCR reaction.

Reagent	Volume per reaction
5× Green GoTaq Reaction buffer	2 µL
dNTPs	0.2 µL
GoTaq G2 DNA polymerase (5 U/µL)	0.05 µL
Forward primer (10 µM)	0.5 µL
Reverse primer (10 µM)	0.5 µL

Table 19. Colony PCR settings.

Step	Temperature	Duration	Cycles
Initial denaturation	94 °C	3 min	1×
Denaturation	94 °C	30 sec	
Annealing	60 °C	30 sec	30×
Extension	72 °C	1 min/1kb	
Final extension	72 °C	5 min	1×
Hold	12 °C		1×

3.3.9. Isolation of plasmid DNA

Plasmid DNA was isolated on a small scale to identify colonies that carry the correct insert: 6 mL of bacterial culture were set up overnight, using LB medium containing the appropriate antibiotic. Bacteria were pelleted by centrifugation at 3200×g for 5 minutes. Thereafter, pellets were taken up in 250 µL of buffer P1. Next, 250 µL of buffer P2 were added and tubes were inverted several times. Then, 350 µL of buffer N3 were added to precipitate protein. Bacterial lysates were centrifuged at 18,000×g for 10 minutes. Supernatants were transferred to spin columns, followed by centrifugation at 13,000×g for 1 minute. Spin columns were washed once with 750 µL of buffer PE, and then subjected to a dry spin, repeating the centrifugation step at 13,000×g each time. Plasmid DNA was eluted using 50 µL of water.

Midiprep quality plasmid DNA was used for lentiviral particle production. To this end, plasmid DNA was purified using the PureLink^{TM} HiPure Plasmid Midiprep Kit according to the manufacturer's instructions [176].

DNA concentrations were determined using a NanoDrop 1000 spectrophotometer. Isolated plasmid DNA was stored at -20 °C.

Frozen stocks of bacteria were prepared by mixing a fresh overnight culture with sterile filtered 50 % glycerol solution at a ratio of 1:1. Bacterial stocks were stored at -80 °C.

3.4.   Production of lentiviral particles and transduction of target cells

Pseudotyped lentiviral particles were produced using a third-generation lentiviral packaging system. To this end, reverse transfection of HEK293T cells was carried out. A DNA mix containing 1 µg of transfer plasmid, 1.5 µg of pMDLg/pRRE, 0.5 µg of pRSV-rev and 1 µg of VSV-g was prepared in 200 µL of OptiMEM. In a separate tube, 10.6 µL of a 1mg/mL stock solution of Polyethylenimine HCl MAX (PEI) were added to 200 µL of OptiMEM, mixed by vortexing and incubated at room temperature for 5 min. Thereafter, 200 µL of PEI dilution in OptiMEM were added to 200 µL of DNA mix, followed by incubation at room temperature for 25 min. A cell suspension containing $2×10^6$ HEK293T cells/mL was prepared in culture medium and 1 mL of this suspension was added per well of a 6-well plate. Thereafter, 350 µL of the transfection mix were added to each well, resuspending gently by pipetting. Plates were placed in an incubator at 37 °C with a CO_2 content of 5 %. Medium was replaced approximately 8 hours after transfection, adding 1 mL of culture medium per well. Viral particles were harvested 3 days after transfection. To this end, supernatants were passed through a 0.45 µm filter. Viral supernatants were either used directly for transduction or stored at -80 °C.

Transduction of THP-1 and U-937 cells was carried out as follows: Per well of a 6-well plate, 1 mL of a suspension containing $1×10^6$ cells/mL was mixed with 1 mL of viral supernatant. Furthermore, protamine sulfate was added to a final

concentration of 10 µg/mL. Cells were centrifuged at 1200×g for 1.5 hours with the acceleration and deceleration ramp set to 1. Thereafter, cells were incubated for 24 hours before exchanging the culture medium. Selection using 5 µg/mL of the appropriate antibiotic (puromycin or blasticidin) was started two days after transduction. Selection medium was renewed every other day and replaced by regular medium after 4-5 days of selection.

Transduction of BLaER2 cells was carried out as follows: Per well of a 6-well plate, 0.5 mL of a suspension containing $1×10^6$ cells/mL was mixed with 0.5 mL of viral supernatant. Thereafter, cells were incubated for 24 hours before exchanging the culture medium. Selection using the 1.25 µg/mL of puromycin was started two days after transduction. Selection medium was renewed every other day and replaced by regular medium after 4-5 days of selection.

Transduction of HEK293T cells was carried out as follows: HEK293T cells were seeded at a density of 250,000 cells/well on a 6-well plate. Approximately 6 hours after plating, viral supernatant was added to achieve dilutions ranging from 1:2 to 1:40. Thereafter, cells were incubated for 24 hours before exchanging the culture medium. Cells were left to grow for 3 days and then transferred to T25 flasks in order to reduce density below 80 %. The following day, culture medium was replaced by medium supplemented with 5 µg/mL of puromycin. Selection medium was replaced by regular medium after 2 days of selection.

3.5. Generation of stable cell lines using the PiggyBac transposon system

To generate BLaER2 cells stably expressing a hybrid VP64-p65-Rta (VPR) tripartite activator fused to endonuclease-dead Cas9 (dCas9), the PiggyBac transposon system was used. $2.5×10^6$ BLaER2 cells were taken up in 250 µL of OptiMEM and 4.5 µg of PB-TRE-dCas9-VPR and 1 µg of pTwist_CMVbg_mCherry_T2A_FLAG-hypPB_Neo (encoding hyperactive PiggyBac transposase) were added. The mixture was incubated at room temperature for 15 minutes. Thereafter, the mixture was transferred to an electroporation cuvette (4 mm gap size). Electroporation was carried out using a Gene Pulser Xcell Electroporation System (Bio-Rad), using an exponential decay protocol at 265 V, 975 µF and 700 Ω. Immediately after electroporation, cells were transferred into a 6-well plate containing pre-warmed culture medium. 72 hours after electroporation, cells were subjected to hygromycin selection, using 150 µg/mL hygromycin. This was previously determined to be a suitable concentration for selection of BLaER2 cells in a dose-response experiment. Selection medium was replaced every 2 days and removed after 10 days of selection.

3.6.   Genome editing using CRISPR/Cas9

3.6.1. Genome editing by nucleofection with ribonucleoproteins

For primary human monocytes and THP-1 cells, genome editing using CRISPR/Cas9 was carried out by nucleofecting cells with ribonucleoproteins (RNPs) assembled *in vitro*. When working with knock-out pools, two or three crRNAs targeting the same gene were used to increase knock-out efficiency. crRNA sequences are listed in Table 6. crRNAs and tracrRNA were reconstituted in IDT duplex buffer to yield 200 µM stock solutions. Reconstituted crRNAs and tracrRNA were stored at -80 °C. Annealing of crRNA and tracrRNA was carried out by incubating mixtures at 95 °C for 5 minutes, followed by incubation at room temperature for 30 minutes. For each reaction, 100 pmol (= 0.5 µL) of crRNA were mixed with 100 pmol of tracrRNA. When using more than one crRNA, annealing was carried out in a single tube, using 100 pmol of each crRNA and an equal amount of tracrRNA. After annealing of crRNA and tracrRNA, Alt-R$^®$ S.p. Cas9 Nuclease V3 was added, followed by incubation at room temperature for 10 minutes to allow assembly of the RNA-protein complex. 40 pmol of Alt-R$^®$ S.p. Cas9 Nuclease V3 were added per each crRNA used. Assembled RNPs were stored at -80 °C until further use or used directly.

For nucleofection of primary human monocytes, monocytes were isolated from PBMCs using the Pan Monocyte Isolation Kit (Miltenyi Biotec). Nucleofection was carried out using the P3 Primary Cell 96-well Nucleofector^{TM} Kit (Lonza). Per nucleofection cuvette, $4×10^6$ cells were used. Cells were washed with PBS and resuspended in 20 µL of P3 Primary Cell Nucleofection Solution supplemented with Supplement 1. The cell suspension was then mixed with the assembled RNPs and transferred to a nucleofection cuvette. Nucleofection was carried out using the program EH-100 on a 4D-Nucleofector X Unit (Lonza). Cells were taken up in culture medium without serum and incubated for 30 minutes. Thereafter, an equal volume of culture medium containing 5 % of human serum were added to achieve a final concentration of 2.5 %. Cells were differentiated as described in chapter 3.2.4.

For nucleofection of THP-1 cells, the SG cell line 4D-Nucleofector X Kit (Lonza) was used. Per nucleofection cuvette, $5×10^5$ cells were used. Cells were washed with PBS and resuspended in 20 µL of SG Cell Line Nucleofection Solution supplemented with Supplement 1. The cell suspension was then mixed with the assembled RNPs and transferred to a nucleofection cuvette. Nucleofection was carried out using the program DV-100 on a 4D-Nucleofector X Unit (Lonza). Finally, cells were taken up in 250 µL of culture medium. On the next day, cells were diluted to a final volume of 1 mL, counted and, if applicable, plated at a density of 1 cell/well on a U-bottom 96-well plate for generation of single cell clones.

3.6.2. Determining the knock-out efficiency for knock-out pools

When working with knock-out pools, the knock-out efficiency was determined using Sanger Sequencing. To this end, primers flanking the edited genomic region were designed using Primer3Plus [177, 178]. Primer sequences are listed in Table 3. $0.5\text{-}1\times10^5$ cells were harvested in direct lysis buffer supplemented with proteinase K. Samples were incubated at 65 °C for 10 minutes, then proteinase K was inactivated by incubating for 15 minutes at 95 °C. PCR reactions were set up as described in Table 20. PCR was performed as described Table 21.

Table 20. PCR reaction for amplifying genomic DNA.

Reagent	Volume
Water	12.58 µL
Buffer GC	5 µL
dNTPs (10 mM)	0.5 µL
Forward primer (10 µM stock)	1.25 µL
Reverse primer (10 µM stock)	1.25 µL
Phusion high-fidelity DNA polymerase	0.25 µL
Lysate	4.16 µL

Table 21. PCR settings for amplifying genomic DNA.

Step	Temperature	Duration	Cycles
Initial denaturation	98 °C	1 min 30 sec	1×
Denaturation	98 °C	20 sec	
Annealing	60 °C	20 sec	30×
Extension	72 °C	20 sec	
Final extension	72 °C	3 min	1×
Hold	12 °C		1×

PCR products were purified using the QIAquick PCR purification kit (Qiagen) according to the manufacturer's instructions [172]. Samples were submitted for Sanger Sequencing using the sequencing primer "MiSeq adapter fwd" (see Table 3). Sequencing results were analyzed using the Interference of CRISPR Edits (ICE) analysis tool [179].

3.6.3. Genome editing by transfection or electroporation with plasmid DNA

Plasmid-mediated CRISPR/Cas9 genome editing was carried out in HEK293T and BLaER2 cells. Plasmids used were generated as described in chapter 3.3.6.
1×10^6 HEK293T cells were plated per well on a 6-well plate on the day prior to transfection. The transfection reaction was set up as follows: Per well, 3 µg of plasmid DNA were diluted in 250 µL of OptiMEM. 6 µL of GeneJuice transfection reagent were added dropwise to 250 µL of OptiMEM, mixed thoroughly by

vortexing and incubated on ice for 5 minutes. Thereafter, the transfection reagent mix was added to the plasmid DNA dilution, followed by incubation at room temperature for 20 minutes. Finally, the transfection mix was added dropwise to the well. 24 hours after transfection, cells were detached using trypsin, washed with PBS and taken up in FACS buffer.

2.5×10^6 BLaER2 cells were taken up in 250 µL of OptiMEM and 5 µg of plasmid DNA were added. The mixture was incubated at room temperature for 15 minutes. Thereafter, the mixture was transferred to an electroporation cuvette (4 mm gap size). Electroporation was carried out using a Gene Pulser Xcell Electroporation System (Bio-Rad), using an exponential decay protocol at 265 V, 975 µF and 700 Ω. Immediately after electroporation, cells were transferred into a 6-well plate containing pre-warmed culture medium. 24 hours after electroporation, cells were collected and taken up in FACS buffer.

For sorting, the cell suspension was transferred into a strainer-capped FACS tube. mCherry positive cells were sorted using a FACSAria Fusion cell sorter (BD Biosciences). To generate single cell clones, HEK293T and BLaER2 cells were plated using 4, 2 or 1 cell(s) per well on a F-bottom or U-bottom 96-well plate, respectively. Cells were left to grow for 3-4 weeks. Thereafter, wells containing clones were identified by measuring absorbance at 600 nm using a Spark20M microplate reader (Tecan). As many clones as possible, or a maximum of 96 clones, were picked and transferred to a 96-well plate using a Biomek FX Automated Liquid Handler (Beckman Coulter). Alternatively, cells were transferred by hand.

3.6.4. Screening for knock-out clones by genotyping

Successfully edited clones were identified using Illumina Sequencing. To this end, primers flanking the edited genomic region were designed using Primer3Plus [177, 178]. Primer sequences are listed in Table 3. Primers were designed to yield an amplicon of approx. 250 bp in length and contain a 5' overhang which serves as an adapter in the subsequent second PCR reaction. In the second PCR reaction, barcode primers are used to assign reads to their respective well of origin.

10 µL of cell suspension were taken from the plate containing picked clones described above and transferred to a 96-well PCR plate containing 10 µL of 2× direct lysis buffer supplemented with proteinase K. Samples were incubated at 65 °C for 10 minutes, then proteinase K was inactivated by incubating for 15 minutes at 95 °C. The PCR reaction for amplifying the genomic region of interest was set up as described in Table 22. PCR was performed as described in Table 21, but running only 18 instead of 30 cycles.

Table 22. PCR1 for identifying knock-out clones by genotyping.

Reagent	Volume
Water	3.5 µL
Buffer GC	1.2 µL
dNTPs (10 mM)	0.12 µL
Forward primer (10 µM stock)	0.06 µL
Reverse primer (10 µM stock)	0.06 µL
Phusion high-fidelity DNA polymerase	0.06 µL
Lysate	1 µL

For the second PCR reaction using barcode primers, the PCR reaction was set up as described in Table 23. PCR was performed as described in Table 21, but running only 18 instead of 30 cycles.

Table 23. PCR2 for identifying knock-out clones by genotyping.

Reagent	Volume
Water	3.92 µL
Buffer GC	1.2 µL
dNTPs (10 mM)	0.12 µL
Barcode primer mix (2.5 µM)	1.2 µL
Phusion high-fidelity DNA polymerase	0.06 µL
PCR product from PCR1	1 µL

The resulting PCR products were pooled, purified from an agarose gel. The subsequent steps were kindly carried out by Dr. Niklas Schmacke (AG Hornung, Ludwig-Maximilians-Universität München): Nucleic acids were precipitated by mixing samples with 3M sodium acetate (pH 5.2), using an amount corresponding to 10 % of the sample volume. Isopropanol was added using an amount corresponding to 110 % of the sample volume and the mixture was incubated at -20 °C for 30 minutes. Thereafter, samples were centrifuged at 4 °C at 14,000×g for 15 minutes. The pelleted DNA was then washed with ice-cold 70 % (v/v) ethanol, followed by centrifugation at 4 °C at 14,000×g for 5 minutes. The pellet was air-dried and resuspended in water. The DNA concentration was determined using a NanoDrop 1000 spectrophotometer. Sequencing was performed using a MiSeq™ system (Illumina). 300 bp length single read sequencing was carried out using the MiSeq reagent kit v2.

Sequencing results were analyzed using the online tool OutKnocker [180]: FastQ files were searched for the amplicon of interest and compared to the wildtype reference sequence. Clones with two differentially edited alleles with out-of-frame mutations were identified as true single cell knock-out clones. Therefore, these two editing events should contribute to approx. 50 % of all reads. Alternatively, clones with a single out-of-frame mutation event contributing to close to 100 % of reads were selected. The selected clones were expanded and used for experiments.

3.7. Enzyme-linked immunosorbent assay (ELISA)

Release of IL-6 and TNF was quantified using enzyme-linked immunosorbent assays (BD Biosciences). High-binding ELISA plates were coated using 50 µL of capture antibody diluted 1:500 in ELISA coating buffer. Plates were incubated at 4 °C overnight. Thereafter, plates were washed 3× with PBS-T and blocking was carried out using 50 µL of blocking buffer (10 % FCS/DPBS) using a BioTek 405 Touch microplate washer (BioTek). Plates were incubated at room temperature for 1 hour. A serial dilution of standard was prepared in blocking buffer. Samples were diluted in blocking buffer to obtain values within the range of the standard curve. After blocking, ELISA plates were washed 3× with PBS-T and 50 µL of diluted samples or standard was added per well. Plates were incubated at room temperature for 2 hours and then washed 5× with PBS-T. Thereafter, 50 µL of a 1:500 dilution of detection antibody and streptavidin-HRP conjugate in blocking buffer were added per well. Plates were incubated at room temperature for 1 hour. Subsequently, plates were washed 5× with PBS-T and 50 µL of substrate solution were added per well. Finally, plates were incubated protected from light and developing reaction was stopped by the addition of 50 µL of 10 % sulfuric acid. Absorbance was measured at 450 nm and 570 nm using a Gen5-Epoch microplate reader (BioTek).

ELISA data were evaluated in RStudio, using a four-parameter logistic regression model to generate the standard curve [181]. The R script was kindly provided by Gunnar Kuut (AG Hornung, Ludwig-Maximilians-Universität München) [182].

3.8. BCA assay

BCA assay was carried out using the Pierce BCA Protein Assay Kit. Bovine serum albumin (BSA) standards were prepared by diluting the supplied stock solution with water as described in the manufacturer's instructions [183].

Samples were diluted with water on a 96-well U-bottom plate to obtain values within the range of the standard curve. 5 µL of diluted sample or BSA standard were used per well. Working reagent was prepared by mixing reagent A:B at a ratio of 50:1. 100 µL of working reagent were added to each well, and the plate was incubated at 37 °C for 30 minutes. Absorbance was measured at 562 nm using a Spark20M microplate reader (Tecan). Protein concentrations were calculated in Microsoft Excel, using the formula of the linear trend line obtained for the standard curve.

3.9. SDS-PAGE

RIPA lysates were diluted using DPBS or RIPA buffer to adjust total protein concentrations. Thereafter, samples were mixed with 6× Laemmli sample buffer and boiled at 95 °C for 5 minutes. Alternatively, cells were directly lysed in 1× Laemmli sample buffer and boiled at 95 °C for 5 minutes. When downstream

analysis included staining for MTCO1, samples were instead boiled at 70 °C for 20 min. SDS-PAGE was carried out using 12 % or 4-12 % bis-tris gels and 1× NuPAGE MOPS SDS running buffer. Equal volumes of sample were loaded. PageRuler™ Prestained Protein Ladder (10 to 180 kDa) was loaded as a reference. Electrophoresis was carried out on ice at 120 V for approximately 2 hours.

3.10. Mitochondria isolation

Mitochondria were isolated from MDMs or human cell lines using the Human Mitochondria Isolation Kit (Miltenyi Biotec). In brief, where applicable, cells were treated with 1 μg/mL doxycycline for 24 hours, unless otherwise indicated. $1×10^7$ cells were washed once with DPBS and taken up in 1 mL of lysis buffer supplemented with cOmplete™ protease inhibitor. Homogenization was carried out using a syringe, performing sets of 5 strokes each as follows: For HEK293T cells, 35 strokes using a 26G needle were performed. For MDMs and THP-1 cells, 40 strokes using a 29G needle were performed. Cells were counted after the indicated amounts of strokes and another set of 5 strokes was carried out if samples still contained more than $1×10^5$ viable cells. Lysates were diluted to a volume of 10 mL with 1× separation buffer and incubated with 50 μL of anti-TOMM22 MicroBeads at 4 °C for 1 hour. Magnetically labelled mitochondria were isolated using LS columns. Subsequently, isolated mitochondria were centrifuged at 4 °C at 13,000×g for 2 minutes. Mitochondrial pellets were washed using 1,800 μL of storage buffer, repeating the centrifugation step. Thereafter, mitochondrial pellets were taken up in 200 μL of storage buffer and 10 μL of the suspension were set aside for BCA assay (see chapter 3.8). The remaining volume was pelleted by repeating the centrifugation step described above and pellets were frozen at -80 °C until performing blue native PAGE (BN PAGE).

3.11. Blue native PAGE

BN PAGE was carried out on isolated mitochondria, using the NativePAGE™ Novex® Bis-Tris Gel System. The procedure was carried out according to the manufacturer's instructions [184]. In brief, total amounts of mitochondrial protein were determined by BCA assay (see chapter 3.8). Frozen mitochondrial pellets were thawed on ice and solubilized in 1× NativePAGE™ sample buffer supplemented with cOmplete protease inhibitor and digitonin. For each experiment, the required digitonin concentration was determined based on the sample with the lowest protein concentration. Samples were taken up in different volumes of the same sample buffer preparation in order to achieve the same digitonin to protein ratio for all samples. Unless indicated otherwise, the digitonin to protein ratio used was 6 g/g. Samples were incubated on ice for 15 minutes and

insoluble components were removed by centrifugation at 4 °C at 20,000×g for 30 minutes. Supernatants were transferred to 1.5 mL tubes. G-250 sample additive was added to achieve a final concentration corresponding to 1/4th of the digitonin concentration used. 25 µL of sample were loaded per lane, corresponding to 50-100 µg of mitochondrial protein. Equal amounts of mitochondrial protein were loaded for each sample. 5 µL of NativeMark were loaded as a reference.

BN PAGE was carried out using NativePAGE™ Novex® 4-16 % bis-tris gels. Electrophoresis was performed using dark blue cathode buffer until the running front reached the first third of the gel. Thereafter, dark blue cathode buffer was replaced with light blue cathode buffer and the gel was run until the running front reached the bottom of the gel. Electrophoresis was carried out at 150 V for approximately 2 hours in total. Thereafter, western blotting was carried out as described below (see chapter 3.12). Where indicated, lanes were excised and subjected to second dimension SDS-PAGE.

Excised lanes were prepared for second dimension SDS-PAGE according to the manufacturer's instructions [184]. Thereafter, second dimension SDS-PAGE was run using 1× NuPAGE MOPS SDS running buffer. Electrophoresis was carried out on ice at 120 V for approximately 2 hours.

3.12. Western blot

Following regular SDS-PAGE or second dimension SDS-PAGE, proteins were blotted onto a 0.2 µm nitrocellulose membrane. Wet transfer was performed using 1× tris-glycine buffer containing 20 % ethanol. Gels were soaked in 1× tris-glycine buffer containing 20 % ethanol for 5 minutes before assembling the gel sandwich. Transfer was carried out at 4 °C at 100 V for 50 minutes. After transfer, membranes were rinsed with PBS-T and stained with Ponceau S solution. Membranes were then destained by washing with PBS-T and blocking and antibody staining was performed as described below.

Following BN PAGE, proteins were blotted onto a 0.2 µm PVDF membrane. Membranes were activated in methanol for 30 seconds and rinsed with water for 1-2 minutes. Then, membranes were soaked transfer buffer for 5 minutes prior to assembling the gel sandwich. Wet transfer was performed using 1× NuPAGE transfer buffer containing 20 % ethanol. Gels were rinsed in 1× NuPAGE transfer buffer containing 20 % ethanol for 5 minutes prior to assembling the gel sandwich. Transfer was carried out at 4 °C at 150 mAmp for 1.5 hours. Thereafter, PVDF membranes were briefly rinsed in PBS-T and subjected to Coomassie staining to visualize the bands of NativeMark. The position of the bands was marked using a pen and membranes were destained completely. Thereafter, membranes were rinsed three times in deionized water.

Blocking was carried out using 3 % milk/PBS-T for at least 1 hour at room temperature. Alternatively, 5 % BSA/TBS-T or 5 % BSA/PBS-T was used for membranes that would be stained for phospho-antigens or Strep-tag, respectively. Thereafter, membranes were incubated with 5 mL of a primary antibody dilution at room temperature for 1 hour or at 4 °C overnight. After incubation with the primary antibody, membranes were washed three times with PBS-T (or TBS-T, if staining for phospho-antigens). Membranes were incubated with the appropriate secondary antibody dilution at room temperature for 1 hour. Secondary antibodies were diluted in 3 % milk/PBS-T, or, if staining for phospho-antigens, in 5 % BSA/TBS-T. Dilution factors of different antibodies are shown in Table 7. After staining with secondary antibodies, membranes were again washed three times with the appropriate wash buffer.

Bands were detected using Immobilon Forte Western HRP Substrate or Pierce ECL Western blotting substrate. Images were taken using a Fusion XF imaging system (Vilber).

3.13. Metabolic activity assays

XF 96-well plates were coated with 0.01 % poly-L-ornithine solution diluted 1:10 in DPBS, using 50 µL per well. Plates were incubated at 37 °C overnight and washed three times with DPBS.

For experiments using primary MDMs, monocytes were isolated, if applicable, subjected to genome editing, and plated for differentiation as described above (see chapters 3.2.1, 3.2.4 and 3.6). On the day prior to conducting the assay, 50,000 cells/well were plated on an XF 96-well plate coated with poly-L-ornithine. Where applicable, cells were stimulated using 200 ng/mL LPS.

For experiments using BMDMs, cells were isolated and differentiated as described above (see chapter 3.2.2) 70,000 cells/well were plated in an XF 96-well plate coated with poly-L-ornithine. On the following day, where applicable, cells were stimulated using 200 ng/mL LPS.

For experiments using THP-1 cells, cells were differentiated as described above (see chapter 3.2.4). 50,000 cells/well were plated on an XF 96-well plate coated with poly-L-ornithine and left to rest for 2-3 days. Where indicated, cells were primed with IFN-γ for 6 hours, followed by overnight stimulation with 2 µg/mL R848, or stimulated overnight with 0.33 µg/mL Pam$_3$CSK$_4$ without IFN-γ priming.

For experiments using HEK293T cells, 5,000 cells/well were plated on an XF 96-well plate coated with poly-L-ornithine two days prior to performing the assay. Where applicable, transgene expression was induced by adding 1 µg/mL doxycycline approx. 24 hours prior to performing the assay.

Assays were carried out using a Seahorse XFe96 Extracellular Flux analyzer (Agilent).

3.13.1.   Mitochondrial stress test

Both the appropriate cell density and the appropriate concentration of carbonyl cyanide 4-(trifluoromethoxy)phenylhydrazone (FCCP) were determined in a preliminary experiment. The mitochondrial stress test was carried out as described in the manufacturer's instructions [185]. In brief, cells were washed twice with Seahorse XF RPMI medium supplemented with 10 mM glucose, 1 mM pyruvate and 2 mM glutamine. For HEK293T cells, Seahorse XF DMEM was used instead of RPMI. Thereafter, 180 µL of supplemented medium were added to each well. Brightfield images were acquired using a Cytation 1 cell imaging multimode reader (BioTek). Then, the assay was carried out, sequentially injecting the following compounds to achieve the final concentrations as indicated: (1) 1.5 µM oligomycin, (2) 1 µM FCCP, (3) 0.5 µM rotenone and 0.5 µM antimycin A, and (4) 8 µM Hoechst. Finally, fluorescence images were acquired using a Cytation 1 cell imaging multimode reader (BioTek). Data were normalized by cell counts and wells for which the imaging had failed were excluded from the analysis.

3.13.2.   Complex IV activity measurements

Complex IV activity was measured using the XF plasma membrane permeabilizer. The experimental setup was adapted from the manufacturer's instructions and Salabei *et al.* [186, 187]. In brief, brightfield images were acquired using a Cytation 1 cell imaging multimode reader (BioTek). Thereafter, cells were quickly washed twice with 1× MAS buffer supplemented with 0.4 % fatty acid free BSA. Then, 180 µL of 1× MAS buffer supplemented with 0.4 % fatty acid free BSA, 1 nM XF plasma membrane permeabilizer and 1 mM ADP were added per well. The assay was carried out by sequentially injecting the following compounds to achieve the final concentrations as indicated: (1) 2 µM antimycin A, (2) 500 µM N,N,N',N'-Tetramethyl-1,4-phenylenediamine (TMPD), 2 mM ascorbate and 1 µM FCCP, (3) 1.5 µM oligomycin A, and (4) 20 mM potassium azide and 8 µM Hoechst. Finally, fluorescence images were acquired using a Cytation 1 cell imaging multimode reader (BioTek). All data were normalized by cell counts and wells for which the imaging had failed were excluded from the analysis. To calculate CIV activity, the following formula was used:

$$CIV\ activity = (max.\ OCR\ after\ TMPD\ inj.)–(min.\ OCR\ after\ azide\ inj.)$$

3.13.3.   Glycolysis stress test

On the day prior to running the assay, the culture medium was replaced with culture medium as described in chapter 3.2.3, but without sodium pyruvate. The glycolysis stress test was carried out as described in the manufacturer's instructions [188]. In brief, cells were washed twice with Seahorse XF RPMI medium supplemented with

2 mM glutamine. Thereafter, 180 µL of supplemented medium were added to each well. Brightfield images were acquired using a Cytation 1 cell imaging multimode reader (BioTek). Then, the assay was carried out, sequentially injecting the following compounds to achieve the final concentrations as indicated: (1) 10 mM glucose, (2) 1.5 µM oligomycin, (3) 50 mM 2-DG and 8 µM Hoechst. Finally, fluorescence images were acquired using a Cytation 1 cell imaging multimode reader (BioTek). All data were normalized by cell counts and wells for which the imaging had failed were excluded from the analysis.

To calculate glycolysis, glycolytic capacity and glycolytic reserve, the following formulas were used:

$$Glycolysis = (max.\ ECAR\ before\ Oligomycin\ inj.)–(last\ ECAR\ before\ Glucose\ inj.)$$

$$Glycolytic\ capacity = (max.\ ECAR\ after\ Oligomycin\ inj.)–(last\ ECAR\ before\ Glucose\ inj.)$$

$$Glycolytic\ reserve\ (\%) = Glycolytic\ capacity\ /\ Glycolysis\ *100$$

3.14. Co-immunoprecipitation of mitochondrial proteins

For co-immunoprecipitation (co-IP) experiments, NDUFA4 k/o THP-1 cells overexpressing NMES1-FLAG, NDUFA4-FLAG and MLS-mCherry-FLAG in a doxycycline-dependent manner were used. THP-1 cells were differentiated as described in chapter 3.2.4 and then plated on a 6-well plate, using 1×10^6 cells/well. Cells were harvested in 500 µL of mito co-IP lysis buffer supplemented with EDTA-free cOmplete protease inhibitor, pooling 2 wells per condition. Digitonin was added to the buffer on the day of use. Cells were scraped from the well surface, followed by homogenization, performing 6 sets of 5 strokes each with a 29G needle. Thereafter, lysates were incubated on ice for 15 minutes, followed by centrifugation at 4 °C at 20,000×g for 30 minutes. For the co-IP, anti-DYKDDDDK G1 Affinity Resin was washed once with mito co-IP lysis buffer. Per sample, 40 µL of bead slurry were used. The beads were pelleted by centrifugation at 4 °C at 700×g for 30 seconds. Cleared lysates were incubated with the beads at 4 °C overnight to allow antigen binding. Then, beads were washed 4× with mito co-IP wash buffer supplemented with 0.04 % digitonin. Thereafter, beads were washed 2× with mito co-IP wash buffer without detergent. After the first no-detergent wash, samples were transferred to clean 1.5 mL tubes to enhance detergent removal. Beads were pelleted, frozen on dry ice and stored at -80 °C until further processing (see chapter 3.15). For mass spectrometry measurements, 4 independent replicates were generated.

To validate potential interaction partners of NMES1 identified in the mass spectrometry experiment, a similar protocol was used, working with transiently transfected HEK293T cells. On the day prior to transfection, 7.5×10^5 cells were plated per well on a 6-well plate. Cells were transfected with a combination of two plasmids per well, as listed in Table 24. FLAG- and HA-tagged mScarlet was used to control for unspecific interactions.

Table 24. Combinations of plasmids used.

Plasmid 1	Plasmid 2
pEF-BOS_hsNMES1-FLAG	pEF-BOS_HA-mScarlet
pEF-BOS_hsNDUFA4-FLAG	pEF-BOS_HA-mScarlet
pEF-BOS_FLAG-mScarlet	pEF-BOS_MPC2-HA
pEF-BOS_hsNMES1-FLAG	pEF-BOS_MPC2-HA
pEF-BOS_hsNDUFA4-FLAG	pEF-BOS_MPC2-HA

Per well, 0.6 µg of each plasmid (plasmid 1 and plasmid 2) were diluted in 50 µL of OptiMEM. 3 µL of GeneJuice transfection reagent were added dropwise to 50 µL of OptiMEM, mixed thoroughly by vortexing and incubated on ice for 5 minutes. Thereafter, the transfection reagent mix was added to the plasmid DNA dilution, followed by incubation at room temperature for 20 minutes. Finally, the transfection mix was added dropwise to the well. 24 hours after transfection, cells were detached using trypsin, washed once with PBS and lysed in 500 µL of mito co-IP lysis buffer supplemented with EDTA-free cOmplete protease inhibitor. Digitonin was added to the buffer on the day of use. Cells were homogenized, performing 6 sets of 5 strokes each with a 26G needle. The remaining procedure was carried out as described above. After the final washing step, proteins bound to the beads were eluted using 50 µL of low pH elution buffer. Beads were incubated at room temperature for 10 minutes. Thereafter, eluates were neutralized by adding 7.5 µL of neutralization buffer per sample. Since low pH elution is not very efficient, beads were then boiled in 50 µL of 1× Laemmli buffer at 70 °C for 20 minutes. Resulting samples were then subjected to western blotting as described in chapter 3.12.

3.15. LC-MS/MS-based proteomics

Sample preparation, LC-MS/MS measurements and data processing using MaxQuant were kindly carried out by Dr. Antonio Piras (AG Pichlmair, Technical University of Munich). Beads were incubated in 1× guanidinium chloride buffer on a shaker at 45 °C and 1200 rpm for 5 minutes. Subsequently, an on-bead digest was carried out. To this end, 0.5 µg of LysC in 1× guanidinium chloride buffer were added, followed by incubation on a shaker at 37 °C and 800 rpm for 3 hours. Subsequently, 0.75 µg of trypsin in 0.1 M Tris buffer (pH 8) were added, followed by incubation on a shaker at 30 °C and 800 rpm for 16 hours. Thereafter, stage tip loading buffer was added to each sample to stop the enzymatic digest. Samples

were mixed by vortexing and centrifuged at 10,000 rpm using a benchtop centrifuge. The supernatant was transferred to a new 1.5 mL tube and samples were de-salted using C18 stage tips.

Purified peptides were measured on a Q Exactive HF mass spectrometer online-coupled to an EASY-nLC 1200 system (Thermo Fisher Scientific). The liquid chromatography setup consisted of a 75 µm x 50 cm analytical column, packed in-house with Reprosil-Pur C18-AQ 1.9 µm particles (Dr. Maisch GmbH). For peptide separation, a binary buffer system was used, consisting of buffer A (0.1 % (v/v) formic acid in water), and buffer B (80 % (v/v) acetonitrile, 0.1 % (v/v) formic acid in water). A 120-minute gradient was used, which was stepped as follows: 5-30 % buffer B (95 minutes), 30-95 % buffer B (10 minutes), wash out at 95 % buffer B (5 minutes), decrease to 5 % buffer B (10 minutes). The flow rate was set to 300 nL/minute and the temperature for peptide elution was set to 60 °C. All measurements were performed in positive ion mode, the spray voltage was set to 2.5 kV, funnel RF level at 60, and heated capillary at 250 °C. Data-dependent acquisition (DDA) included repeating cycles of one MS1 full scan (300–1,650 m/z, R = 60,000 at 200 m/z) at an ion target of 3×10^6 with an injection time of 20 ms. For MS2 scans, the top 15 intense isolated and fragmented peptide precursors (R = 15,000 at 200 m/z, ion target value of 1×10^5, and maximum injection time of 25 ms) were recorded. Isolation and fragmentation of the same peptide precursor was eliminated by dynamic exclusion for 20 seconds. The isolation window of the quadrupole was set to 1.4 m/z and HCD to a normalized collision energy of 27 %, respectively. All buffers were prepared using LC-MS grade reagents.

Raw MS data files obtained from LC-MS/MS analysis conducted in data-dependent acquisition mode were processed with MaxQuant (version 2.0.1.0) using the default settings, with "label-free quantification" (LFQ min ratio count 2, normalization type classic) enabled. Spectra were searched against forward and reverse sequences of the reviewed human proteome (UP000005640_9606 and UP000005640_9606_additional) using the built-in Andromeda search engine. The raw data were analyzed using the "match between runs" and "intensity Based Absolute Quantification" (iBAQ) options.

MaxQuant output files were analyzed using Perseus v 2.0.7.0. Protein groups were filtered, removing entries only identified by site, or marked as reverse sequence matches or contaminants. Furthermore, protein groups detected in less than three out of four replicates in at least one condition were excluded. LFQ values were $\log_2$-transformed and missing values were imputed by sampling values from a normal distribution calculated from the measured data (width = 0.3× SD, downshift = -1.8× SD). Statistical significance was evaluated using a two-sided Student's t-test, with the cut-off for permutation-based FDR set to 0.005 and the number of randomizations set to 250. S0 was set to 0.3.

To take the different expression levels of NMES1-FLAG and NDUFA4-FLAG into account, a scatter plot showing the $\log_2$ fold change enrichment of proteins for IP of NMES1-FLAG versus NDUFA4-FLAG as compared to the MLS-mCherry-FLAG control was generated: Significantly enriched proteins from the Student's t-test were filtered, setting the cut-off for the $\log_2$ fold change to 1.5. Furthermore, proteins were only considered specific NMES1 or NDUFA4 interactors if they showed a $\log_2$ fold change difference equal to or bigger than 1 between NMES1-FLAG and NDUFA4-FLAG affinity purifications. MitoCarta 3.0 was used to identify mitochondrial proteins and components and assembly factors of the different ETC complexes [189].

3.16. Transcriptome analysis using RNA sequencing

To investigate potential changes in the transcriptome upon induction of NMES1 expression, RNA sequencing (RNAseq) was carried out. To this end, THP-1 cells expressing NMES1 or mCherry in a doxycycline-dependent manner were differentiated as described in chapter 3.2.4. Thereafter, cells were plated on a 96-well plate, using 80,000 cells/well. 5 technical replicates were plated per condition. Cells were left to rest for 2 days, followed by doxycycline induction.

To analyze the effect of NMES1 expression alone, cells expressing NMES1 or mCherry in a doxycycline-dependent manner were treated with doxycycline for 4, 8, 16, or 24 hours. To analyze the effect of NMES1 expression on the response to R848 stimulation, approximately 20 hours after doxycycline induction, cells were treated with 2 µg/mL R848 for 4 hours or left untreated.

Samples were harvested in 100 µL of RLT Plus buffer supplemented with 1 % β-mercaptoethanol. Lysates were diluted 1:8 with RLT Plus buffer supplemented with 1 % β-mercaptoethanol in order to achieve an optimal cell number of 10,000 cells/100 µL. RLT lysates were randomized using a Biomek i7 Automated Workstation (Beckman Coulter) and stored at -80 °C.

RNA extraction and library preparation was kindly carried out by Ines Bliesener (AG Enard, Ludwig-Maximilians-Universität München). RNAseq libraries were prepared according to the prime-seq protocol published by Janjic *et al.* [190]. In brief, 50 µL of the diluted RLT lysates described above were utilized for library preparation. Samples were treated with proteinase K and DNase I, followed by reverse transcription using barcoded oligo-dT primers. Barcoded cDNAs were pooled, treated with Exonuclease I and amplified by PCR with 9 cycles. 60 ng of pooled cDNA were used for the generation of the final library, for which the cDNA was fragmented, end-repaired, dA-tailed and ligated to adapters. The resulting fragments were amplified with 9 cycles of PCR using Illumina adapters as primers in order to enrich for 3'-ends and introduce Illumina sample barcodes. The final library was quantified using a Bioanalyzer 2100 High Sensitivity DNA Kit (Agilent)

and sequenced on a NextSeq 1000/2000 P2 Flowcell, using 28 cycles for the forward read (Sample-Barcode & UMI), 8 cycles for each of both index reads and 93 cycles for the reverse read (cDNA).

Data pre-processing was kindly carried out by Dr. Daniel Richter (AG Enard, Ludwig-Maximilians-Universität München) as published by Janjic *et al.* [190]. Data analysis was kindly conducted by Dr. Niklas Schmacke (AG Hornung, Ludwig-Maximilians-Universität München). In brief, the counts table was analyzed using R [181]. Based on principle component analysis, one outlier was excluded (well H04, barcode CCACTCTAGGCT; corresponding to unstimulated NMES1-expressing cells that were not treated with doxycycline). Furthermore, only transcripts with at least 10 reads in at least 3 samples were included in the analysis. Finally, differentially expressed genes were identified using the DESeq2 package.

3.17. Quantitative PCR (qPCR)

To validate results obtained from the RNAseq experiment, quantitative PCR (qPCR) was performed. Primers were designed using the RealTime qPCR Assay design tool from IDT [191]. Primers were designed to target the CDS of the respective gene, with the amplicon spanning an exon-exon junction. Wherever possible, primer pairs detecting all reported isoforms were selected. The qPCR reaction was run in duplicates for each sample. GAPDH expression was measured for normalization. Primer sequences are listed in Table 3.

1×10^6 differentiated THP-1 cells expressing NMES1 or mCherry in a doxycycline-dependent manner were plated per well on a 6-well plate. Two days after plating, cells were treated with 1 µg/mL doxycycline to induce transgene expression. Approximately 20 hours after doxycycline induction, cells were treated with 2 µg/mL R848 for 4 hours or left untreated. Cells were harvested in RLT Plus buffer supplemented with 40 mM DTT, using 300 µL of buffer per well. Plates were sealed and frozen at -80 °C overnight. RNA extraction and cDNA synthesis were carried out as described in chapters 3.3.1 and 3.3.2, respectively. Equal amounts of RNA were used in the cDNA synthesis reaction for each sample. qPCR was carried out using SYBR green. The reaction was set up as described in Table 25.

Table 25. qPCR reaction.

Reagent	Volume
cDNA	4 µL
Forward primer (5 µM)	0.5 µL
Reverse primer (5 µM)	0.5 µL
Takyon No ROX SYBR 2× MasterMix blue dTTP	5 µL

qPCR was performed using a CFX96 Touch Real-Time PCR detection system (Bio-Rad), using the settings described in Table 26.

Table 26. qPCR settings.

Step	Temperature	Duration	Cycles
Carry over prevention	50 °C	2 min	1×
Taykon™ activation	95 °C	3 min	1×
Denaturation	95 °C	10 sec	40×
Annealing/Extension	60 °C	1 min	

To ensure primer specificity, a melt curve was included at the end of the qPCR run when using a primer pair for the first time.

For the validation of the RNAseq results, the data were analyzed using the $\Delta\Delta C_t$ method: For each gene and sample, the mean C_t was calculated, followed by normalization against the mean C_t value obtained for GAPDH (ΔC_t). Then, the difference between sample and control ΔC_t values was calculated (e.g. NMES1 +dox vs. mCherry +dox), yielding the $\Delta\Delta C_t$ value. Finally, fold change expression was calculated as follows:

$$fold\ change\ expression = 2^{-\Delta\Delta Ct}$$

For the analysis of TNF expression levels, relative expression was calculated as follows:

$$relative\ expression = 2^{-\Delta Ct}$$

3.18. MitoSOX Flow Cytometry

MitoSOX flow cytometry was performed to measure mitochondrial ROS production. THP-1 cells expressing NMES1 or mCherry in a doxycycline-dependent manner and NDUFA4 k/o THP-1 cells were differentiated, treated with doxycycline and stimulated as indicated. $0.5\text{-}1\times10^6$ cells were used for staining. To this end, cells were detached using 2mM EDTA/DPBS and a cell suspension of 1×10^6 cells/mL in DPBS was generated. Cells were stained with Zombie Aqua™, using a 1:500 dilution. Samples were incubated at room temperature for 30 minutes, washed once with DPBS and taken up in FACS buffer. Thereafter, a 0.5 mM MitoSOX reagent solution was generated by dissolving lyophilized MitoSOX reagent in DMSO. MitoSOX staining was performed using 2 µL of MitoSOX reagent solution per mL of cell suspension. Samples were incubated on a shaker at 37 °C for 20 minutes, protected from light. Subsequently, cells were washed 3× with pre-warmed FACS buffer and resuspended in 500 µL of FACS buffer per 1×10^6 cells. The cell suspensions were then transferred to strainer-capped FACS tubes. As a positive control, one sample of untreated cells was treated with 5 µM antimycin A for 20 minutes prior to analysis. Samples were analyzed using a LSRFortessa (BD Biosciences).

Data were evaluated using FlowJo™ 10. First, FSC vs. SSC gating was used to select intact cells. Then, SSC-A vs. SSC-H gating was used to filter for single cells.

Live cells were selected based on an SSC-H vs. V525_50-A plot. Finally, MitoSOX positive cells were identified based on an SSC-H vs. YG582_15-A plot.

3.19. Statistical analysis

Statistical analyses were carried out using GraphPad Prism 10.0.3. When the response was affected by two factors (e.g., cell line and stimulus), a two-way ANOVA was carried out. When the response was affected by a single factor (e.g., cell line), a one-way ANOVA was performed. When comparing every column mean with every column mean, a Tukey's multiple comparisons test was performed. When comparing a control column (e.g., wt) mean with the other column means, a Dunnett's multiple comparisons test was performed.

4. RESULTS

4.1. Establishing a cell culture model to investigate the role of NMES1

4.1.1. NMES1 expression in MDMs is regulated by NF-κB

In primary human monocytes, NMES1 protein levels strongly increase upon LPS stimulation [106]. However, monocytes are short-lived cells and can only be cultivated *in vitro* for 1-2 days. To allow for the analysis of the effect of the loss of NMES1 induced by genome editing, monocyte-derived macrophages (MDMs) were chosen as a model. Here, human monocytes are subjected to genome editing and subsequently differentiated to MDMs for 5-7 days. We reasoned that in doing so, we would be able to ensure that cellular perturbations induced by genome editing do not affect the functionality of the cells. To confirm that NMES1 protein levels indeed increase in MDMs upon LPS stimulation, wildtype and NMES1-deficient MDMs were stimulated with LPS and NMES1 protein levels were analyzed by western blotting (Figure 7A). Furthermore, cells deficient for NDUFA4 and TBX21 were included. TBX21 encodes the T_H1-specific transcription factor T-bet, which is not expressed in myeloid cells [115, 192]. Therefore, TBX21-deficient cells serve as a control to determine effects induced by genome editing alone. The efficiency of RNP-mediated knock-out of NMES1, NDUFA4 and TBX21 was 90-100 %, as determined using the ICE CRISPR analysis tool. In line with this, no bands could be observed for NMES1 and NDUFA4 in the respective lanes, showing that the commercially available antibodies against NMES1 and NDUFA4 are specific (Figure 7A). Interestingly, LPS stimulation of wildtype and TBX21-deficient cells resulted in a strong decrease of NDUFA4 protein levels. This effect was dependent on NMES1, since in NMES1-deficient cells, NDUFA4 levels remained stable upon LPS stimulation. Of note, lysates derived from unstimulated MDMs also yielded faint bands for NMES1. The extent varied between donors (Figure 7B). M-CSF is known to activate NF-κB [193]. As NMES1 expression was not detected in unstimulated monocytes (Figure 7B, "undifferentiated"), we concluded that the expression in unstimulated MDMs is induced by M-CSF treatment. To keep NMES1 expression in unstimulated MDMs as low as possible, M-CSF was titrated (Figure 7C). 10 ng/mL M-CSF added every third day resulted in the biggest difference in NMES1 levels between unstimulated and LPS-stimulated cells. This differentiation protocol was therefore used for subsequent experiments, unless otherwise indicated.
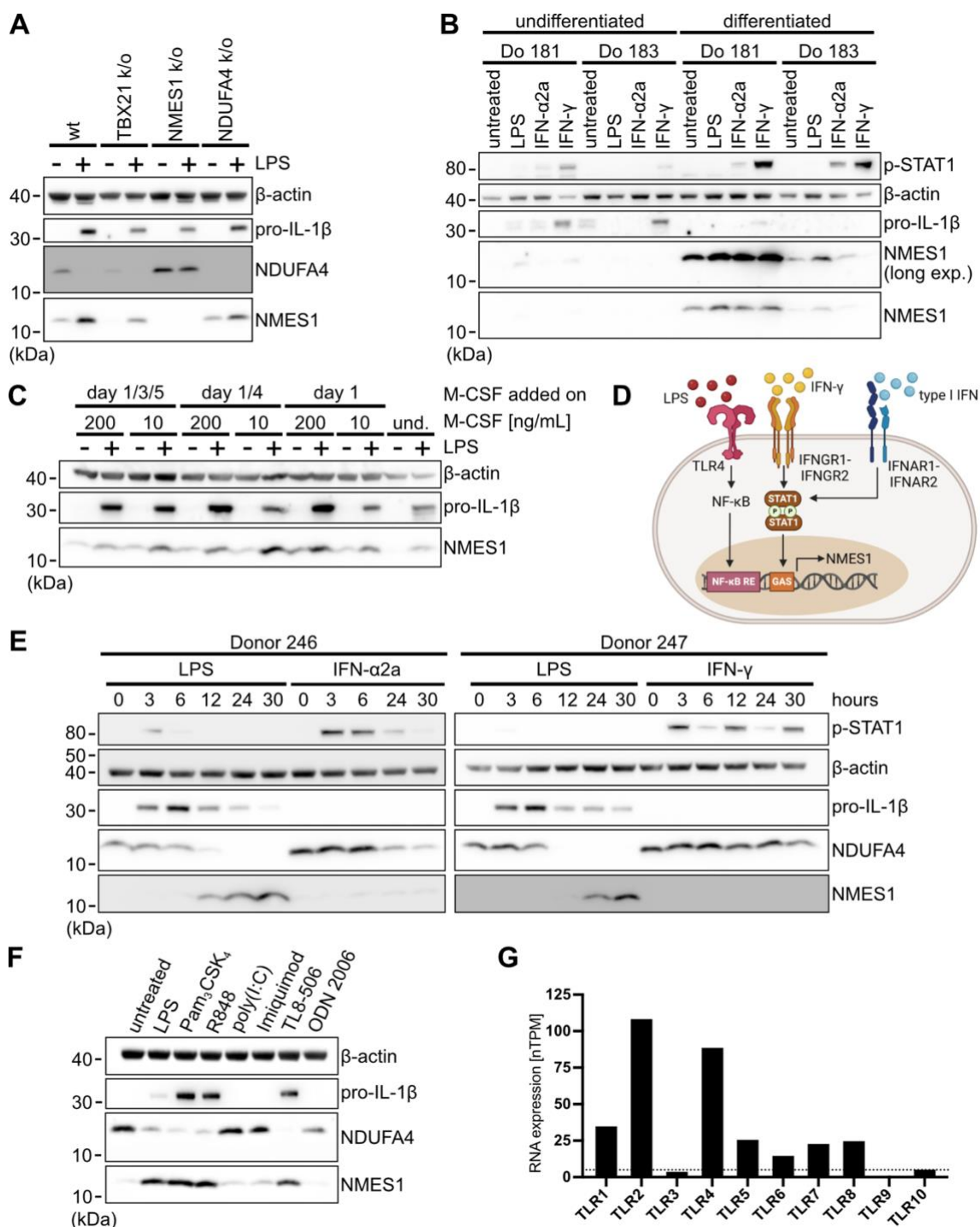
Figure 7. NMES1 expression in MDMs is regulated by NF-κB. (A) Monocytes were isolated from PBMCs using the Pan Monocyte Isolation kit and nucleofected with RNPs targeting the indicated gene. Cells were differentiated to MDMs for 5 days. Thereafter, cells were stimulated with LPS for 14 hours. Cells were harvested in 1× Laemmli sample buffer. n = 3. **(B)** Monocytes were isolated from PBMCs using CD14 MicroBeads and differentiated for 6 days using 200 ng/mL M-CSF. MDMs were stimulated using LPS, IFN-α2a or IFN-γ for 14 hours. n = 3. **(C)** Monocytes were isolated from PBMCs using CD14 MicroBeads and differentiated for 6 days using the amount of M-CSF indicated. New M-CSF was added on the days indicated. Cells were stimulated with LPS for 14 hours. und. = undifferentiated. n = 2 biological replicates. **(D)** Schematic representation of predicted transcription factor binding sites for the NMES1 gene locus, potentially driving NMES1 expression. Created with BioRender.com. **(E)&(F)** Monocytes were isolated from PBMCs using CD14 MicroBeads and differentiated for 5 days. **(E)** MDMs were stimulated with LPS, IFN-α2a or IFN-γ for the number of hours indicated. n = 2 biological replicates. **(F)** MDMs were stimulated using LPS,

Pam$_3$CSK$_4$, R848, poly(I:C) (HMW), TL8-506 or ODN 2006 for 24 hours. n = 4 biological replicates. **(G)** RNA expression levels of different TLRs in primary human monocytes. The horizontal dotted line indicates nTPM = 5. Data taken from the Human Protein Atlas [115, 116]. **(B)**, **(C)**, **(E)**&**(F)** Cells were harvested in RIPA lysis buffer supplemented with protease inhibitor. SDS-PAGE was carried out using 12 % bis-tris gels. Equal amounts of protein were loaded in each lane.

The promoter region of C15orf48 was reported to contain three potential NF-κB consensus binding sites and a GAS element [108], indicating that NMES1 expression could be regulated by TLR and type I & II IFN signaling (Figure 7D). Sorouri *et al.* showed that in A549 cells, NMES1 expression can be induced by IFN-γ treatment [110]. To determine whether this is also the case in MDMs, a stimulation time-course experiment was carried out (Figure 7E). Since STAT1 dimerization can be induced by both IFN-γ and type I IFN [194], stimulation with IFN-α2a was also included. While very faint bands corresponding to NMES1 were detected for stimulation with IFN-α2a, with a slight increase in signal intensity starting at the 6-hour timepoint, stimulation with IFN-γ did not yield any bands for NMES1. Thus, in MDMs, NMES1 expression is primarily driven by NF-κB. Stimulation with LPS showed that induction of NMES1 expression is a late event: While pro-IL-1β could be detected after 3 hours and peaked at 6 hours after stimulation, NMES1 could only be detected starting at 6 hours after stimulation. This is in line with published RNAseq data shown in Figure 2. Furthermore, NMES1 protein levels continued to increase until the latest timepoint included (30 hours). As already described for Figure 7A, a decrease of NDUFA4 protein levels could be observed with the increase in NMES1 protein levels.

To show that NMES1 expression can also be induced by TLR ligands other than LPS, MDMs were stimulated with different TLR ligands and NMES1 protein levels were analyzed by western blotting (Figure 7F). Stimulation with LPS (TLR4), Pam$_3$CSK$_4$ (TLR1/2), R848 (TLR7&TLR8) and TL8-506 (TLR8) resulted in strong bands for NMES1, with a concomitant decrease in NDUFA4 protein levels. In contrast, stimulation with poly(I:C) (TLR3), or ODN 2006 (TLR9) did not result in any apparent increase of NMES1 protein levels. At the same time, no signal for pro-IL-1β was detected upon stimulation with poly(I:C) or ODN 2006, indicating that NF-κB is not activated under these conditions. This is in line with RNA expression data from the Human Protein Atlas, which show that in human macrophages, TLR3 is among the least abundant TLRs and TLR9 expression is not detected (Figure 7G) [115, 116]. Stimulation with Imiquimod (TLR7) did not yield any bands for IL-1β and only showed a slight increase in signal intensity for NMES1 compared to the unstimulated control, suggesting that the response to R848 stimulation is mainly mediated by TLR8 in MDMs (Figure 7F).

4.1.2. There is no suitable myeloid cell line that endogenously expresses NMES1

To identify a cell line that can be used to study the role of NMES1, BLaER2, THP-1, KBM-7, U-937, HL-60 and HMC-1.1 cells were tested for NMES1 expression by western blotting. mRNA expression data available from the Human Protein Atlas suggest that HAP1, HL-60, U-937 and THP-1 do not express NMES1 (Figure 8A) [115, 195]. HAP1 is a haploid cell line derived from KBM-7. In addition, mRNA expression data generated in-house for BLaER1 cells showed that BLaER1 cells do not express NMES1 (data not shown). However, since NMES1 expression is stimulation-dependent in MDMs, these cell lines were tested nonetheless. In brief, cell lines were treated with TLR ligands (LPS or Pam$_3$CSK$_4$), IFN-α2a or IFN-γ. Additionally, where indicated, cells were primed with IFN-γ prior to stimulation with TLR ligands. BLaER2, THP-1, KBM-7 and U-937 and HL-60 did not yield any bands for NMES1 in any of the conditions tested (Figure 8B-F). HMC-1.1, a mast cell derived cell line, showed constitutive expression of NMES1 (Figure 8G), as indicated by RNA sequencing data (Figure 8A). NMES1 protein levels in HMC-1.1 cells were slightly increased upon treatment with IFN-α2a. All cell lines except KBM-7 and HMC-1.1 yielded bands for pro-IL-1β, showing that NF-κB activation was successful (Figure 8B, C, E & F). Despite the expression of NMES1, HMC1.1 was deemed unsuitable as a model, as we could not detect any release of IL-6 or TNF upon stimulation with Pam$_3$CSK$_4$ (TLR1/2), poly(I:C) (TLR3), LPS (TLR4), R848 (TLR7&TLR8) and PMA (PKC) (data not shown). In conclusion, none of the cell line models commonly used to study monocytes and macrophages *in vitro* endogenously express NMES1.
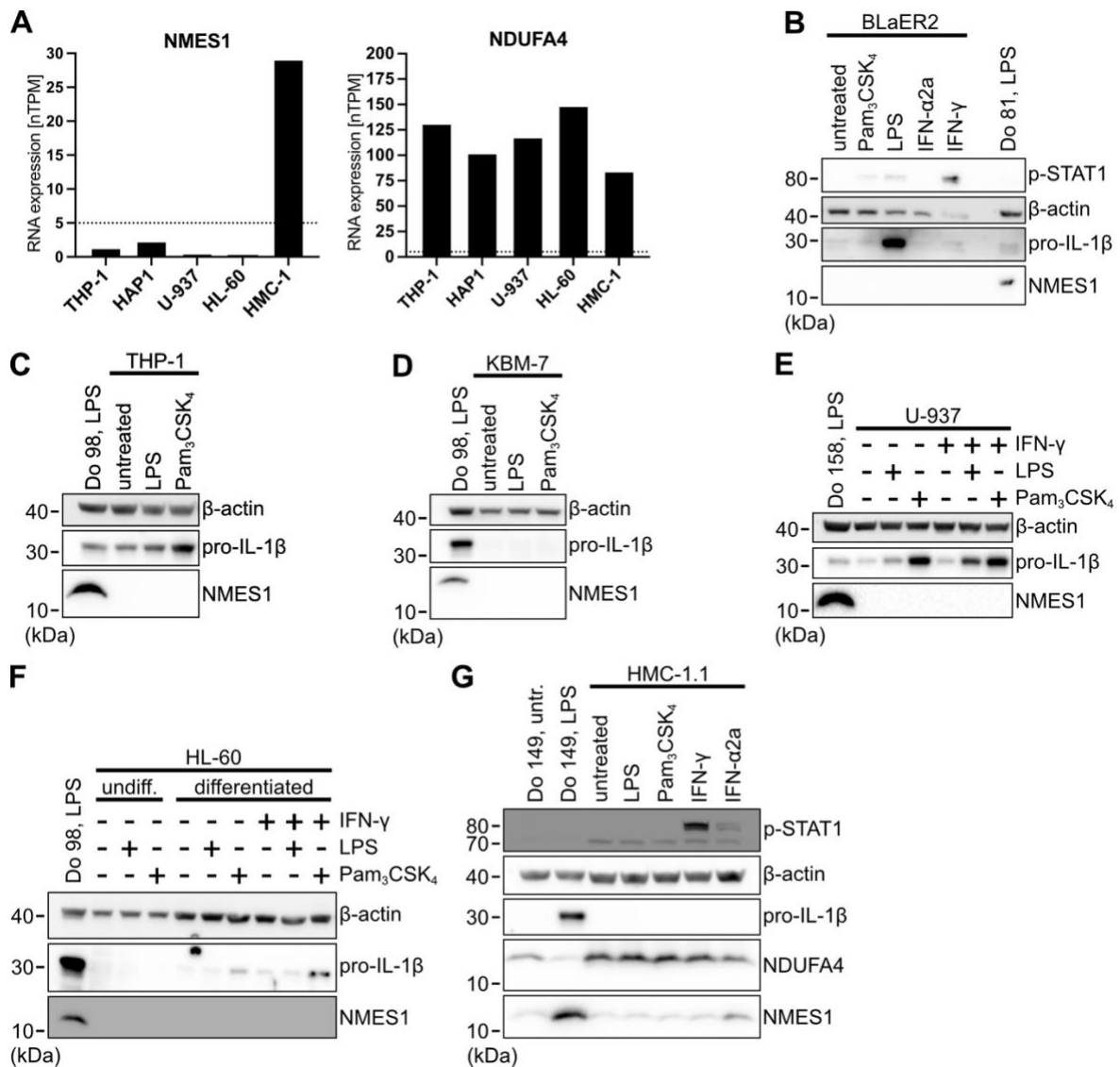
Figure 8. Most myeloid cell lines do not endogenously express NMES1. (A) RNA expression levels of NMES1 and NDUFA4 in myeloid cell lines. The horizontal dotted line indicates nTPM = 5. Data taken from the Human Protein Atlas [115, 195]. **(B)** Transdifferentiated BLaER2 cells were stimulated with LPS, Pam₃CSK₄, IFN-α2a or IFN-γ for 14 hours. n = 2. **(C)** THP-1 cells were differentiated to macrophages and subjected to starvation using culture medium containing 0.3 % FCS for 7 hours. Thereafter, cells were primed using 100 ng/mL IFN-γ for 2 hours. Finally, cells were stimulated with LPS or Pam₃CSK₄ for 14 hours. n = 2. **(D)** KBM-7 cells were stimulated with LPS or Pam₃CSK₄ for 14 hours. n = 1. **(E)** U-937 cells were differentiated and, where indicated, primed with IFN-γ for 2 hours. Cells were stimulated with LPS or Pam₃CSK₄ for 14 hours. n = 1. **(F)** HL-60 cells were differentiated, followed by starvation for approximately 8 hours using culture medium containing 0.3 % FCS. Where indicated, cells were primed with IFN-γ for 2 hours. Thereafter, cells were stimulated with LPS or Pam₃CSK₄ for 14 hours. **(G)** HMC-1.1 cells were treated with LPS, Pam₃CSK₄, IFN-γ or IFN-α2a for 14 hours. n = 2. **(B)-(G)** Cells were harvested in RIPA lysis buffer supplemented with protease inhibitor. SDS-PAGE was carried out using 12 % bis-tris gels. Equal amounts of protein were loaded in each lane. Lysates generated from MDMs were loaded as a reference: Monocytes were isolated from PBMCs using CD14 MicroBeads, differentiated for 5 days and stimulated with LPS for 14 hours.

4.1.3. CRISPR activation only induces low levels of NMES1 expression

As we could not identify a suitable cell line that endogenously expresses NMES1, overexpressing NMES1 or activating NMES1 expression using CRISPR activation (CRISPRa) represent possible alternatives. Overexpression mainly differs from physiological NMES1 expression in two modalities: Firstly, the constructs used do not include the 5'- and 3'-UTRs, and therefore do not encode miR-147b. Secondly, NMES1 overexpression occurs separately from stimulation with TLR ligands and downstream activation of NF-κB. In contrast, if successful, CRISPRa would induce expression of both NMES1 and miR-147b, and could make the promoter region of C15orf48 accessible to activation by NF-κB. Therefore, CRISPRa may more closely mimic endogenous expression of NMES1.

In attempt to induce NMES1 expression from its endogenous locus, we generated THP-1 and BLaER2 cells expressing a hybrid VP64-p65-Rta (VPR) tripartite activator fused to endonuclease-dead Cas9 (dCas9) [196]. These cell lines were then transduced with constructs encoding a gRNA targeting the proximal promoter region of the C15orf48 gene locus (Figure 9A). Two different gRNAs were tested. The remaining three gRNAs suggested by CRISPick were predicted to have low on-target activity (Figure 9B).

Figure 9. CRISPR activation only induces low levels of NMES1 expression. (A) Schematic representation of the C15orf48 promoter region as annotated by the ENCODE project [197-199]. NF-κB family member binding sites were predicted using JASPAR [200]. Created using SnapGene. TSS = transcription start site. **(B)** gRNAs for CRISPRa designed using CRISPick [201, 202]. Only gRNA1 & gRNA2 were predicted to have high on-target activity. **(C)-(E)** THP-1 or BLaER2 cells expressing dCas9-VPR in a doxycycline-dependent manner and constitutively expressing a gRNA (g1, g2) targeting the proximal promoter region of C15orf48 were differentiated and subsequently treated with doxycycline (dox) for the number of hours indicated. **(E)** After doxycycline induction for the duration indicated, cells were treated with Pam3CSK4 for 15 hours. Cells were harvested in RIPA lysis buffer supplemented with protease inhibitor. Lysate derived from LPS stimulated MDMs was loaded as a reference (Do 252 LPS). SDS-PAGE was carried out using 4-12 % bis-tris gels. Equal amounts of protein were loaded per lane. n = 1.

We could induce NMES1 expression in THP-1 cells expressing gRNA1 (g1), however, NMES1 expression levels were much lower compared to LPS-stimulated MDMs (Figure 9C). Furthermore, we could not achieve any detectable levels of NMES1 expression in BLaER2 cells (Figure 9C). miR-147b is generated from NMES1 mRNA, and it is possible that the mRNA is processed by the miRNA machinery, thereby limiting the amount of NMES1 protein generated. Since NDUFA4 is targeted by miR-147b, in case of an increase in miR-147b, we would expect to see a decrease in NDUFA4 protein levels [109]. However, NDUFA4 protein levels remained stable upon induction of dCas9-VPR expression (Figure 9C). This suggests that mRNA expression levels induced through CRISPR activation in THP-1 cells are low.

In attempt to increase NMES1 expression in THP-1 cells expressing gRNA1, we analyzed NMES1 expression at different timepoints after doxycycline induction. NMES1 expression was still extremely low even 72 hours after doxycycline induction (Figure 9D). As mentioned above, it is conceivable that after initial dCas9-VPR-guided activation of transcription from the C15orf48 gene locus, the locus becomes accessible to NF-κB. Therefore, we analyzed whether the combination of doxycycline-induced expression of dCas9-VPR and TLR-mediated NF-κB activation results in higher NMES1 protein levels. Indeed, stimulation with Pam$_3$CSK$_4$ after initial treatment with doxycycline led to an increase in NMES1 expression levels (Figure 9E). In addition, a slight decrease of NDUFA4 protein levels could be observed. However, the NMES1 expression levels achieved were still much lower compared to LPS-stimulated MDMs. Overall, despite the fact that NMES1 expression could successfully be induced in THP-1 cells using CRISPRa, the expression levels achieved were not sufficient to mimic endogenous NMES1 expression. Therefore, to study the role of NMES1, a THP-1 based overexpression model was used for the majority of the subsequent experiments.

4.2. Elucidating the role of NMES1 in the electron transport chain

4.2.1. NMES1 integrates into complex IV of the electron transport chain

Since NDUFA4 is a structural homolog of NMES1, we expected NMES1 to be a component of CIV of the ETC. To test whether this is the case, we carried out blue native PAGE (BN PAGE) and 2D PAGE on mitochondria isolated from LPS-stimulated MDMs (Figure 10A & B). As expected, NMES1 co-migrated with NDUFA4 and MTCO1, one of the core components of CIV. This is in line with recently published data by Lee $et\ al.$ and Clayton $et\ al.$ [109, 111]. In addition to the band corresponding to monomeric CIV (IV$_1$), bands at a higher molecular weight were detected. These bands likely correspond to dimeric CIV (IV$_2$), the complex III$_2$+IV$_1$ and CIV-containing supercomplexes (I+III$_2$+IV$_n$) [150]. BN and 2D PAGE yielded slightly different band patterns: Interestingly, 2D PAGE yielded a strong signal for NMES1 corresponding to a molecular weight below 66 kDa in the first dimension. In BN PAGE, this band could also be detected, although the band was less intense and more diffuse compared to the band corresponding to IV$_1$. Furthermore, two bands of similar intensity could be detected for MTCO1 in BN PAGE, whereas in 2D PAGE the strongest signal was detected at the molecular weight of IV$_1$. Irrespective of these differences, of all CIV-containing complexes, the strongest signal for NMES1 was detected at the molecular weight of IV$_1$.

Next, we sought to determine whether NMES1 also integrates into CIV when overexpressed in cell lines, and whether adding a C-terminal FLAG-tag interferes with the integration. To this end, we generated HEK293T and THP-1 cells expressing NMES1 or NMES1-FLAG in a doxycycline-dependent manner. mCherry was used as a control. As observed for MDMs, NMES1 co-migrated with NDUFA4 and MTCO1 (Figure 10C-E). Furthermore, in HEK293T, a strong signal for NMES1 corresponding to a molecular weight below 66 kDa in the first dimension can be observed (Figure 10C). HEK293T cells expressing mCherry did not yield a band at this height, confirming that this band is specific. A band for NDUFA4 could also be detected at the same molecular weight, however the signal was much weaker compared to the band corresponding to IV$_1$. Of note, the anti-NDUFA4 antibody yields a strong off-target band at the height of IV$_2$ in BN PAGE (Figure 10D & E). This band is still present in BN PAGE performed using a THP-1 NDUFA4$^{-/-}$ single cell clone (Figure 10E). 2D PAGE experiments yielded the strongest signal for NDUFA4 at the molecular weight of IV$_1$ (Figure 10A & C). This is in line with data published by Clayton $et\ al.$, who found that, like NMES1, NDUFA4 predominantly migrates at the molecular weight of IV$_1$ [111]. Interestingly, total levels of NMES1-FLAG were consistently lower than those of untagged NMES1 (Figure 10F). This difference in expression was also reflected in the amount of protein integrated into CIV as determined by BN PAGE (Figure 10E).
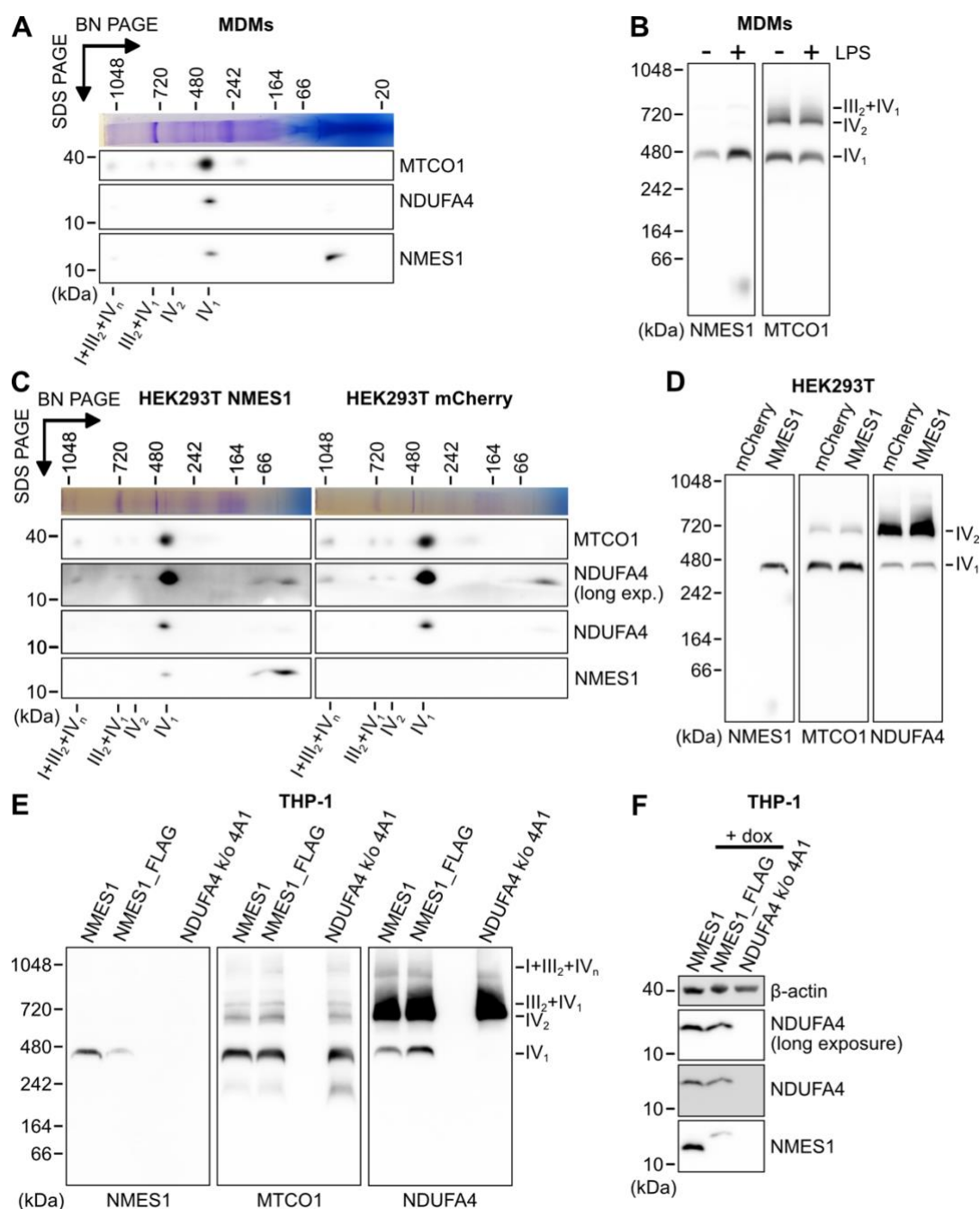
Figure 10. NMES1 integrates into CIV of the ETC. (A) & **(B)** Monocytes were isolated from PBMCs using CD14 MicroBeads and differentiated for 5 days. Thereafter, cells were stimulated with LPS for 14 hours. **(C)**&**(D)** HEK293T cells expressing NMES1 in a doxycycline-dependent manner were treated with doxycycline for 24 hours. **(A)** & **(C)** Mitochondria were isolated, followed by BN PAGE. The samples were loaded in duplicate. One lane was used for the 2nd dimension PAGE, while the other was subjected to Coomassie staining. **(B)**, **(D)** & **(E)** Mitochondria were isolated, followed by BN PAGE. Equal amounts of mitochondrial protein were loaded per lane. **(E)** THP-1 cells expressing NMES1 or NMES1-FLAG in a doxycycline-dependent manner were differentiated and subsequently treated with doxycycline (dox) for 24 hours to induce transgene expression. An NDUFA4-deficient THP-1 single cell clone was included to show that the band at approx. 720 kDa detected in the anti-NDUFA4 staining is unspecific. **(F)** For the experiment described in **(E)**, 1×10^6 cells were put aside before mitochondria isolation and whole cell lysates were generated using RIPA lysis buffer. SDS-PAGE was carried out using a 12 % bis-tris gel. Equal amounts of protein were loaded per lane. **(A)**-**(E)** Expected band size of monomeric (IV_1) and dimeric (IV_2) complex IV and complex IV-containing supercomplexes [150] are indicated at the bottom. $I+III_2+IV_1$, $I+III_2+IV_2$ and $I+III_2+IV_3$ are not resolved and are instead collectively labelled as $I+III_2+IV_n$.

4.2.2. The decrease in NDUFA4 protein levels is independent of miR-147b

The 3'-UTR of the C15orf48 gene transcript gives rise to miR-147b [108], and the microRNA target site prediction tool TargetScan lists NDUFA4 as the top target for miR-147b [132] (Figure 4). Therefore, it is conceivable that the miR-147b plays a role in the decrease of NDUFA4 protein levels upon induction of NMES1 expression (Figure 7A & G). To test whether NDUFA4 protein levels also decrease in the absence of miR-147b, we conducted experiments using HEK293T and THP-1 cells expressing mCherry or NMES1 in a doxycycline-dependent manner. Upon addition of doxycycline, NDUFA4 protein levels continuously decreased over time in cells expressing NMES1, but not in control cells expressing mCherry (Figure 11A & B). As the construct used to transduce HEK293T and THP-1 cells only contains the coding sequence of NMES1, but not the 3'-UTR, these results indicate that miR-147b is dispensable with regard to the decrease of NDUFA4 protein levels. This is in line with the findings of Lee *et al.*, which suggest that NMES1 is more efficient at reducing NDUFA4 protein levels than miR-147b [109].
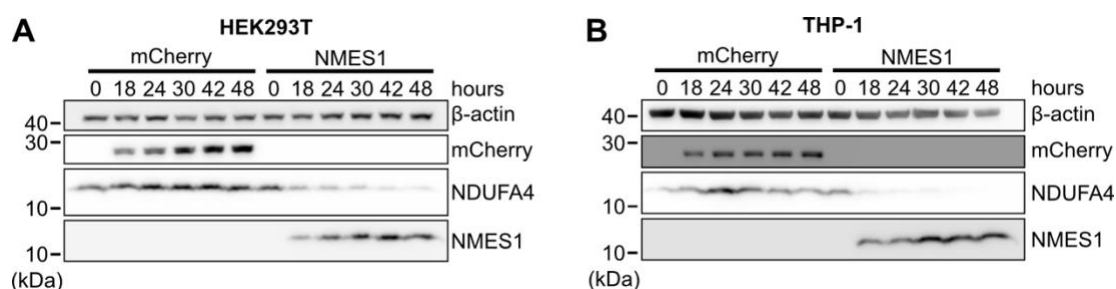
Figure 11. The decrease in NDUFA4 protein levels upon induction of NMES1 expression is independent of miR-147b. (A) HEK293T cells expressing mCherry or NMES1 in a doxycycline-dependent manner were treated with doxycycline for the number of hours indicated. n = 3. **(B)** THP-1 cells expressing mCherry or NMES1 in a doxycycline-dependent manner were differentiated and treated with doxycycline for the number of hours indicated. n = 1. **(A)** & **(B)** Cells were harvested in RIPA lysis buffer supplemented with protease inhibitor. SDS-PAGE was carried out using 12 % bis-tris gels. Equal amounts of protein were loaded in each lane.

4.2.3. Genome editing in MDMs affects electron transport chain activity regardless of the gene targeted

Having established that NMES1 is a component of CIV of the electron transport chain, we next aimed to analyze the effect of NMES1 on electron transport chain activity. To this end, we measured both mitochondrial respiration and CIV activity in MDMs. First, the optimal concentration of FCCP for MDMs was determined, with 1 µM FCCP resulting in the maximal oxygen consumption rate (OCR) (Figure 12A). Of note, mouse bone marrow derived macrophages (BMDMs) have been reported to exhibit a decreased oxygen consumption rate upon stimulation with LPS [203]. In contrast, data published by Clayton *et al.* suggests that this is not the case for MDMs [111]: They observed an increased basal respiration in MDMs upon LPS stimulation, whereas the maximal respiratory capacity remained unchanged. In our hands, LPS-stimulated MDMs did not exhibit an increased basal respiration and the maximal respiratory capacity remained largely unchanged (Figure 12B). When performing experiments with BMDMs we could not observe a decrease in maximal respiratory capacity upon LPS stimulation (Figure 12B). Rather, LPS-stimulated BMDMs exhibited an increased basal respiration compared to unstimulated cells (Figure 12B). These differences are most likely explained by differences in culture media composition and differentiation protocols. As we did not observe any LPS stimulation-dependent differences in the respiratory activity of MDMs, only the data obtained for the unstimulated condition is shown for the subsequent datasets.

Next, we performed mitochondrial stress tests on NMES1-deficient MDMs. NDUFA4-deficient MDMs were included to determine whether the effect observed is specific to NMES1. Furthermore, TBX21-deficient MDMs were used to identify effects induced by genome editing alone. The results varied between donors (Figure 12C), which might be explained in part by differences in knock-out efficiency. The knock-out efficiencies ranged from 88 % to 100 %, as determined using the ICE CRISPR analysis tool. In addition, successful genome editing was confirmed by western blotting (Figure 12D). Importantly, TBX21-deficient MDMs showed a lower maximal respiration and thus a decreased spare respiratory capacity when compared to wildtype cells. This indicates that the respiratory activity of these cells was somehow compromised by genome editing.

Measurements of CIV activity yielded similar results as the mitochondrial stress test: Results varied between donors, and CIV activity also seemed to be affected by genome editing itself, since the results obtained for TBX21-deficient and wildtype (wt) MDMs were not consistent (Figure 12E). The knock-out efficiency was 80-100 %, which was also confirmed by western blotting (Figure 12F). In conclusion, data generated using MDMs subjected to genome editing are not reliable enough to draw any conclusions with regard to the function of NMES1.
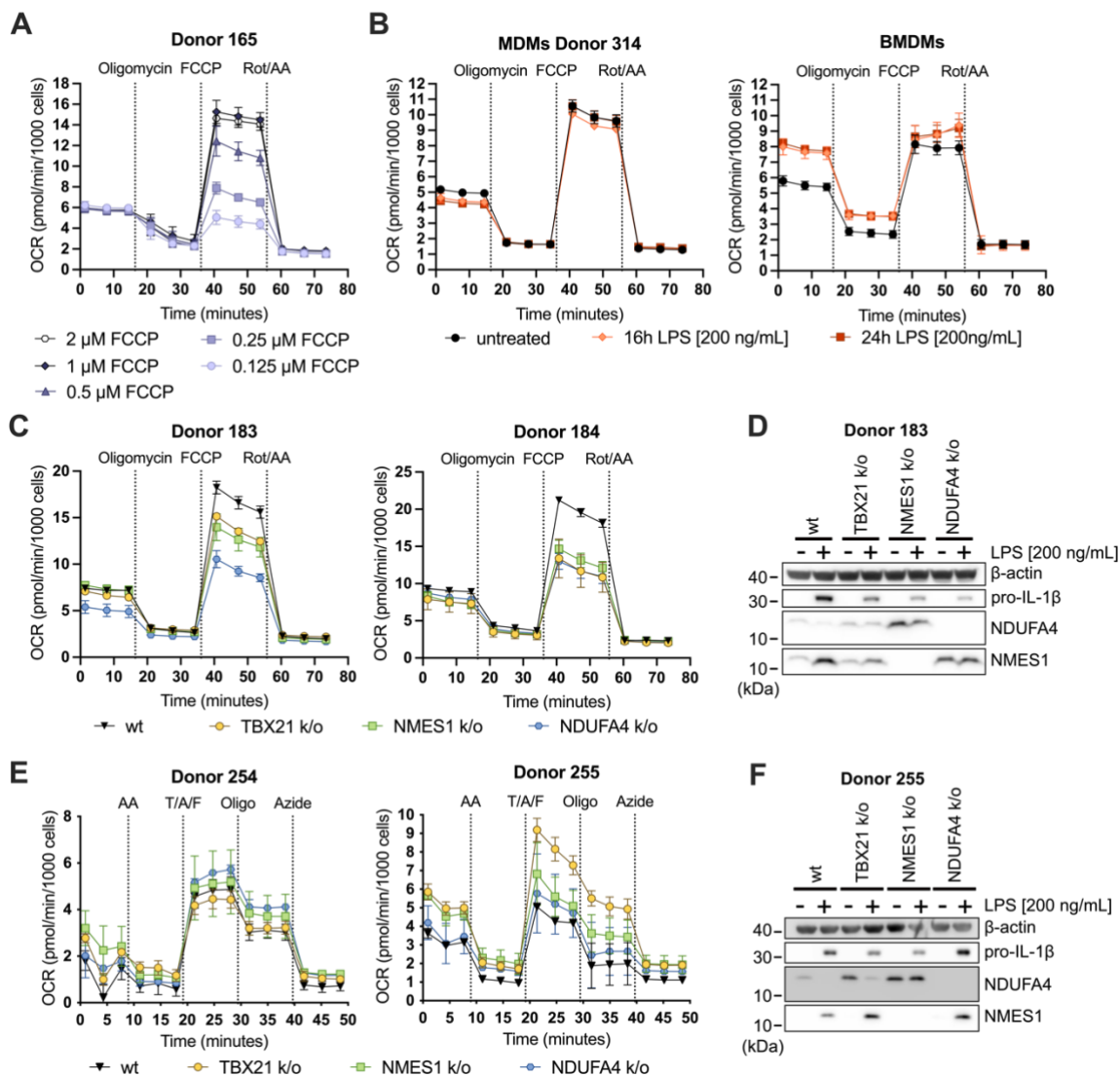
Figure 12. Genome editing in MDMs affects electron transport chain activity regardless of the gene targeted. (A) Monocytes were isolated using CD14 MicroBeads and subsequently differentiated for 7 days. A mitochondrial stress test was carried out using different concentrations of FCCP to determine which concentration induces the highest oxygen consumption rate (OCR). Rot/AA = rotenone/antimycin A. n = 1. **(B)** Monocytes were isolated using CD14 MicroBeads and subsequently differentiated for 5 days. Bone marrow-derived cells were isolated and differentiated to BMDMs for 6 days. Cells were stimulated with LPS for 16 or 24 hours or left untreated. Finally, a mitochondrial stress test was carried out. Error bars indicate the SD. Rot/AA = rotenone/antimycin A. MDMs: n = 4 biological replicates. BMDMs: n = 2 biological replicates. **(C)-(F)** Monocytes were isolated using the Pan Monocyte Isolation kit. Subsequently, RNP-mediated genome editing was carried out, targeting the indicated gene. Unedited (wt) cells were included as a control. Cells were differentiated for 5 days. n = 2 biological replicates. **(C)** A mitochondrial stress test was carried out. Error bars indicate the SD. AA = antimycin A. **(D)&(F)** Cells used in **(C)&(E)**, respectively, were stimulated with LPS for 14 hours or left untreated and subsequently subjected to SDS-PAGE to show that the genome editing was efficient. Cells were harvested in RIPA lysis buffer supplemented with protease inhibitor. SDS-PAGE was carried out using 12 % bis-tris gels. Equal amounts of protein were loaded in each lane. **(E)** Complex IV activity was measured. Error bars indicate the SD. AA = antimycin A; T/A/F = TMPD, ascorbate & FCCP; Oligo = oligomycin A; Azide = potassium azide. n = 2 biological replicates.

4.2.4. NMES1 and NDUFA4 are redundant regarding complex IV activity

As we were unable to analyze the effect of NMES1 on mitochondrial respiration using MDMs, we turned to the THP-1 based overexpression model instead. CIV activity was measured in THP-1 cells transduced to express NMES1 or mCherry in a doxycycline-dependent manner. There was no difference whatsoever in CIV activity between NMES1 and mCherry expressing cells or the non-induced control ("NMES1 -dox") (Figure 13A). This is in contrast to findings of Lee *et al.*, which suggested that NMES1 overexpression leads to a small but significant decrease in CIV activity [109]. As described above, in MDMs, NMES1 expression is induced upon stimulation with TLR ligands (see Figure 7). It is therefore conceivable that the effect of NMES1 is stimulation-dependent. However, as shown in Figure 13B, NMES1 expression in combination with R848 stimulation had no effect on CIV activity. These data contradict our initial hypothesis that NMES1 might be a negative regulator of the electron transport chain.

Next, we generated polyclonal NDUFA4 k/o THP-1 cells to study the effect of NMES1 on CIV activity in absence of NDUFA4. First, we characterized the untransduced cells: Of note, NDUFA4 k/o THP-1 cells proliferated at approximately half the rate of wildtype or TBX21 k/o cells and exhibited increased acidification of the culture medium, suggesting an effect on metabolism. Surprisingly, there was no difference between wildtype, TBX21 k/o and NDUFA4 k/o cells detectable with regard to basal and maximal respiration, as measured in mitochondrial stress tests (Figure 13C). The editing efficiencies were 100 %, 96 %, and 87 % for NDUFA4 k/o #1, NDUFA4 k/o #2 and TBX21 k/o cells, respectively, as determined using the ICE CRISPR analysis tool [179]. Loss of NDUFA4 expression was confirmed by western blotting (Figure 13D). We performed additional experiments to investigate whether the loss of NDUFA4 affects mitochondrial respiration in the context of TLR stimulation: Pam_3CSK_4 stimulation did not result in any changes in basal respiration, and the spare respiratory capacity remained largely unchanged (Figure 13E).

Knockdown of NDUFA4 has been reported to lead to a significant decrease in CIV activity [109, 129]. We could confirm these results using polyclonal NDUFA4 k/o THP-1 cells (Figure 13F & G). Interestingly, reconstitution with either NDUFA4 or NMES1 was sufficient to restore CIV activity in these cells. Thus, NMES1 and NDUFA4 appear to be redundant with regard to CIV activity.
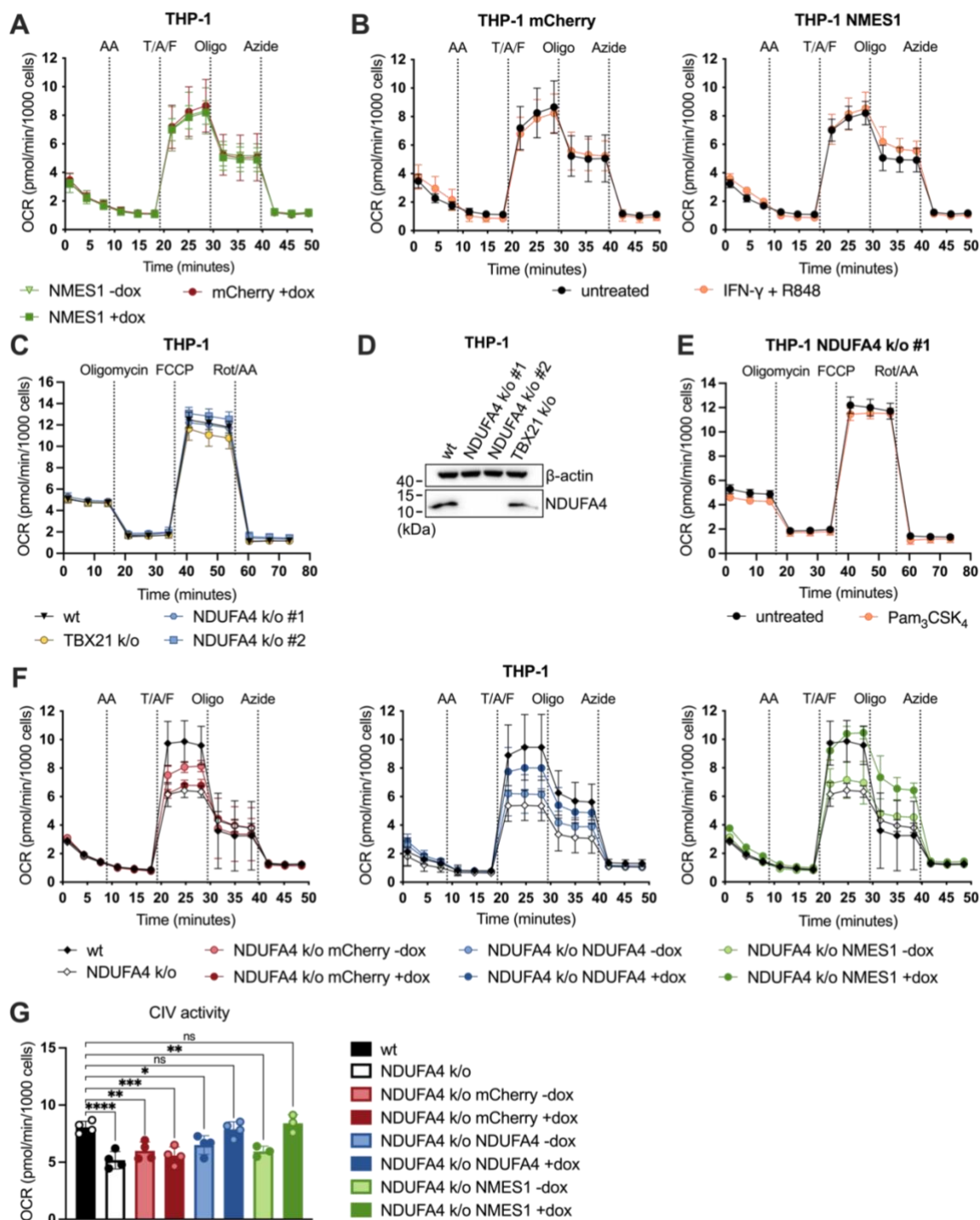
Figure 13. NMES1 and NDUFA4 are redundant regarding complex IV activity. (A) & **(B)** THP-1 cells expressing mCherry or NMES1 in a doxycycline-dependent manner were differentiated and treated with doxycycline for approx. 24 hours. Where indicated, cells were primed with IFN-γ for 6 hours, followed by overnight stimulation with R848. Thereafter, complex IV activity was measured. Error bars indicate the SD. AA = antimycin A; T/A/F = TMPD, ascorbate & FCCP; Oligo = oligomycin A; Azide = potassium azide. n = 2. **(C)-(E)** THP-1 wildtype, NDUFA4 k/o and TBX21 k/o cells were differentiated. **(E)** Cells were stimulated with Pam₃CSK₄ overnight or left untreated. Subsequently, a mitochondrial stress test was carried out. Error bars indicate the SD. Rot/AA = rotenone/antimycin A. n = 2. **(D)** Lysates generated from cells used in **(C)** & **(E)** were analyzed by western blotting. Cells were harvested in RIPA lysis buffer supplemented with protease inhibitor. SDS-PAGE was carried out using 12 % bis-tris gels. Equal amounts of protein were loaded in each lane. **(F)** NDUFA4 k/o THP-1 cells expressing mCherry, NMES1 or NDUFA4 in a doxycycline-dependent manner were used to measure complex IV activity as described for **(A)**. wt,

NDUFA4 k/o, NDUFA4 k/o NDUFA4: n = 4. NDUFA4 k/o NMES1: n = 3. **(G)** Complex IV activity was calculated using data derived from experiments described in **(F)**. Error bars indicate the SD. Statistical analysis was carried out using one-way ANOVA (Dunnett's multiple comparisons test). ns = P > 0.05, * = P ≤ 0.05, ** = P ≤ 0.01, *** = P ≤ 0.001, **** = P ≤ 0.0001.

To investigate whether the decrease in CIV activity upon loss of NDUFA4 leads to changes in glycolysis, we performed glycolysis stress tests on NDUFA4 k/o THP-1 cells. As expected, NDUFA4 k/o cells exhibited an increase in glycolysis (Figure 14A). The glycolytic capacity was not affected. Hence, the loss of NDUFA4 also resulted in a lower glycolytic reserve. The differences in glycolysis and glycolytic reserve were significant only for NDUFA4 k/o #1, likely owing to the lower knock-out efficiency for NDUFA4 k/o #2. As mentioned above, NDUFA4 k/o cells exhibit decreased proliferation rates compared to wildtype cells. Therefore, the proportion of wildtype cells in the pool may increase over time.

Surprisingly, overexpression of NMES1 or NDUFA4 in NDUFA4 k/o THP-1 cells did not restore glycolytic activity to wildtype levels (Figure 14B). We speculate that, since cells are driven towards a glycolytic phenotype under cell culture conditions [204], short-term induction of NMES1 or NDUFA4 expression may not be sufficient to revert the effects of the NDUFA4 knock-out.
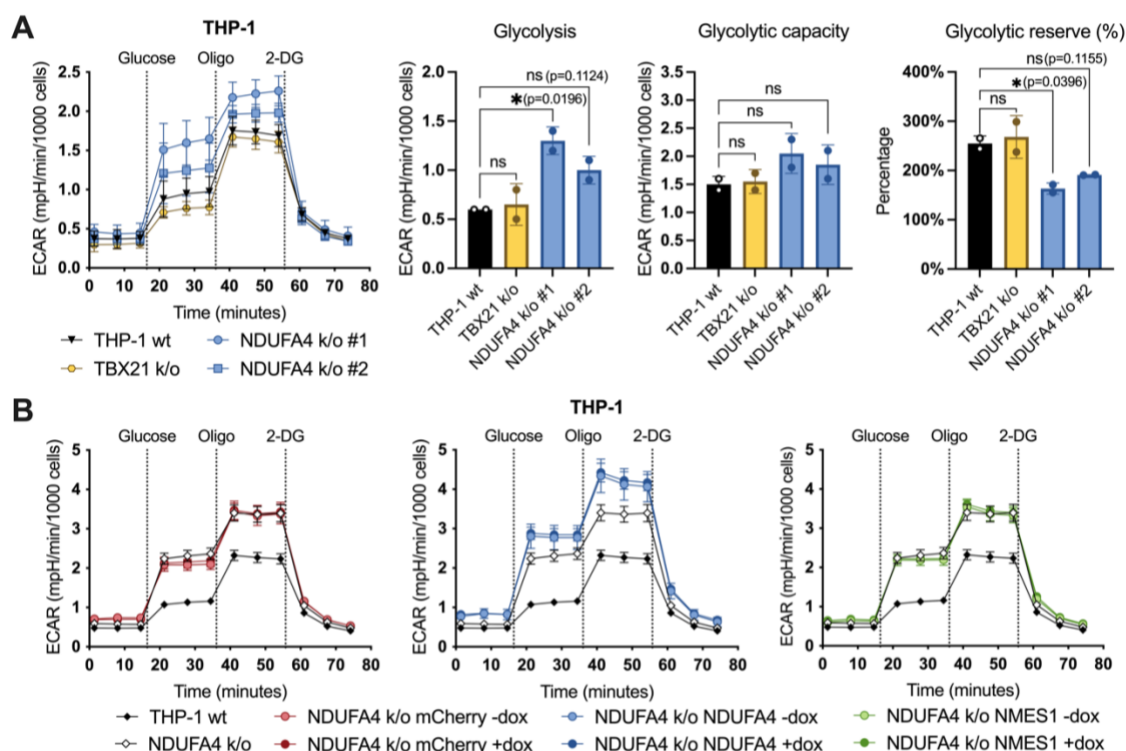
Figure 14. NDUFA4 k/o cells exhibit an increase in glycolysis. (A) THP-1 wildtype, NDUFA4 k/o and TBX21 k/o cells, or **(B)** NDUFA4 k/o THP-1 cells expressing mCherry, NMES1 or NDUFA4 in a doxycycline-dependent manner were differentiated and treated with doxycycline for 24 hours where indicated. **(A)** & **(B)** A glycolysis stress test was carried out. 2-DG = 2-deoxy-D-glucose. Statistical analysis was carried out using one-way ANOVA (Dunnett's multiple comparisons test). ns = P > 0.05, * = P ≤ 0.05.

4.2.5. NMES1 does not seem to affect mitochondrial ROS production

The electron transport chain is a major source of reactive oxygen species (ROS) [161]. Together with ROS produced by NADPH oxidase, mitochondrial ROS (mtROS) contribute to microbial killing by macrophages [163]. Since NMES1 is a component of CIV of the electron transport chain, it is conceivable that upregulation of NMES1 expression also affects mtROS production. Interestingly, Tello *et al.* reported that the hypoxia-mediated induction of NDUFA4L2, a homolog of NMES1, results in CI inhibition and a concomitant decrease in mtROS [130]. To investigate the effect of NMES1 on mtROS production, we performed MitoSOX flow cytometry on THP-1 cells expressing NMES1 in a doxycycline-dependent manner (Figure 15A-C). Scatter plots for one experiment are shown in Figure 15A as an example. There was no clear trend regarding the median fluorescence intensity under any of the conditions tested (Figure 15B). We confirmed that NMES1 was indeed expressed in the respective samples by western blotting (Figure 15C). In addition, pro-IL-1β could be detected in samples derived from R848 stimulated cells, showing that stimulation was successful. Interestingly, we could observe a slight decrease in NDUFA4 protein levels upon R848 stimulation. Furthermore, doxycycline-induced cells yielded a stronger signal for pro-IL-1β upon R848 stimulation compared to untreated controls, suggesting that NMES1 might enhance the NF-κB response. However, as we did not include mCherry expressing cells as a control, we could not rule out the possibility of this effect being caused by the doxycycline treatment. Both effects were observed throughout all experiments, although the extent varied between replicates.

As NDUFA4 k/o THP-1 cells exhibit a marked decrease in CIV activity, we performed MitoSOX flow cytometry on these cells to determine whether this has any impact on mtROS production. Experiments were performed using NDUFA4 k/o THP-1 cells expressing NDUFA4 in a doxycycline-dependent manner, and doxycycline-treated cells were included as a control. The scatter plots from one out of two experiments are shown in Figure 15D. There was also no clear difference between cells lacking NDUFA4 expression and the reconstituted control regarding median fluorescence intensity (Figure 15E). We confirmed NDUFA4 expression for the doxycycline-treated control by western blotting (Figure 15F). Taken together, we could not detect any NMES1 or NDUFA4-dependent changes in mtROS production under any of the conditions tested.
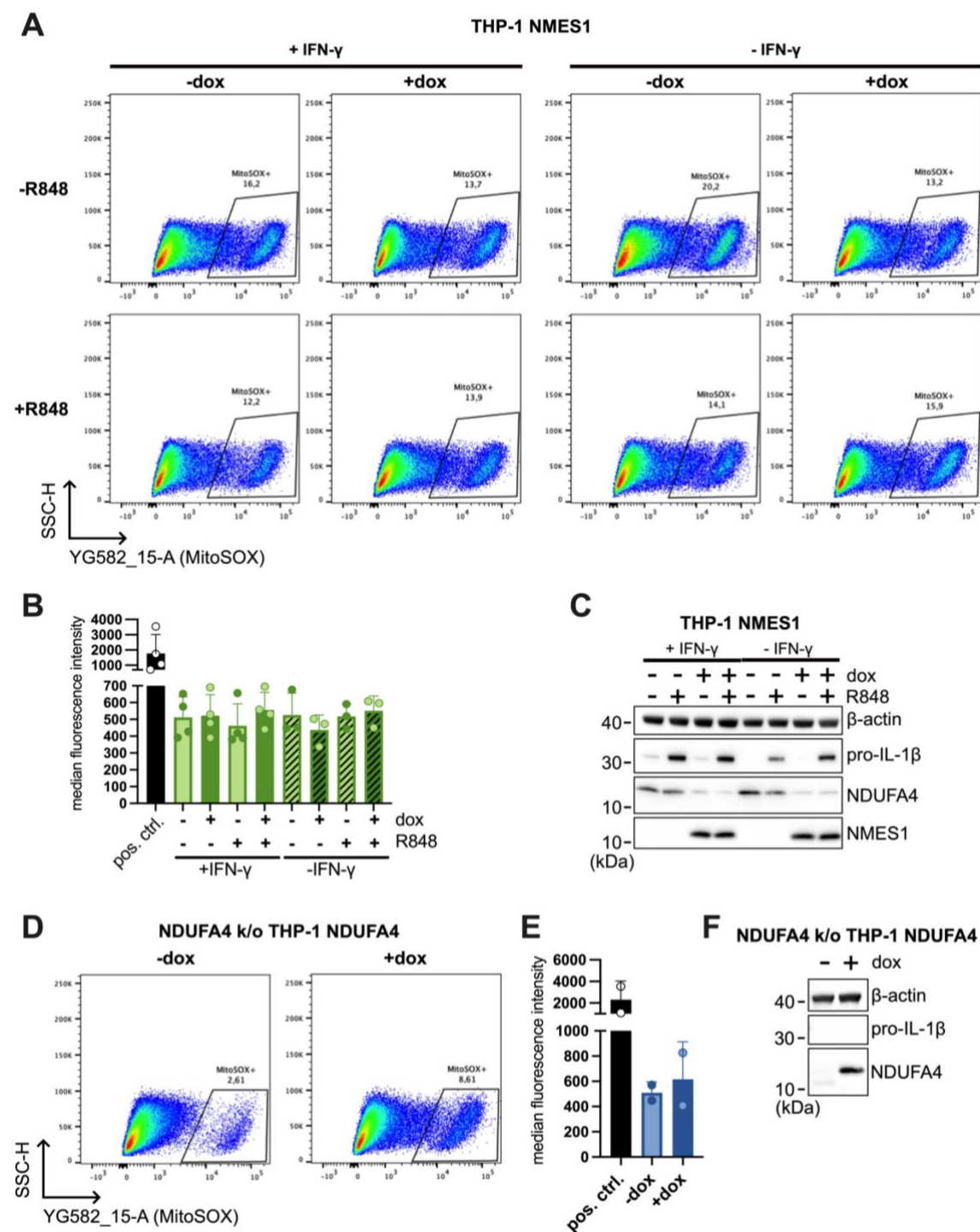
Figure 15. NMES1 does not seem to affect mitochondrial ROS production. (A)-(C) THP-1 cells expressing NMES1 in a doxycycline-dependent manner were differentiated and treated with doxycycline for approx. 24 hours. Where indicated, cells were primed with IFN-γ for 6 hours, followed by overnight stimulation with R848. Cells were stained with MitoSOX and analyzed by flow cytometry. As a positive control (pos. ctrl.), cells treated with 5 µM antimycin A for 20 minutes were included. with IFN-γ priming: n = 4. without IFN-γ priming: n = 3. **(D)-(F)** NDUFA4 k/o THP-1 cells expressing NDUFA4 in a doxycycline-dependent manner were differentiated and treated with doxycycline for approx. 24 hours. Cells were stained with MitoSOX and analyzed by flow cytometry. As a positive control (pos. ctrl.), cells treated with 5 µM antimycin A for 20 minutes prior to analysis were included. n = 2. **(A) & (E)** Scatter plots for one representative experiment are shown. **(B) & (E)** Median fluorescence intensity for MitoSOX was calculated. Error bars indicate the SD. **(C) & (F)** Cells were harvested in RIPA lysis buffer supplemented with protease inhibitor. SDS-PAGE was carried out using 12 % bis-tris gels. Equal amounts of protein were loaded in each lane.

4.2.6. The squirrel pox homolog of NMES1 displaces NDUFA4 from CIV

Sorouri *et al.* reported three viral homologs for NMES1 and NDUFA4, with the squirrel pox homolog sharing the most homology with NMES1 [110]. An alignment of the amino acid sequences of human (hs) and squirrel pox (sqp) NMES1 generated using BLASTp is shown in Figure 16A. The amino acid sequences are highly similar, with 47 % identities and 66 % positives. An AlphaFold prediction of the structure of hsNMES1 is shown in Figure 16B, with identities and positives highlighted in red and blue, respectively.

Due to the high similarity between hsNMES1 and sqpNMES1, it is conceivable that the viral homolog is able to integrate into CIV of the ETC. Therefore, we hypothesized that NMES1 may have evolved to protect host cells against pathogens: Viral homologs might displace NDUFA4 from CIV to alter ETC activity. NMES1, on the other hand, might exhibit higher affinity to the complex, thereby protecting host cells against the effects of the viral homolog. To test this hypothesis, experiments were carried out in HEK293T cells expressing sqpNMES1 in a doxycycline-dependent manner. Additional experiments were carried out in an NDUFA4 k/o background to detect possible redundancies between NDUFA4 and sqpNMES1.

CIV activity was measured for NDUFA4$^{-/-}$ single cell clones to select a suitable clone that exhibits a decrease in CIV activity, as observed for THP-1 NDUFA4 k/o cells (Figure 13F). CIV activity was reduced to a similar extent in all NDUFA4$^{-/-}$ clones tested. Clone 1B3 was used for subsequent experiments (Figure 16C).

Next, mitochondria were isolated from HEK293T wildtype cells and NDUFA4$^{-/-}$ clone 1B3 expressing mCherry or sqpNMES1-Strep in a doxycycline-dependent manner. A western blot comparing whole cell lysates and mitochondrial lysates shows that sqpNMES1 indeed localizes to the mitochondria (Figure 16D). Furthermore, in HEK293T wildtype cells expressing sqpNMES1-Strep, NDUFA4 levels were decreased compared to the mCherry expressing control (Figure 16D).
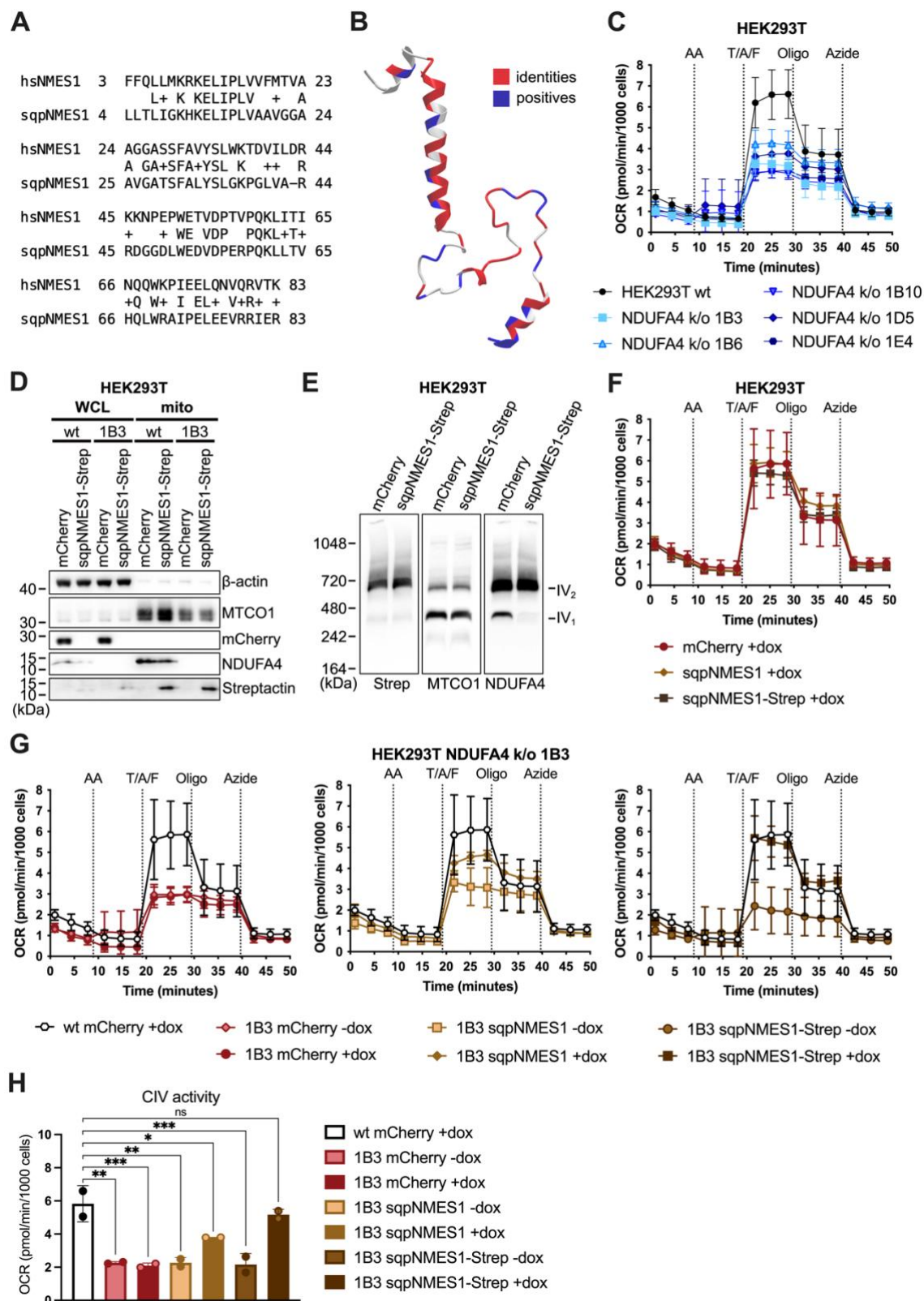
Figure 16. The squirrel pox homolog of NMES1 displaces NDUFA4 from CIV. (A) Amino acid sequence alignment of human (hs) and squirrel pox (sqp) NMES1 (NP_115789.1 and YP_008658503.1, respectively), generated using NCBI BLASTp [102, 103]. **(B)** AlphaFold prediction of the structure of hsNMES1, with positives and identities from the amino acid sequence alignment described in **(A)** highlighted in blue and red, respectively. Generated using iCn3D [205]. **(C)** CIV activity was measured for HEK293T wildtype cells and NDUFA4$^{-/-}$ single cell clones. Error bars indicate the SD. AA = antimycin A; T/A/F = TMPD, ascorbate & FCCP; Oligo = oligomycin A;

Azide = potassium azide. n = 1. **(D)** & **(E)** Mitochondria were isolated from HEK293T wildtype cells and NDUFA4$^{-/-}$ clone 1B3 expressing mCherry or sqpNMES1-Strep in a doxycycline-dependent manner. Cells were harvested approx. 24 hours after doxycycline induction. **(D)** SDS-PAGE was carried out comparing whole cell lysates (WCL) and lysates from isolated mitochondria (mito). Cells and mitochondria were harvested in RIPA lysis buffer supplemented with protease inhibitor. SDS-PAGE was carried out using 4-12 % bis-tris gels. Equal amounts of protein were loaded in each lane. n = 2. **(E)** BN PAGE was carried out loading equal amounts of mitochondrial protein per lane. Note that the anti-Strep-tag antibody only gave an unspecific signal. n = 2. **(F)** & **(G)** Complex IV activity was measured for **(F)** HEK293T wildtype and **(G)** HEK293T NDUFA4$^{-/-}$ clone 1B3 cells expressing sqpNMES1(-Strep) in a doxycycline-dependent manner. HEK293T wildtype cells expressing mCherry in a doxycycline-dependent manner were included as a reference. Error bars indicate the SD. AA = antimycin A; T/A/F = TMPD, ascorbate & FCCP; Oligo = oligomycin A; Azide = potassium azide. n = 2. **(H)** Complex IV activity was calculated using data derived from experiments described in **(F)**&**(G)**. Error bars indicate the SD. Statistical analysis was carried out using one-way ANOVA (Dunnett's multiple comparisons test). ns = P > 0.05, * = P ≤ 0.05, ** = P ≤ 0.01, *** = P ≤ 0.001.

Interestingly, BN PAGE revealed a drastic decrease in CIV-associated NDUFA4 upon induction of sqpNMES1 expression (Figure 16E). Since the anti-Strep-tag antibody used only yielded unspecific bands for BN PAGE experiments, we can only infer that sqpNMES1-Strep replaces NDUFA4 based on the highly conserved amino acid sequence between hsNMES1 and sqpNMES1. The decrease in NDUFA4 levels observed upon expression of sqpNMES1 also supports this notion (Figure 16D).

To investigate the consequences of the replacement of NDUFA4 by sqpNMES1, we then measured CIV activity in these cells. Similar to overexpression of human NMES1 in THP-1 cells, sqpNMES1(-Strep) did not affect CIV activity when expressed in HEK293T wildtype cells (Figure 16F). Surprisingly, we found that sqpNMES1 restores CIV activity when expressed in HEK293T NDUFA4 k/o cells (Figure 16G&H). This effect was stronger for the Strep-tagged protein. However, as there is no antibody against sqpNMES1 available, it is possible that there are differences in expression levels and/or stability of the tagged and untagged protein.

On a side note, BLASTp search also revealed homologs for NDUFA4 and NMES1 in bacteria (Figure 17). A homolog of NMES1 was identified in an unclassified *Erythrobacter* species. Homologs of both NMES1 and NDUFA4 were identified in *S. aureus*, *N. humilatus* and *N. antri*. Homologs of NDUFA4 were, among others, identified in *L. monocytogenes* and *E. faecium*. Importantly, since the samples used to identify homologs in *S. aureus, L. monocytogenes* and *E. faecium* were collected from humans, in these cases, cross-contamination with human DNA is possible. Homologs for NDUFA4 and NMES1 have, however, also been reported for bacterial samples derived from sediment and soil (e.g., *N. humilatus* and *N. antri)*, suggesting that bacterial homologs might indeed exist.
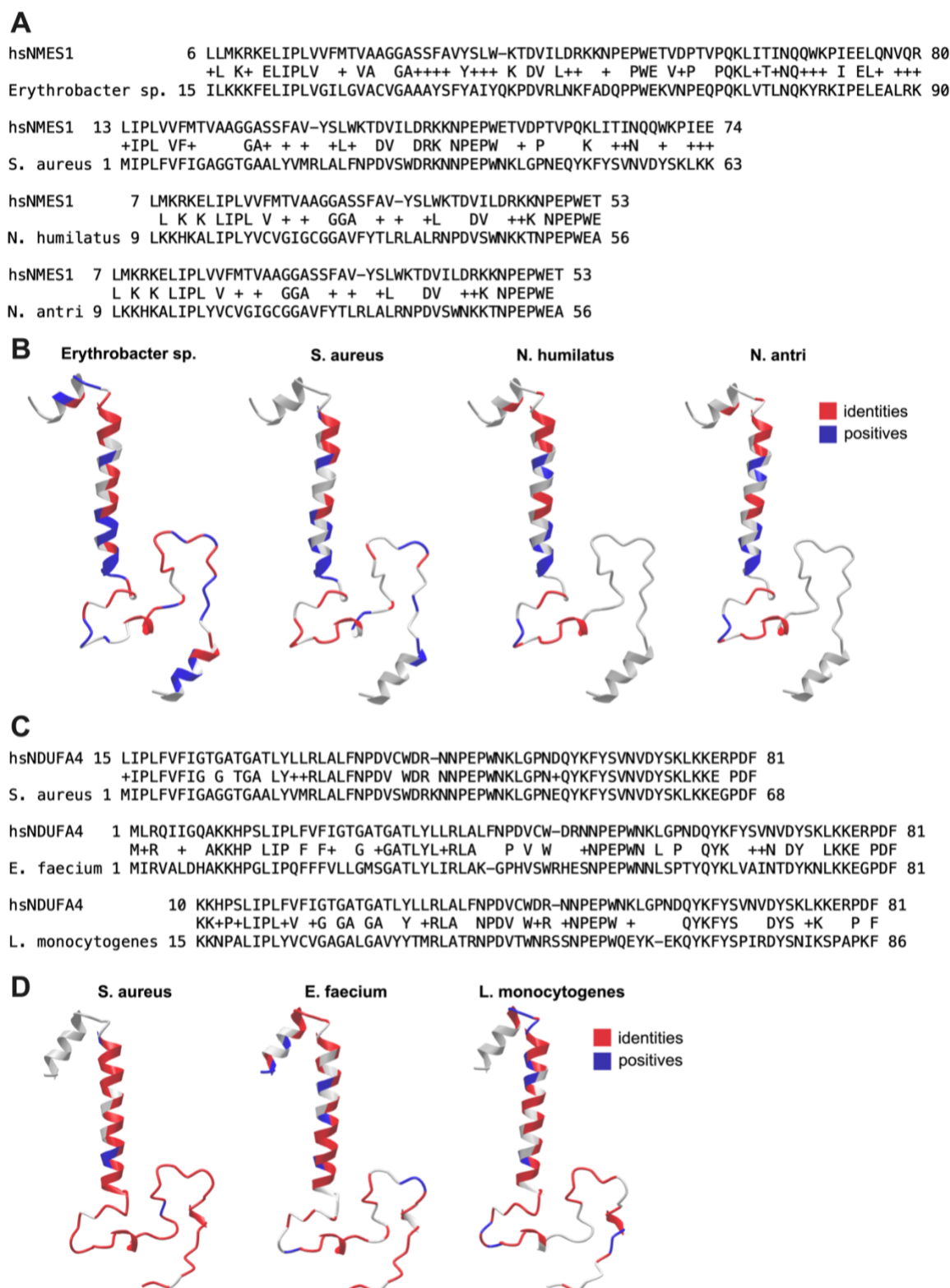
A

```
hsNMES1              6 LLMKRKELIPLVVFMTVAAGGASSFAVYSLW-KTDVILDRKKNPEPWETVDPTVPQKLITINQQWKPIEELQNVQR 80
                       +L K+ ELIPLV  + VA  GA++++ Y+++ K DV L++  +  PWE V+P  PQKL+T+NQ+++ I EL+ +++
Erythrobacter sp.   15 ILKKKFELIPLVGILGVACVGAAAYSFYAIYQKPDVRLNKFADQPPWEKVNPEQPQKLVTLNQKYRKIPELEALRK 90

hsNMES1             13 LIPLVVFMTVAAGGASSFAV-YSLWKTDVILDRKKNPEPWETVDPTVPQKLITINQQWKPIEE 74
                       +IPL VF+     GA+ + +  +L+ DV  DRK NPEPW + P   K ++N + +++
S. aureus            1 MIPLFVFIGAGGTGAALYVMRLALFNPDVSWDRKNNPEPWNKLGPNEQYKFYSVNVDYSKLKK 63

hsNMES1              7 LMKRKELIPLVVFMTVAAGGASSFAV-YSLWKTDVILDRKKNPEPWET 53
                          L K K LIPL V + +  GGA  + +  +L   DV  ++K NPEPWE
N. humilatus         9 LKKHKALIPLYVCVGIGCGGAVFYTLRLALRNPDVSWNKKTNPEPWEA 56

hsNMES1              7 LMKRKELIPLVVFMTVAAGGASSFAV-YSLWKTDVILDRKKNPEPWET 53
                          L K K LIPL V + +  GGA  + +  +L   DV   ++K NPEPWE
N. antri             9 LKKHKALIPLYVCVGIGCGGAVFYTLRLALRNPDVSWNKKTNPEPWEA 56
```

B

C

```
hsNDUFA4            15 LIPLFVFIGTGATGATLYLLRLALFNPDVCWDR-NNPEPWNKLGPNDQYKFYSVNVDYSKLKKERPDF 81
                       +IPLFVFIG G TGA LY++RLALFNPDV WDR NNPEPWNKLGPN+QYKFYSVNVDYSKLKKE PDF
S. aureus            1 MIPLFVFIGAGGTGAALYVMRLALFNPDVSWDRKNNPEPWNKLGPNEQYKFYSVNVDYSKLKKEGPDF 68

hsNDUFA4             1 MLRQIIGQAKKHPSLIPLFVFIGTGATGATLYLLRLALFNPDVCW-DRNNPEPWNKLGPNDQYKFYSVNVDYSKLKKERPDF 81
                       M+R + AKKHP LIP F F+ G +GATLYL+RLA  P V W  +NPEPWN L P  QYK ++N DY LKKE PDF
E. faecium           1 MIRVALDHAKKHPGLIPQFFFVLLGMSGATLYLIRLAK-GPHVSWRHESNPEPWNNLSPTYQYKLVAINTDYKNLKKEGPDF 81

hsNDUFA4            10 KKHPSLIPLFVFIGTGATGATLYLLRLALFNPDVCWDR-NNPEPWNKLGPNDQYKFYSVNVDYSKLKKERPDF 81
                       KK+P+LIPL+V +G GA GA Y +RLA  NPDV W+R +NPEPW +    QYKFYS  DYS +K   P F
L. monocytogenes    15 KKNPALIPLYVCVGAGALGAVYYTMRLATRNPDVTWNRSSNPEPWQEYK-EKQYKFYSPIRDYSNIKSPAPKF 86
```

D

Figure 17. Homologs of NMES1 and NDUFA4 also exist in bacteria. (A) Amino acid sequence alignment of human (hs) NMES1 (NP_115789.1) with homologs from *Erythrobacter sp.* SN021 (WP_236926243.1), *Staphylococcus aureus* (MBO8905138.1), *Nocardioides humilatus* (KAA1412537.1), and *Nocardioides antri* (KAA1414767.1). Generated using NCBI BLASTp [102, 103]. **(C)** Amino acid sequence alignment of hsNDUFA4 (NP_002480.1) with homologs from *Staphylococcus aureus* (MBO8905138.1), *Enterococcus faecium* (PWS22687.1) and *Listeria monocytogenes* (MBH0213473.1). **(B)** & **(D)** AlphaFold prediction of the structure of **(B)** hsNMES1 and **(D)** hsNDUFA4, with positives and identities from the amino acid sequence alignments shown in **(A)**& **(C)** highlighted in blue and red, respectively. Generated using iCn3D [205].

91

4.3. Analyzing the effect of NMES1 on pro-inflammatory cytokine release

4.3.1. Genome-edited MDMs yield inconsistent results

To investigate whether NMES1 plays a role in the inflammatory response, we measured the release of the pro-inflammatory cytokines IL-6 and TNF using ELISA. First, we performed experiments in MDMs that had been subjected to genome editing. Similar to the experiments investigating electron transport chain activity, we could not obtain consistent results using genome-edited MDMs (Figure 18A & B). Importantly, in some experiments, IL-6 and/or TNF release seemed to be blunted regardless of the gene targeted. Except for NDUFA4, where the gRNA combination used in initial experiments resulted only in approx. 30 % knock-out efficiency (Figure 18C, Do 172), knock-out efficiencies between experiments were similar (80-100 %). Therefore, the variation in knock-out efficiency alone cannot explain the differences observed between donors. Overall, the results obtained were not reliable enough to draw any conclusions with regard to the effect of NMES1 on pro-inflammatory cytokine release.
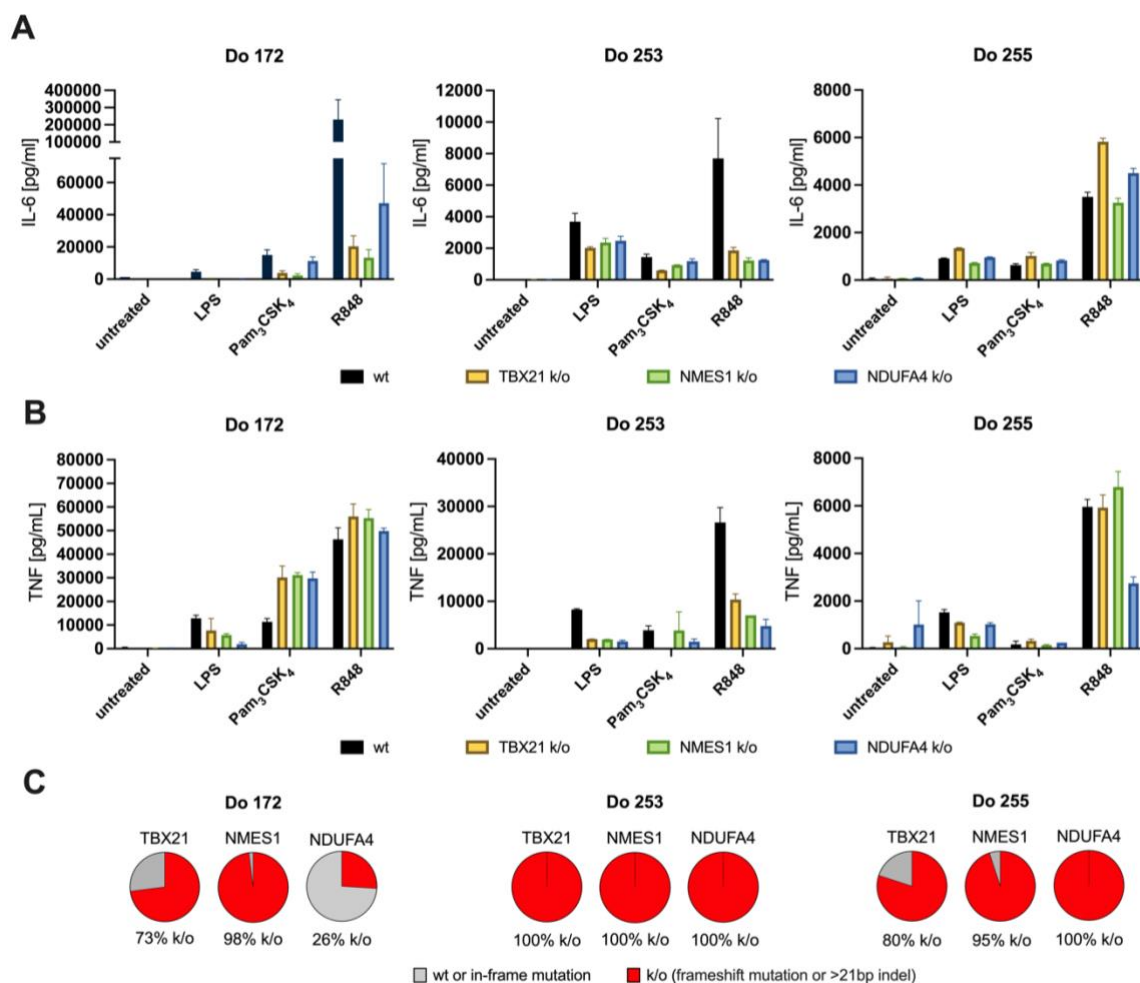
Figure 18. Genome editing in MDMs affects cytokine release regardless of the gene edited. Monocytes were isolated using the Pan monocyte isolation kit. Subsequently, RNP-mediated

genome editing was carried out, targeting the indicated gene. Unedited (wt) cells were included as a control. Cells were differentiated for 5 days. Thereafter, cells were stimulated with LPS, Pam_3CSK_4, or R848 for 16 hours. Supernatants were collected and IL-6 and TNF release was measured using ELISA, shown in **(A)** and **(B)**, respectively. Error bars indicate SD. **(C)** Knock-out efficiencies as determined by Sanger sequencing and subsequent analysis using the ICE CRISPR analysis tool [179]. Results from three donors are shown as a representative. n = 4 biological replicates.

4.3.2. *Overexpression of NMES1 or NDUFA4 leads to an increase in TNF release*

Having established that genome-edited MDMs are not suited to study the effect of NMES1 on pro-inflammatory cytokine release, we performed experiments using THP-1 cells expressing NMES1 in a doxycycline-dependent manner. In addition, THP-1 cells expressing NDUFA4 or sqpNMES1(-Strep) in a doxycycline-dependent manner were included to investigate the effect of overexpression of these proteins on pro-inflammatory cytokine release. mCherry-expressing cells were used as a control. Interestingly, in cells overexpressing either NMES1 or NDUFA4, TNF release was increased upon stimulation with Pam_3CSK_4 or R848 (Figure 19A). Compared to cells that were not treated with doxycycline, the increase was approximately two-fold. Despite the same trend being observed across all experiments, this increase was only significant for NDUFA4-expressing cells stimulated with Pam_3CSK_4 (Figure 19A, bottom right graph). We did not observe a clear trend for cells expressing sqpNMES1(-Strep) with regard to TNF release. Furthermore, IL-6 release was not affected by overexpression of any of the proteins tested (Figure 19B). To ensure that the respective protein is indeed expressed upon doxycycline induction, we performed western blot analysis on lysates generated from cells after harvesting the supernatants (Figure 19C). Bands for mCherry, NMES1, NDUFA4, and sqpNMES1-Strep could be detected in the respective lanes. In addition, overexpression of untagged sqpNMES1, similar to sqpNMES1-Strep, resulted in a decrease in NDUFA4 protein levels, indicating that the untagged protein is expressed.

To investigate whether loss of NDUFA4 expression affects pro-inflammatory cytokine release, we performed the same experiment using THP-1 wildtype, NDUFA4 k/o and TBX21 k/o cells. We could not detect any significant differences in TNF or IL-6 release between these cell lines (Figure 19D & E).

Overall, these results indicate that, in contrast to our initial hypothesis, NMES1 is a pro-inflammatory protein that promotes TNF release downstream of TLR signaling.
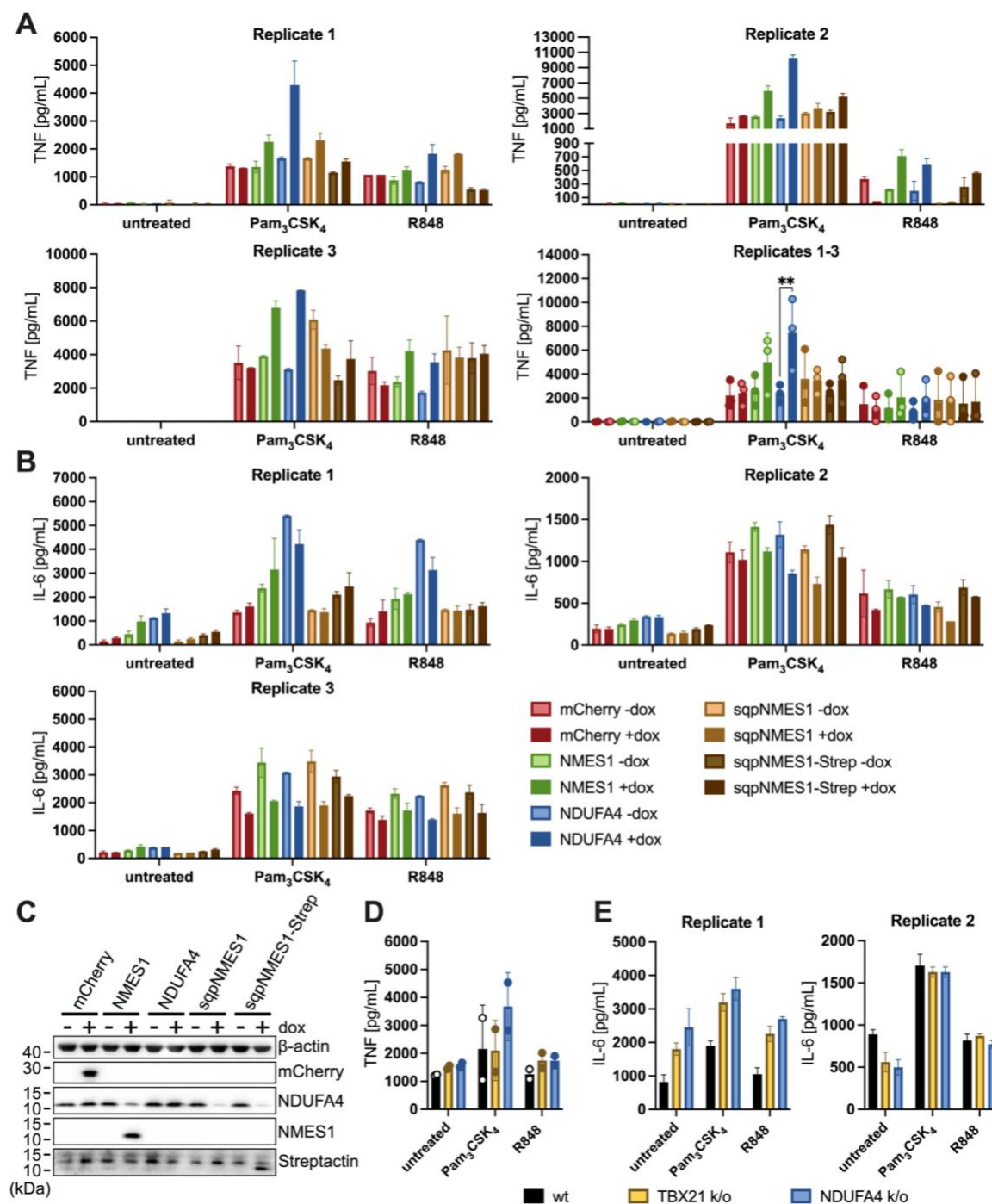
Figure 19. Overexpression of NMES1 or NDUFA4 leads to an increase in TNF release. (A)-(C) THP-1 cells expressing the indicated protein in a doxycycline-dependent manner were differentiated and transgene expression was induced by adding doxycycline. Cells were stimulated using Pam_3CSK_4 or R848 for 14 hours. Supernatants were collected and TNF and IL-6 release was measured using ELISA, shown in **(A)** and **(B)**, respectively. n = 3. For **(A)**, the bottom right graph shows a summary of all three replicates. Dots indicate the mean from each individual experiment. Statistical analysis was carried out using two-way ANOVA (Tukey's multiple comparisons test). ns = P > 0.05, ** = P ≤ 0.01. Results of the statistical analysis are only displayed for comparisons where P ≤ 0.05. **(C)** Western blot performed using Laemmli lysates generated after harvesting supernatants. **(D)** & **(E)** THP-1 wildtype, NDUFA4 k/o and TBX21 k/o cells were differentiated and stimulated using Pam_3CSK_4 or R848 for 14 hours. Supernatants were collected and TNF and IL-6 release was measured using ELISA, shown in **(D)** and **(E)**, respectively. n = 2. **(A)-(E)** Error bars indicate SD.

4.3.3. Overexpression of NMES1 or NDUFA4 leads to a stimulation-dependent increase in TNF expression

To elucidate whether the increase of TNF release is accompanied by an increase in TNF mRNA expression levels, we performed qPCR on THP-1 cells expressing NMES1, NDUFA4 or mCherry in a doxycycline-dependent manner. Indeed, we observed a moderate, but statistically significant increase in TNF mRNA expression levels after 4 hours of Pam_3CSK_4 stimulation compared to the mCherry-expressing control (Figure 20A). In contrast, differences in expression levels of TNFAIP3 and ICAM-1, two additional NF-κB target genes, were not significant.

mRNA expression levels of TNF and TNFAIP3 have been reported to be increased as early as one hour after TLR stimulation [206, 207]. Therefore, we performed additional experiments to determine whether the differences in mRNA expression levels are more prominent at an earlier timepoint. We observed a similar trend as seen for the 4-hour timepoint after one hour of Pam_3CSK_4 stimulation (Figure 20B). However, the differences observed were not statistically significant.

As we could also detect an increase in TNF release in cells overexpressing NMES1 or NDUFA4 in the context of R848 stimulation, we performed additional qPCR experiments to measure TNF mRNA expression levels upon R848 stimulation (Figure 20C). In contrast to Pam_3CSK_4 stimulation, we could not detect any differences in expression levels of TNF after 4 hours of R848 stimulation. This could be explained by the fact that the amount of TNF released upon stimulation with R848 varied between experiments, and, on average, was low as compared to Pam_3CSK_4 stimulation (Figure 19A).

In summary, the increase of TNF mRNA expression levels in NMES1 or NDUFA4 expressing cells correlates with the increase in TNF release measured by ELISA. As expression levels of TNFAIP3 and ICAM-1 were not affected, it seems as though the effect is specific to TNF. However, additional experiments are required to elucidate whether NMES1 specifically affects TNF expression or whether other early NF-κB target genes are also affected.
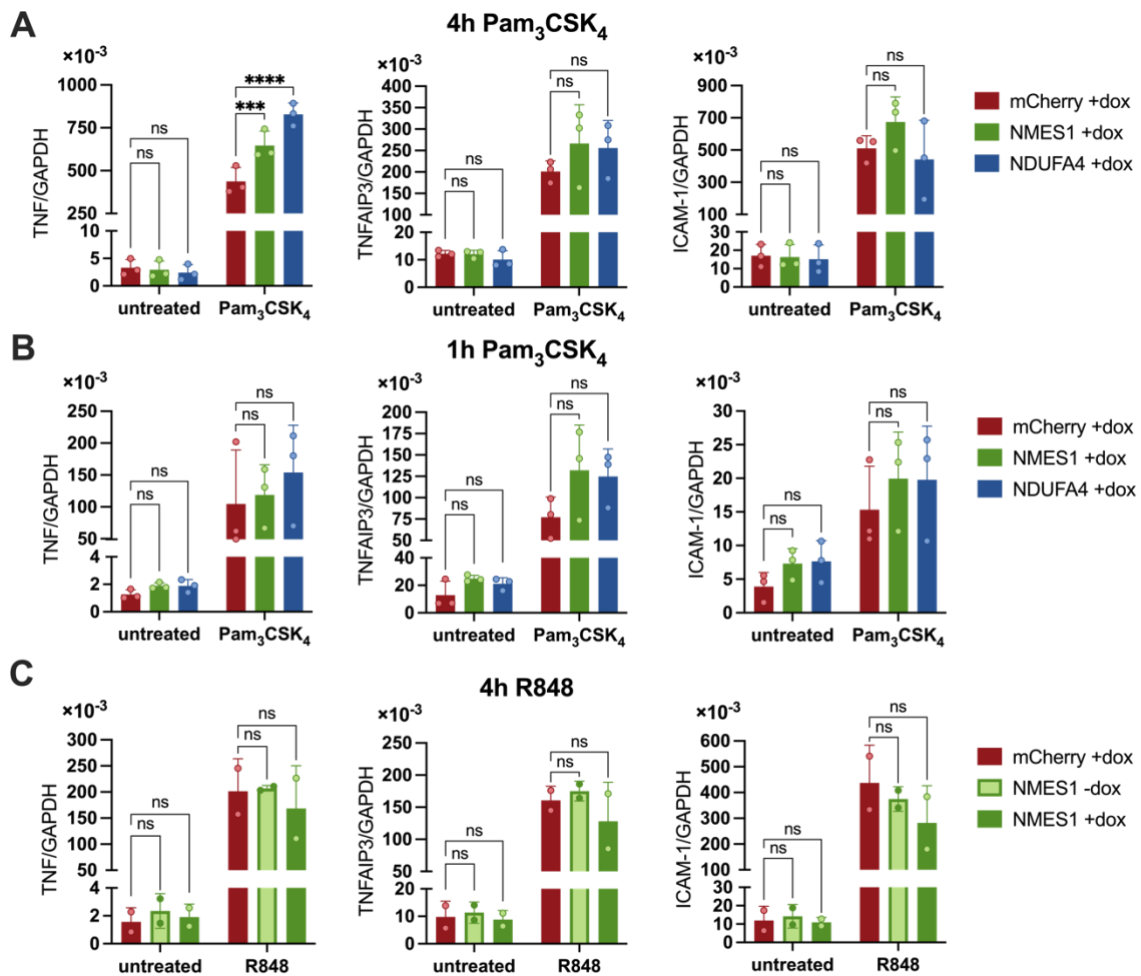
Figure 20. Overexpression of NMES1 or NDUFA4 leads to a stimulation-dependent increase in TNF expression. THP-1 cells expressing the indicated protein in a doxycycline-dependent manner were differentiated and transgene expression was induced by adding doxycycline (dox). On the next day, cells were stimulated with Pam_3CSK_4 for **(A)** 4 hours, or **(B)** 1 hour; for **(C)**, cells were stimulated with R848 for 4 hours. Samples were analyzed by qPCR. Relative expression was calculated using GAPDH as a reference. Error bars indicate the SD. **(A)** & **(B)**: n = 3, **(C)**: n = 2. Statistical analysis was carried out using two-way ANOVA (Dunnett's multiple comparisons test). ns = P > 0.05, *** = P ≤ 0.001, **** = P ≤ 0.0001.

4.3.4. Transgene silencing and low transgene expression make U-937 and BLaER2 cells unsuitable as cell culture models

In attempt to recapitulate the findings regarding ETC activity and cytokine release in other cell lines, U-937 and BLaER2 based overexpression models were set up. Transduced U-937 cells initially showed NMES1 protein levels comparable to LPS-stimulated MDMs (Figure 21A), however, after less than three weeks in culture, NMES1 expression could no longer be detected (Figure 21B). Cells were treated with doxycycline only for up to 18 hours for the western blot shown in Figure 21B. However, based on previous results generated using both HEK293T and THP-1 based overexpression systems, we would have expected to be able to detect NMES1 expression after 18 hours of doxycycline treatment (Figure 11A & B).

In addition, we generated NDUFA4$^{-/-}$ single cell clones from BLaER2 cells and confirmed the absence of NDUFA4 expression by sequencing and western blotting (Figure 21C). In BLaER1 cells, the parental cell line of BLaER2, out of all TLRs, TLR4 and TLR8 are most highly expressed (Figure 21D). We therefore stimulated these cells with LPS and R848 to investigate possible differences with regard to pro-inflammatory cytokine release. Interestingly, IL-6 release was reduced by approx. 50 % in NDUFA4$^{-/-}$ BLaER2 compared to wildtype cells (Figure 21E), whereas TNF release varied between clones and did not show a clear trend (Figure 21F). This is in contrast to results obtained using THP-1 cells, where loss of NDUFA4 expression did not affect pro-inflammatory cytokine release (Figure 19D & E). We then transduced BLaER2 wildtype and NDUFA4$^{-/-}$ single cell clones A5 and A6 to express mCherry, NMES1(-FLAG) or NDUFA4(-FLAG) in a doxycycline-dependent manner. Western blots generated using lysates derived from transduced BLaER2 wildtype cells and NDUFA4$^{-/-}$ clone A6 are shown as an example (Figure 21G-I). Unfortunately, NMES1 expression was extremely low and barely detectable in some experiments (Figure 21G-I). Lysates generated from THP-1 cells transduced with the same construct were loaded to confirm that the antibody staining was successful in general (Figure 21G & H). Furthermore, NDUFA4 expression levels achieved in transduced NDUFA4$^{-/-}$ clones A5 and A6 were visibly lower compared to endogenous NDUFA4 protein levels detected in BLaER2 wildtype cells (Figure 21I). In contrast to U-937 cells, for which transgene expression levels decreased over time, in BLaER2 cells, transgene expression was low but remained stable over several weeks. Importantly, NDUFA4 k/o THP-1 cells were transduced with the same viral supernatants as the BLaER2-based overexpression model. High transgene expression levels could be achieved in these cell lines, showing that the low levels of transgene expression were not caused by low titers of lentivirus (data not shown). Hence, the transducability of BLaER2 cells appears to be low in general. Taken together, our attempts to establish a U-937 or BLaER2-based model to study NMES1 were unsuccessful.
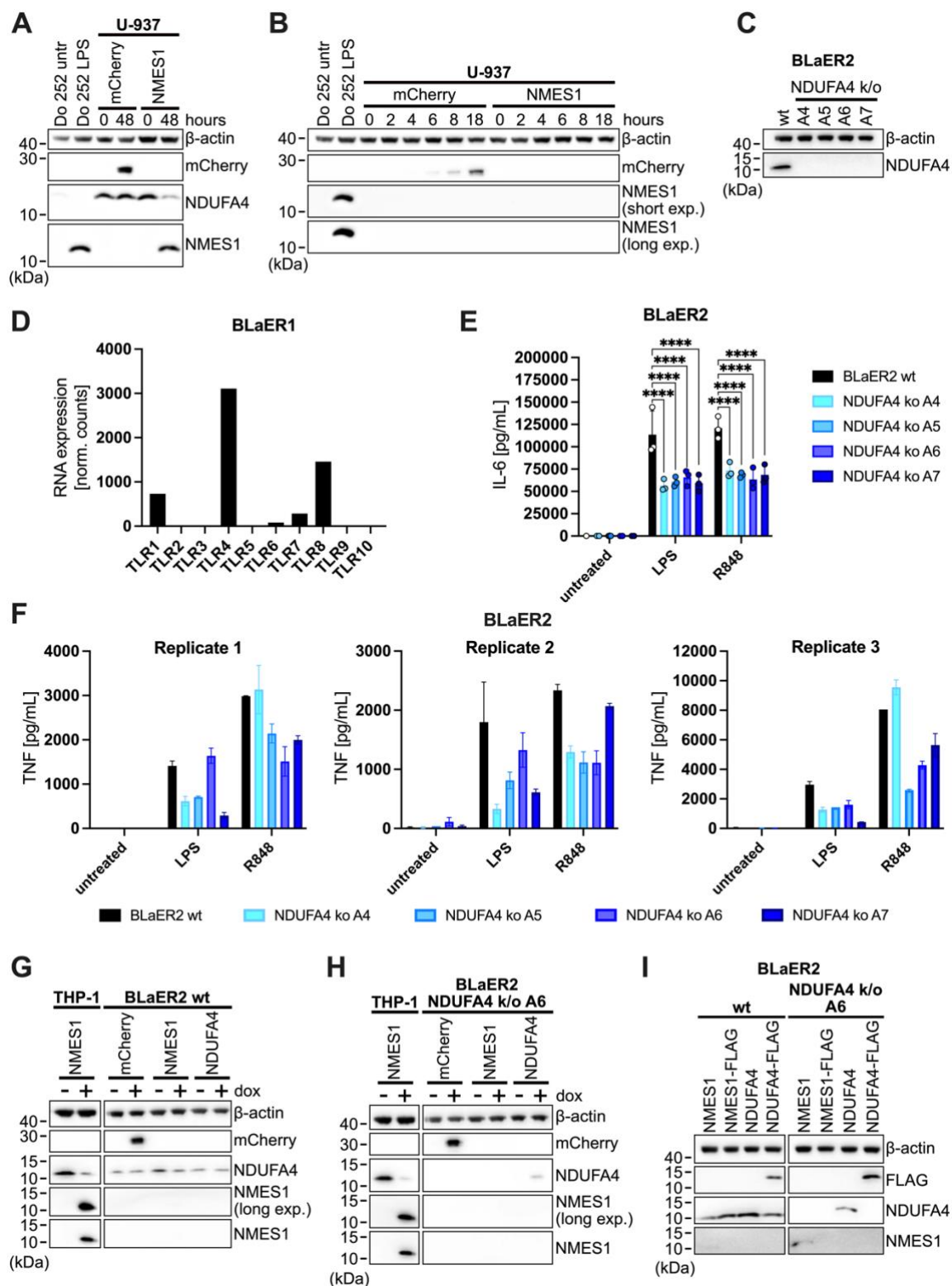
Figure 21. U-937 and BLaER2 cells unsuitable as overexpression models. (A) & **(B)** U-937 cells expressing NMES1 or mCherry in a doxycycline-dependent manner were differentiated and subsequently treated with doxycycline for the duration indicated. Cells were harvested in RIPA lysis buffer supplemented with protease inhibitor. Lysates generated from untreated (untr) and LPS-stimulated MDMs (Do 252) were included as a reference. SDS-PAGE was carried out using 12 % bis-tris gels. Equal amounts of protein were loaded in each lane. **(C)**, **(E)** & **(F)** BLaER2 wildtype cells and NDUFA4$^{-/-}$ single cell clones were differentiated and stimulated with the TLR ligand indicated for 14 hours. Thereafter, supernatants were collected and IL-6 and TNF release was measured using ELISA (shown in **(E)** and **(F)**, respectively). For **(C)**, cells from the "untreated"

condition were washed once with PBS and harvested in 1× Laemmli buffer. SDS-PAGE was carried out using 12 % bis-tris gels. **(E)** & **(F)** Error bars indicate SD. Individual points show the mean of one biological replicate. For TNF, biological replicates are shown in separate graphs. n = 3. Statistical analysis was carried out using two-way ANOVA (Dunnett's multiple comparisons test). ns = P > 0.05, * = P ≤ 0.05, ** = P ≤ 0.01, *** = P ≤ 0.001, **** = P ≤ 0.0001. For readability, results of the statistical analysis are only displayed for comparisons where P ≤ 0.05. **(D)** RNA expression levels of different TLRs in LPS-stimulated BLaER1 cells. RNA sequencing data were kindly generated by Fionan O'Duill. **(G)** & **(H)** BLaER2 wildtype cells and NDUFA4$^{-/-}$ single cell clone A6 expressing the indicated protein in a doxycycline-dependent manner were differentiated and treated with doxycycline for 48 hours. Cells were washed once with PBS and harvested in 1× Laemmli buffer. SDS-PAGE was carried out using 4-12 % bis-tris gels. Samples derived from THP-1 cells expressing NMES1 in a doxycycline-dependent manner were included as a control. n = 3. **(I)** BLaER2 wildtype cells and NDUFA4$^{-/-}$ single cell clone A6 expressing the indicated protein in a doxycycline-dependent manner were treated with doxycycline for 24 hours. Cells were harvested in RIPA lysis buffer supplemented with protease inhibitor and SDS-PAGE was carried out using a 4-12 % bis-tris gel. Equal amounts of protein were loaded in each lane. n = 1.

4.4. Searching for a role of NMES1 beyond electron transport chain activity and cytokine release

4.4.1. The interactomes of NMES1 and NDUFA4 differ

To identify potential functions of NMES1 beyond electron transport chain activity, and to unravel the mechanism through which NMES1 expression impacts TNF release, we performed LC-MS/MS analyses. In addition, these experiments should give insight into possible functional differences between NMES1 and its homolog NDUFA4. We performed co-immunoprecipitation of NMES1-FLAG and NDUFA4-FLAG using a buffer containing the mild detergent digitonin to ensure that electron transport chain complexes remain intact. As a reference, mitochondrial localization signal-tagged (MLS) mCherry-FLAG was included. Here, the MLS of COX8A was used. Co-immunoprecipitated proteins were then identified using LC-MS/MS.

First, the digitonin concentration was titrated to determine the lowest concentration at which mitochondrial membranes are solubilized. It has been reported that at high concentrations of digitonin, aggregates of incompletely solubilized protein may be entrapped in liquid dispersions, which generates artefacts [208]. Concentrations between 0.04 % and 1 % digitonin were tested, since a digitonin to protein ratio of 6 g/g was estimated to be achieved within this range for the number of cells used. THP-1 cells expressing NMES1-FLAG in a doxycycline-dependent manner were used. No signal for NMES1, NDUFA4 or MTCO1 could be detected at 0.04 % digitonin, indicating that the mitochondrial membranes were not solubilized (Figure 22A). For all other concentrations tested, mitochondrial proteins could be detected. With this experiment, we could also confirm that NMES1 and NDUFA4 are mutually exclusive components of complex IV, as recently published by Lee *et al.* [109]: We could co-immunoprecipitate MTCO1, but not NDUFA4, in the FLAG-IP. For subsequent experiments, lysis buffer containing 0.16 % digitonin was used.

To avoid competition between endogenous NDUFA4 and NDUFA4-FLAG for interaction partners, for LC-MS/MS analysis, NDUFA4 k/o THP-1 cells were transduced with the above-mentioned constructs. To show that the co-immunoprecipitation is also successful using these cell lines, we generated samples in duplicate, eluting bound protein from the beads using low pH elution buffer for one set of samples. These samples were then analyzed by western blotting. We observed that NMES1-FLAG protein levels were much lower than those of NDUFA4-FLAG, as shown by the anti-FLAG staining (Figure 22B). Furthermore, NMES1-FLAG levels were below the detection limit in the eluate. In a subsequent experiment, we boiled the beads in 1× Laemmli buffer instead, and a strong signal was obtained for NMES1, suggesting that when using low pH elution buffer, a considerable amount of protein remains bound to the beads (data not shown). In LC-MS/MS measurements, NMES1 was readily identified as
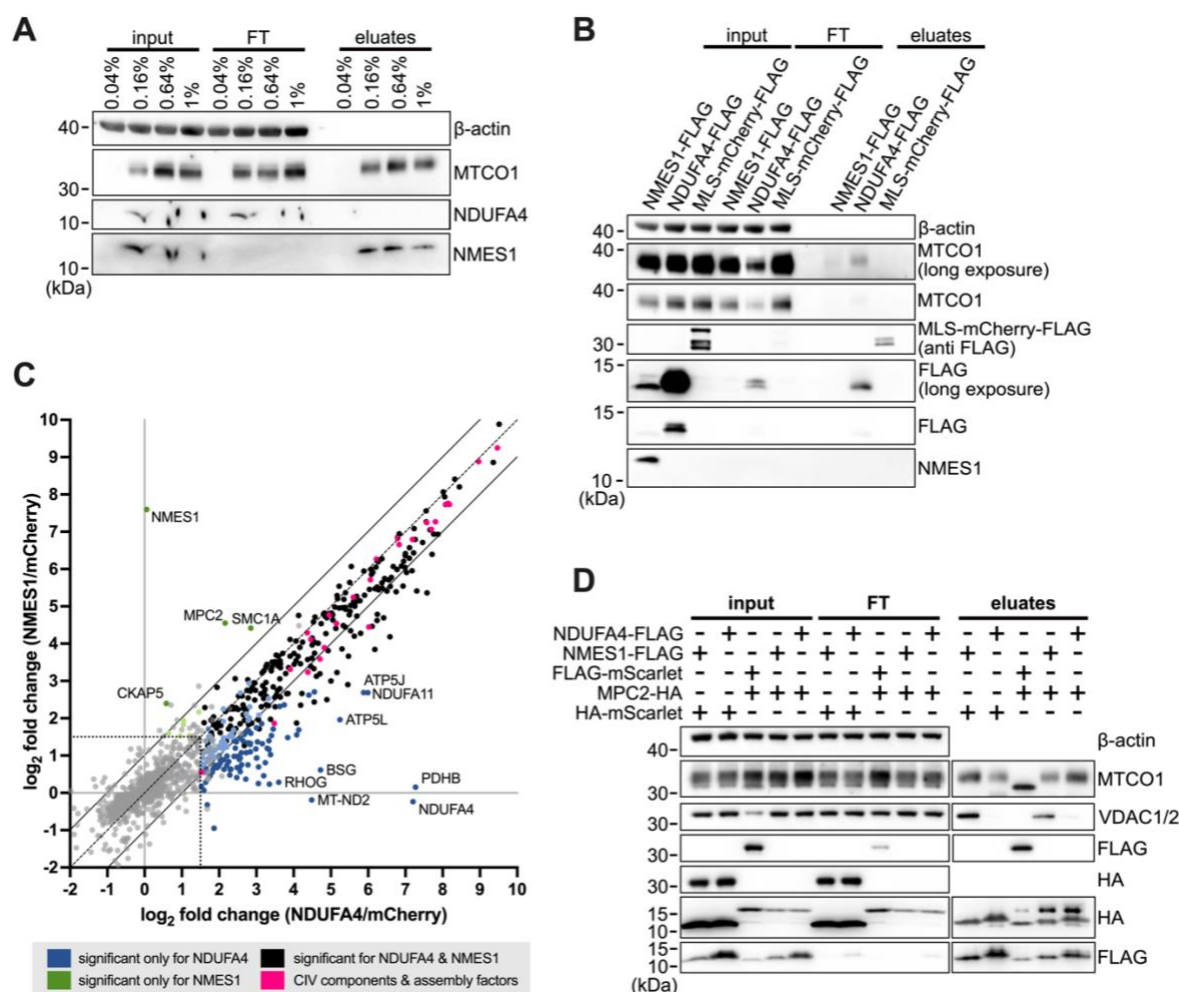
Figure 22. The interactomes of NMES1 and NDUFA4 differ. (A) THP-1 wildtype cells expressing NMES1-FLAG in a doxycycline-dependent manner were differentiated and treated with doxycycline for 24 hours. Thereafter, cells were harvested in mito co-IP lysis buffer containing the indicated concentration of digitonin and lysed using a syringe. **(B)** NDUFA4 k/o THP-1 cells expressing the indicated FLAG-tagged protein in a doxycycline-dependent manner were differentiated and treated with doxycycline for 24 hours. Thereafter, cells were harvested in mito co-IP lysis buffer containing 0.16 % digitonin and lysed using a syringe. **(A)** & **(B)** FLAG-IP was carried out at 4 °C overnight. Thereafter, bound protein was eluted using low pH elution buffer. SDS-PAGE was carried out using a 12 % bis-tris gel. **(C)** Co-IP was carried out as described for **(B)**. Instead of eluting proteins using low pH elution buffer, an on-bead digest was carried out and samples were prepared for LC-MS/MS analysis. The scatter plot shows the $\log_2$ fold change enrichment of proteins for IP of NMES1-FLAG vs. NDUFA4-FLAG as compared to the MLS-mCherry-FLAG control. Statistical significance was evaluated using a two-sided Student's t-test (permutation-based FDR <0.005, S0 = 0.3). Furthermore, the cut-off for the $\log_2$ fold change was set to 1.5 (indicated by black dotted lines). Proteins only significant for NMES1-FLAG are highlighted in light and dark green, proteins only significant for NDUFA4-FLAG are highlighted in light and dark blue, proteins significant for both NMES1-FLAG and NDUFA4-FLAG are highlighted in black, non-significant proteins or proteins below the $\log_2$ fold change cut-off are marked in grey. Finally, proteins with a $\log_2$ fold change difference ≥1 between NMES1-FLAG and NDUFA4-FLAG co-IP were identified (highlighted in dark green and dark blue, respectively). n = 4 biological replicates per condition. **(D)** HEK293T cells were transfected with constructs encoding the indicated proteins. 24 hours after transfection, cells were harvested in mito co-IP lysis buffer containing 0.16 % digitonin and lysed using a syringe. FLAG-IP was carried out at 4 °C. Elution was carried out using low pH elution buffer. Subsequently, the beads were boiled in 1× Laemmli buffer to elute remaining protein from the beads. Note that for MTCO1 and FLAG-mScarlet, images corresponding to the low pH elution are shown. For all other stainings, images corresponding to the Laemmli elution are presented.

significantly enriched in the respective samples, as were NDUFA4 and MLS-mCherry (Figure 22C). To better visualize proteins enriched for NMES1 and NDUFA4, the axes were cut off. Therefore, the data point for MLS-mCherry (x = -12.59, y = -12.07) is not shown.

Apart from COX8A, whose MLS was used to tag mCherry, all 12 remaining components of CIV were found to significantly interact with both NMES1 and NDUFA4 and yielded similar $\log_2$ fold changes compared to the MLS-mCherry control. Furthermore, except for COX15, which was found to significantly interact with NDUFA4 but not NMES1, all assembly factors of CIV detected were found to significantly interact with both NMES1 and NDUFA4. In general, only three proteins were found to significantly interact with NMES1 but not NDUFA4, whereas 88 proteins were found to significantly interact with NDUFA4 but not NMES1. Out of these 88 proteins, 49 localize to the mitochondria. Only one mitochondrial protein, mitochondrial pyruvate carrier 2 (MPC2), was identified to significantly and specifically interact with NMES1. Co-enrichment of MPC2 could be detected in samples derived from both NMES1-FLAG and NDUFA4-FLAG expressing cells. However, the association was only significant for NMES1 but not NDUFA4. MPC2 forms heterodimers with MPC1 to make up a functional pyruvate carrier [209], and MPC1 was not detected in the LC-MS/MS analysis. Significant interactors of NDUFA4 (but not NMES1) included several components and assembly factors of CI and CV of the ETC, including NDUFA11, MT-ND2 and TMEM126B, and ATP5J, ATP5L, MT-ATP6 and MT-ATP8, respectively.

To validate the interaction between NMES1 and MPC2, we performed co-immunoprecipitation on samples derived from HEK293T cells transiently co-transfected with constructs encoding NMES1-FLAG (or NDUFA4-FLAG) and MPC2-HA. As a control, these three constructs were combined with HA-mScarlet or FLAG-mScarlet encoding constructs, respectively. Bands for MPC2-HA could be detected in the respective eluates, confirming the interaction of NMES1 and NDUFA4 with MPC2 (Figure 22D). For MTCO1, a known interactor of NMES1 and NDUFA4, bands could be observed for all samples containing either NMES1 or NDUFA4, but not for the control sample containing MPC2 and mScarlet, suggesting that there was no unspecific binding of protein to the beads. To account for the possibility of non-specific binding of mitochondrial proteins to NMES1-FLAG and NDUFA4-FLAG, blots were stained for VDAC1/2. As we could detect VDAC1/2 in all eluates derived from NMES1-FLAG containing samples, we cannot exclude the possibility that the interaction between NMES1 and MPC2 is non-specific.

In summary, it seems as though the function of NMES1 may be explained by the absence of interaction with certain proteins. For example, NMES1 and NDUFA4 might differentially affect supercomplex assembly. However, additional experiments are required to support this hypothesis.

4.4.2. NMES1 overexpression does not result in major changes in the transcriptome

To determine whether overexpression of NMES1 leads to any changes in the transcriptome, we performed RNAseq analysis on THP-1 cells expressing NMES1 or mCherry in a doxycycline-dependent manner. Both doxycycline-induced mCherry expressing cells and uninduced NMES1 expressing cells were included as a reference.

Firstly, we wanted to analyze the effect of NMES1 expression alone at different timepoints. To this end, cells were treated with doxycycline for 4, 8, 16, or 24 hours. Note that overexpressed NMES1 and mCherry could not be detected in these analyses, since the vector used for overexpression does not provide a poly(A) signal. Transcripts that are not polyadenylated were lost during library preparation due to the use of oligo dT primers. No differentially expressed genes were detected after 4 and 8 hours of doxycycline treatment. After 16 hours, only few differentially expressed genes were identified (Figure 23A). The highest number of differentially expressed genes was detected after 24 hours of doxycycline treatment (Figure 23B). As shown in Figure 23C, the comparison to the uninduced NMES1 expressing control yielded similar results as the comparison to doxycycline-induced mCherry expressing control (Figure 23B). As doxycycline itself may affect the transcriptome, the doxycycline-induced mCherry expressing control is shown as a reference for all further comparisons.

Regarding the differentially expressed genes which are upregulated upon NMES1 expression, there was no enrichment for a specific cellular process or pathway. Some of these genes have been implicated in the inflammatory response and/or electron transport chain activity: Thioredoxin (TXN), an important factor in the maintenance of redox homeostasis, has been found to be upregulated in TLR-ligand stimulated BMDMs [210]. Ferroportin-1 (SLC40A1) exports iron across the plasma membrane and is known to be highly expressed in macrophages resident to tissues involved in recycling of iron from erythrocytes [211]. Macrophages derived from mice with a heterozygous loss-of-function mutation in *Slc40a1* were reported to be more susceptible to intracellular bacterial growth [212]. In a more recent study, macrophages derived from myeloid-specific *Slc40a1* knock-out mice showed reduced mitochondrial respiratory spare capacity [213]. ADAMTS1 belongs to the family of disintegrin- and metalloproteinase domain containing proteins with thrombospondin motifs, which play an important role in the remodeling of extracellular matrix, and has been shown to aggravate liver fibrosis through the activation of TGF-β [214]. Finally, single nucleotide polymorphisms in the C21orf91 gene have been associated with an increased susceptibility to herpetic keratitis [215].
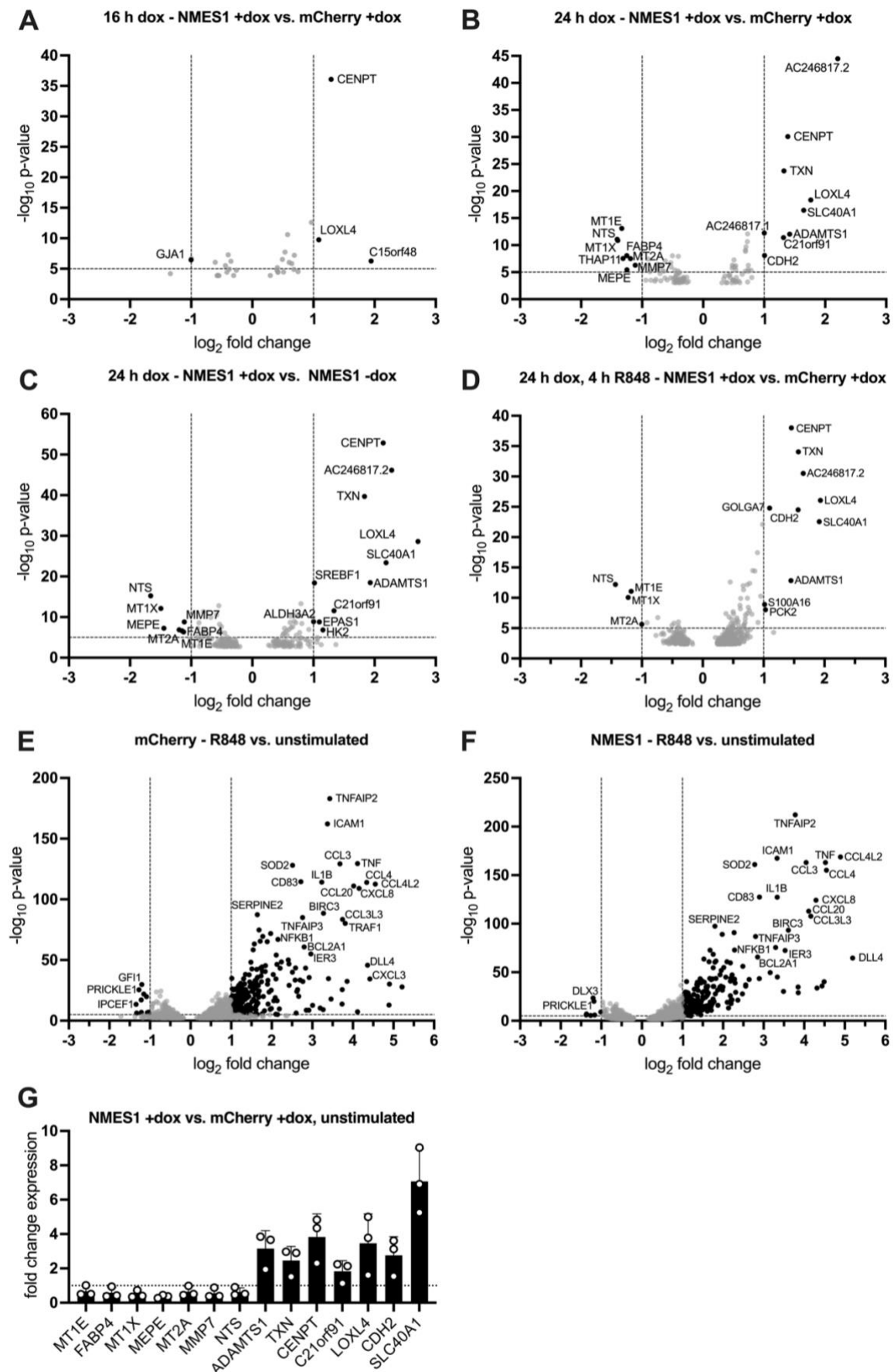
Figure 23. NMES1 overexpression does not result in major changes in the transcriptome.
(A)-(F) RNAseq was carried out on THP-1 cells expressing NMES1 or mCherry in a doxycycline-

dependent manner. Differentially expressed genes were identified using the R package DESeq2. The cut-offs for the $\log_2$ fold change = 1 and for the $-\log_{10}$ p-value = 5 are marked by dashed lines. Differentially expressed genes are marked in black. All other genes are marked in grey. n = 5 technical replicates per condition. Volcano plots comparing **(A)** NMES1 and mCherry expressing cells treated with doxycycline for 16 hours, **(B)** NMES1 and mCherry expressing cells treated with doxycycline for 24 hours, **(C)** NMES1 expressing cells treated with doxycycline for 24 hours to NMES1 expressing cells that remained untreated, **(D)** NMES1 and mCherry expressing cells treated with doxycycline for 24 hours and stimulated with R848 for 4 hours, **(E)** mCherry expressing cells that were stimulated with R848 for 4 hours or left unstimulated. Cells were treated with doxycycline for 24 hours before stimulation to induce transgene expression. **(F)** Volcano plot comparing NMES1 expressing cells that were stimulated with R848 for 4 hours or left unstimulated. Cells were treated with doxycycline for 24 hours before stimulation to induce transgene expression. **(G)** Validation of differentially expressed genes by qPCR. Fold change expression was calculated comparing NMES1 +dox (sample) against mCherry +dox (control). Dotted line: fold change expression = 1. Error bars indicate standard deviation. n = 3.

For the remaining genes which are upregulated upon NMES1 expression, no role in inflammatory or metabolic processes has been reported. Centromere protein T (CENPT) is required for centromere assembly [216]. AC246817.2 encodes a long non-coding RNA with no reported function. Cadherin 2 (CDH2) is a calcium-dependent cell adhesion protein. Lysyl oxidase like protein 4 (LOXL4) remains largely uncharacterized to date and belongs to the protein family of lysyl oxidases, which play a role in connective tissue maturation [217].

Regarding the differentially expressed genes which are downregulated upon NMES1 expression, several genes encoding proteins of the metallothionein family were identified, namely MT1E, MT1X and MT2A. Metallothioneins bind heavy metals, thereby conferring protection against metal toxicity [218]. Furthermore, they have been reported to act as free radical scavengers [218]. Neurotensin (NTS) has been suggested to play both pro- and anti-inflammatory roles in different tissues [219, 220]. However, to the best of our knowledge, neurotensin has not yet been studied in the context of immune cells. Fatty acid binding protein 4 (FABP4) has recently been reported to exert pro-inflammatory effects in acute kidney injury [221]. FABP4 expression is induced by LPS stimulation via JNK/c-Jun/AP-1 and has been described to be part of a positive feedback loop, thereby sustaining LPS-induced inflammatory signaling in macrophages [222]. Matrix metalloproteinase 7 (MMP7) has been reported to mediate TNF release in peritoneal macrophages [223]. Finally, matrix extracellular phosphoglycoprotein (MEPE) is involved in bone mineralization [224].

As we had observed an increase in TNF release upon stimulation with TLR ligands in NMES1 expressing cells (see Figure 19A), we wanted to investigate whether NMES1 leads to a general increase in early NF-κB target gene expression in this context. There were no R848 stimulation dependent differences with regard to differentially expressed genes (Figure 23B & D). Various NF-κB target genes, including TNFAIP2 and ICAM-1, were identified as differentially expressed in both mCherry and NMES1 expressing cells upon R848 stimulation, confirming that

R848 stimulation was indeed successful (Figure 23E & F). Importantly, as shown in Figure 19A, the amount of TNF released upon R848 stimulation varied between experiments and was, on average, much lower than the amount of TNF released upon Pam_3CSK_4 stimulation. As such, Pam_3CSK_4 would have been better suited to investigate possible stimulation-dependent effects of NMES1 on the transcriptome. In line with the RNAseq data presented here, we did not detect any significant differences in TNF mRNA expression levels in qPCR experiments after 4 hours of R848 stimulation (see Figure 20C).

Finally, we conducted qPCR analyses on selected transcripts to confirm the results of the RNAseq experiment (Figure 23G): As expected, expression levels of MT1E, FABP4, MT1X, MEPE, MT2A, MMP7 and NTS were decreased in NMES1 expressing cells compared to the mCherry expressing control. Furthermore, in line with the RNAseq data, expression of ADAMTS1, TXN, CENPT, C21orf91, LOXL4, CDH2 and SLC40A1 was upregulated in NMES1 expressing cells. Of note, the first primer pairs tested for MEPE and C21orf91 gave rise to off-target amplification products. As no alternative primer pairs detecting all reported isoforms could be designed, the primer pairs that finally were used for these genes do not detect all isoforms.

In summary, since differentially expressed genes were only detected at late timepoints after doxycycline induction, the effect of NMES1 overexpression on the transcriptome seems to be rather indirect. Furthermore, due to the experimental setup used, we could not conclude with certainty on whether or not NMES1 overexpression leads to TLR stimulation-dependent changes in the transcriptome.

5. DISCUSSION

5.1. The challenges of investigating the role of NMES1 *in vitro*

We initially attempted to study the role of NMES1 in primary human MDMs, however, we and others observed that electroporation of primary human monocytes leads to changes in OXPHOS and cytokine release (Figure 12C & E, Figure 18) and sustained mtROS production, respectively [111]. Therefore, we sought to identify a monocytic cell line that can be used as model instead.

Intriguingly, none of the monocytic cell lines tested herein endogenously express NMES1 under any of the conditions tested (Figure 8). In this context, it is worth mentioning that there is currently no human myeloid cell line of non-cancerous origin available. In theory, downregulation of NMES1 expression across all myeloid cancers would explain the absence of expression in monocytic cell lines. NMES1 has first been described as a potential tumor suppressor in esophageal squamous cell carcinoma [113, 114], while a more recent study found NMES1 expression to be upregulated in various cancers, including breast, ovarian, pancreatic and lung cancer [137]. To the best of our knowledge, due to the lack of appropriate healthy controls, it is currently unclear whether NMES1 expression is also differentially regulated in myeloid cancers.

In contrast to our findings, Sorouri *et al.* and Liu *et al.* showed that NMES1 expression can be induced by stimulation with IFN-γ in HL-60 cells or with LPS in THP-1 cells, respectively [108, 110]. However, expression was only analyzed on an RNA level in these publications, and no experimental evidence on a protein level was provided. With regard to THP-1, it is worth mentioning that this cell line inherently responds poorly to LPS stimulation due to the lack of CD14 expression [225]. Therefore, it is possible that protein levels in these cell lines remain below the detection limit of western blot analysis. Furthermore, NMES1 mRNA serves as pri-miRNA for miR-147b [108], and therefore mRNA expression levels might not directly translate into protein levels in this case.

HMC-1.1, a myeloid cell line used to study mast cells *in vitro*, is the only myeloid cell line that endogenously expresses NMES1 (Figure 8G). However, in contrast to primary monocytes and macrophages, this cell line constitutively expresses NMES1 and did not respond to stimulation with TLR ligands in any of the conditions tested. Therefore, HMC-1.1 was deemed unsuitable as a model to study NMES1.

We therefore turned to a THP-1-based overexpression model, which was used for the majority of experiments presented in this thesis. Needless to say, overexpression of proteins can generate artefacts and overexpression models may not fully represent the endogenous settings, for example, due to the lack of expression of components that act up- or downstream of the overexpressed protein. Baseline expression of NMES1 is low in primary human MDMs, with a

strong increase observed upon stimulation with TLR ligands (Figure 2). To more closely mimic these conditions, we opted for a doxycycline-inducible system for the expression of NMES1. Doxycycline is known to affect mitochondrial gene expression at concentrations that are typically used when working with doxycycline-inducible cell culture models [226]. We therefore included a control expressing mCherry in a doxycycline-dependent manner to control for possible side effects of doxycycline treatment. Furthermore, to account for the possibility of cell line-specific differences, we set out to generate overexpression models based on U-937 and BLaER2 (Figure 21). However, these attempts were unsuccessful due to transgene silencing and poor transgene expression, respectively.

In contrast to the overexpression model used, endogenous expression also gives rise to miR-147b, which is generated from the 3'-UTR of NMES1 gene transcripts (Figure 4). Furthermore, in the overexpression model, NMES1 is expressed independent of TLR ligand stimulation and subsequent activation of NF-κB. Therefore, we attempted to induce endogenous expression of NMES1 using CRISPRa in THP-1 and BLaER2 cells. Although we were able to induce NMES1 expression in THP-1 cells, the NMES1 protein levels achieved were much lower compared to LPS-stimulated MDMs (Figure 9C-E). We analyzed NDUFA4 protein levels to assess whether miR-147b expression is increased upon doxycycline-induced expression of dCas9-VPR. NDUFA4 protein levels remained stable, indicating that under the conditions tested, gene expression from the C15orf48 gene locus is low in general. The only commercially available antibody against human NMES1 is not suitable for flow cytometry analysis. Therefore, we were unable to determine whether upon induction of dCas9-VPR expression, all cells homogenously express low levels of NMES1 or whether few cells express high levels of NMES1. If the former is the case, an increase in NMES1 expression may be achieved by using different gRNAs. However, out of a panel of 5 gRNAs suggested for targeting the C15orf48 promoter region, only the two tested herein were predicted to have good on-target activity (0.96 and 0.83, respectively; Figure 9B). Targeting enhancer regions of the C15orf48 gene locus may result in higher NMES1 protein levels. Conversely, if NMES1 expression is high in only a subset of cells, sorting for cells with similar levels of NMES1 expression or generating single cell clones could be useful.

Finally, an iPSC-derived macrophage model has successfully been established in our laboratory [227, 228], and iPSC-derived macrophages deficient for NMES1 might represent a more suitable – albeit more time- and resource-intensive – model for studying the role of NMES1. iPSC-derived macrophages were shown to release IL-6 and TNF in response to LPS stimulation [227]. It is, however, unclear whether iPSC-derived macrophages endogenously express NMES1 upon stimulation with TLR ligands.

5.2. The effect of NMES1 and its homologs on the electron transport chain

In accordance with recent literature [109, 111], we could show that NMES1 is a component of CIV of the ETC, and that it predominantly migrates at the expected height of CIV_1 in BN PAGE (Figure 10). Intriguingly, 2D PAGE experiments consistently showed a strong, specific signal for NMES1 corresponding to a molecular weight below 66 kDa in the first dimension (Figure 10A-D). NDUFA4 also yielded a band at this height, but the signal intensity was much lower compared to the band at the height of IV_1. As resolution of BN PAGE is poor below a molecular weight of 100 kDa [229], it is possible that these bands correspond to the respective single protein. Alternatively, the bands could correspond to NMES1 and NDUFA4 interacting with other proteins, such as assembly factors or chaperones. We performed an LPS stimulation time course to analyze whether the CIV-associated proportion of NMES1 increases over time, but could not observe any difference between 14, 24 and 36 hours of LPS stimulation (data not shown). Thus, it seems that after LPS stimulation, the amount of NMES1-containing CIV reaches a plateau, despite NMES1 being present in excess. From these observations, it is tempting to infer that the amounts of NMES1- and NDUFA4-containing CIV are somehow regulated, thereby preventing a complete loss of NDUFA4-containing CIV upon upregulation of NMES1 expression. In contrast, we found that overexpression of the squirrel pox homolog of NMES1 leads to an almost complete loss of NDUFA4-containing CIV (Figure 16E). This will be discussed in more detail below.

In line with data published by Lee *et al.*, we found that NMES1 overexpression results in a decrease in NDUFA4 protein levels, independent of the presence of miR-147b [109] (Figure 11). Even though NMES1 expression is not completely absent in HEK293T cells (nTPM = 1.9 according to the Human Protein Atlas [195]), and has been reported to be induced upon LPS stimulation in THP-1 cells [108], amounts of miR-147b are probably negligible. As suggested by Lee *et al.,* NDUFA4 may be stabilized through its association with CIV, and consequently, displacement of NDUFA4 from the complex in presence of NMES1 may result in its degradation [109]. It remains to be determined how NDUFA4 is degraded. If NDUFA4 is indeed degraded upon being displaced from CIV, the degradation is likely mediated by ClpXP or LONP: These mitochondrial proteases are known to degrade proteins that have previously been incorporated into the inner mitochondrial membrane [230].

Having established that NMES1 integrates into CIV of the ETC, we investigated the effect of NMES1 on mitochondrial activity and CIV activity using metabolic flux assays. Interestingly, both NMES1 and NDUFA4 restored CIV activity when overexpressed in NDUFA4 k/o THP-1 cells (Figure 13F). However, as these

experiments did not control for possible differences in expression levels of NMES1 and NDUFA4, it is still possible that one protein is more efficient at restoring CIV activity than the other. Our data are in contrast to findings of Lee *et al.*, who reported a slight but significant decrease in CIV activity upon NMES1 overexpression [109]. These differences may be explained by the different cell types used: Lee *et al.* performed experiments using mitochondria isolated from AAV-transduced mouse heart tissue, or transduced HAECs or A549 cells.

Surprisingly, despite the drastic decrease in CIV activity upon loss of NDUFA4 expression, we were unable to detect any differences between wildtype and NDUFA4 k/o THP-1 cells in the mitochondrial stress test (Figure 13C). In assays such as the CIV activity assay, which use permeabilized cells, OXPHOS kinetics are saturated [231]. Therefore, such assays do not represent physiological conditions [231]. Due to the obvious decrease in proliferation and the increase in glycolysis in NDUFA4-deficient cells, we would have expected to see a difference in the mitochondrial stress test, which is more physiologically relevant. Interestingly, Lee *et al.* suggested that the apparent contradiction between the CIV activity assay and the mitochondrial stress test may be explained by the large excess capacity of CIV [109].

Sorouri *et al.* recently investigated the effect of sqpNMES1 on the response to apoptotic triggers [110]. Both loss of NMES1 and overexpression of sqpNMES1 led to a decrease in sensitivity to VSV-induced apoptosis in A549 cells [110]. In contrast, loss of NDUFA4 sensitized cells to apoptotic triggers [110]. Cogliati *et al.* previously suggested that cristae remodeling-induced disruption of mitochondrial function may contribute to apoptosis [153]. Hence, Sorouri *et al.* hypothesized that NMES1 and its homologs may modulate ETC activity or (super-)complex composition to regulate apoptosis upon viral infection [110, 232]. However, so far, no experimental evidence supporting this hypothesis has been provided. Here, we assessed the effect of sqpNMES1 on CIV composition and activity. We found that sqpNMES1 indeed integrates into CIV. Due to the lack of signal for Strep-tagged sqpNMES1, we failed to provide direct evidence. However, we observed a decrease in NDUFA4 protein levels in sqpNMES1 expressing cells (Figure 16D), similar to the effect of NMES1 overexpression. Furthermore, almost no signal for CIV-associated NDUFA4 was detected in BN PAGE experiments in presence of sqpNMES1 (Figure 16E). Together with the amino acid sequence homology between sqpNMES1, NMES1 and NDUFA4, these data strongly suggest that sqpNMES1 integrates into CIV to displace NDUFA4 from the complex. Intriguingly, sqpNMES1 had no effect on CIV activity in wildtype cells (Figure 16F), but restored CIV activity in NDUFA4 k/o cells (Figure 16G & H). Therefore, sqpNMES1 and NDUFA4 seem to be redundant with regard to CIV activity. Despite this, it is still possible that NMES1 and its homologs affect supercomplex composition, as

proposed by Sorouri *et al.* [232]. Further research is needed to investigate the potential effect of NMES1 and its homologs on mitochondrial supercomplexes. On that note, NDUFA4L2 was originally described to inhibit CI [130]. At that time, NDUFA4 was still believed to be a component of CI and not CIV. However, CI activity may also be affected indirectly by changes in CIV composition due to loss of supercomplexes: As mentioned in chapter 1.5.2, it has been suggested that interactions with CIII and CIV are required to stabilize CI [154]. Thus, the effect of NMES1 on CI activity may be worth investigating, as it may serve as a proxy for supercomplex assembly.

The effect of sqpNMES1 on NMES1 remains elusive, since constitutive expression of NMES1 was rapidly silenced in THP-1 and HEK293T cells (data not shown). As already mentioned, sqpNMES1 almost completely displaced NDUFA4 from CIV (Figure 16E). In contrast, NMES1 overexpression did not result in any detectable changes in CIV-associated NDUFA4 (Figure 10D), and CIV-associated NDUFA4 was still detected in LPS-stimulated MDMs (Figure 10A). Therefore, we speculate that, in contradiction to our initial hypothesis, sqpNMES1 may exhibit higher affinity to CIV than both NMES1 and NDUFA4. However, due to possible differences in expression levels of sqpNMES1 and NMES1, additional experiments are required to investigate whether sqpNMES1 indeed competes with NMES1 for integration into CIV.

Intriguingly, homologs of NMES1 and/or NDUFA4 were, among others, identified in *S. aureus, L. monocytogenes* and *E. faecium*, which are known to be facultative intracellular pathogens [233-235] (Figure 17). However, as already mentioned, cross-contamination of sequencing samples with human DNA cannot be excluded. Furthermore, since, in contrast to viruses, aerobic bacteria encode fully functional electron transport systems [236], it is unclear whether potential bacterial homologs interfere with host cell functions. In fact, this is rather improbable, since bacterial homologs would somehow need to be shuttled into host mitochondria. It is far more likely that in the case of bacteria, homologs of NMES1 and NDUFA4 merely exist to fulfil their metabolic function within their cell of origin.

5.3. The effect of NMES1 and its homologs on pro-inflammatory cytokine release

Our data suggest that NMES1 is a pro-inflammatory protein. More specifically, according to our ELISA data, NMES1 seems to affect early NF-kB responses, since we could only observe an increase in release of TNF, but not IL-6 (Figure 19A & B). This is, again, in contrast with findings by Lee *et al.*, who reported that NMES1 overexpression dampens pro-inflammatory cytokine release [109]. As already mentioned, these differences may be explained by the different cell types used in this study. In contrast, Clayton *et al.* showed that NMES1 expression is increased

in macrophages derived from patients suffering from rheumatoid arthritis or COVID-19 [111]. These findings support the notion that NMES1 indeed exerts a pro-inflammatory function.

Importantly, the cell culture model employed herein is artificial, since NMES1 expression is induced prior to stimulation, whereas under endogenous settings, NMES1 expression is induced downstream of stimulation with TLR ligands (Figure 7). Whether NMES1 expression also affects TNF release in a setting where NMES1 is expressed endogenously remains to be investigated. TNF release was also increased upon overexpression of NDUFA4 (Figure 19A & B). However, overexpression of NDUFA4 is artificial, since in contrast to NMES1, NDUFA4 is constitutively expressed, and expression is not upregulated upon stimulation with TLR ligands in endogenous settings. The effect on TNF release was consistently stronger for NDUFA4 than for NMES1, possibly owing to differences in expression levels and/or stability between the two proteins.

In line with our ELISA data, we also observed a significant increase in TNF mRNA expression upon Pam_3CSK_4 stimulation in THP-1 cells overexpressing NMES1 or NDUFA4 (Figure 20A). Interestingly, differences in expression of TNFAIP3, another early NF-κB target gene, were not statistically significant. Additional experiments are required to test whether NMES1 specifically affects the expression levels of TNF or whether other early NF-κB target genes are also affected. TNF expression has been reported to be regulated post-transcriptionally [237, 238]. Therefore, it remains to be determined whether the increase in mRNA levels is due to an increase in *de novo* transcription or due to an increase in mRNA stability. Of note, TNF shedding presents another possible layer of regulation. So far, we have not investigated whether NMES1 affects this process. As NMES1 localizes to the mitochondria, any effects on TNF shedding would most likely be indirect.

Interestingly, NDUFA4 k/o THP-1 cells did not exhibit any significant changes in TNF or IL-6 release (Figure 19D & E), whereas IL-6 release was significantly decreased in NDUFA4 k/o BLaER2 cells (Figure 21E). This difference may be explained by the fact that the BLaER2 cell line is derived from malignant B cells, and macrophage-specific gene expression is only induced short-term upon transdifferentiation [239]. Overall, these cell line-dependent differences emphasize the importance of additional cell culture models to recapitulate our findings.

Intriguingly, overexpression of sqpNMES1 did not induce an increase in TNF release (Figure 19A). Therefore, viral homologs might have evolved to inhibit the pro-inflammatory effects of NMES1. Further experimental evidence is required to support this hypothesis. For example, as mentioned above, it remains to be analyzed how co-expression of sqpNMES1 affects cytokine release in NMES1-expressing cells. Furthermore, an alanine scan focusing on residues that distinguish NMES1 from sqpNMES1 may allow to pinpoint the residues that

mediate the observed increase in TNF release. Finally, despite the homology of the amino acid sequences of both NMES1 and NDUFA4 between squirrel and human, it is possible that the effects of sqpNMES1 observed herein are different from those in its native host. Moreover, the function of sqpNMES1 may be influenced by other viral factors.

5.4. Looking for a role of NMES1 beyond complex IV activity

In search of a potential role of NMES1 beyond ETC activity, and in order to unravel the molecular mechanism through which NMES1 expression leads to the observed increase in TNF release, we analyzed the interactomes of NMES1 and NDUFA4 by mass spectrometry. The only mitochondrial protein that was significantly and specifically enriched in the NMES1-FLAG co-IP is MPC2 (Figure 22C). Although we could co-immunoprecipitate MPC2 with NMES1 or NDUFA4, and thus were able to recapitulate the results obtained from the LC-MS/MS analysis (Figure 22D), we cannot exclude the possibility that this interaction is non-specific.

Interestingly, we found components of CI to be significantly enriched in the NDUFA4-FLAG co-IP (Figure 22C). This might indicate that in presence of NDUFA4, CIV is more likely to form supercomplexes. In fact, as mentioned above, Sorouri *et al.* hypothesized that NDUFA4 and NMES1 might regulate mitochondrial supercomplex formation, thereby affecting cristae structure, and in consequence, regulating intrinsic apoptosis [232]. However, only few components of CIII were significantly enriched in the NDUFA4-FLAG co-IP, which would argue against such an effect. In addition, BN PAGE experiments showed no clear differences in the band pattern of MTCO1 between any of the conditions tested (Figure 10B, D & E and Figure 16E). Importantly, since we focused on medium molecular weight complexes (including CIV_1 and CIV_2) in our analyses, the BN PAGE experiments shown here do not resolve the different supercomplexes. Therefore, further experiments are required to investigate the potential effect of NMES1 and NDUFA4 on mitochondrial supercomplexes. Together with BN PAGE experiments and in-gel activity assays, CI activity assays may prove useful in this context, since CI stability is dependent on mitochondrial supercomplexes.

In addition to mass spectrometry analyses, we investigated potential changes in the transcriptome upon expression of NMES1 using RNAseq. Overexpression of NMES1 alone only resulted in small changes in the transcriptome and differentially expressed genes were only detected at very late timepoints (Figure 23A & B). Therefore, the effects of NMES1 on the transcriptome appear to be indirect. Furthermore, there was no enrichment of components of a specific pathway or process. Hence, the mechanism through which NMES1 expression leads to an increase in TNF release still remains elusive.

As endogenous expression of NMES1 is induced downstream of TLR signaling, it is conceivable that the effect of NMES1 is stimulation-dependent. We performed experiments to investigate this possibility. However, the experimental design was not ideal, since the response of THP-1 cells to R848 stimulation varied greatly between experiments (Figure 19A). Furthermore, TNF release induced was much higher and more robust upon stimulation with Pam_3CSK_4. In order to determine whether NMES1 overexpression results in stimulation-dependent changes in the transcriptome, the experiment should therefore be repeated using Pam_3CSK_4 stimulation.

5.5. Conclusions

Taken together, our data suggest that NMES1 plays a pro-inflammatory role in macrophages. However, the NMES1-dependent increase in TNF release was only moderate and not significant. Hence, the relevance of this effect *in vivo* remains to be determined. We are currently unable to provide a mechanism through which NMES1 expression leads to the observed increased in TNF release. On one hand, we could not identify any processes beyond the electron transport chain that NMES1 may be involved in. On the other hand, NMES1 and NDUFA4 seem to be redundant with regard to electron transport chain activity. Therefore, it is conceivable that the role of NMES1 lies in finetuning electron transport chain activity, and, as previously proposed by Sorouri *et al*. [232], modulating supercomplex composition. There is still much debate concerning the function of mitochondrial supercomplexes, and additional research in this field is required to elucidate the potential role of NMES1. In addition, metabolomics experiments may provide further insights into the function of NMES1.

Due to the dysregulation of metabolism in cancer cells and the adaptation of cellular metabolism to cell culture conditions, cell line models may not be ideal to investigate the function of NMES1. In particular, the absence of NMES1 expression in all of the monocyte-like cell lines tested herein raises the question whether all components acting up- and downstream of NMES1 are indeed expressed in these cells. To clarify the role of NMES1, loss-of-function studies complementing our data would be of particular interest.

Ultimately, the immune response is a complex process that requires the interplay between various different cell types. Therefore, it would be interesting to study the effects of loss of NMES1 expression in a mouse model *in vivo*. Finally, it remains to be investigated whether NMES1 affects other effector functions of macrophages, such as phagocytosis.

6. SUMMARY

NMES1 expression is strongly induced in macrophages upon LPS stimulation, and NMES1 was recently identified as a component of complex IV of the electron transport chain. The exact function of NMES1, however, remains unknown. NMES1 exhibits structural homology to NDUFA4, a component of complex IV, and sequence homology to NDUFA4L2, a hypoxia-inducible protein which was shown to inhibit complex I activity. Hence, we initially hypothesized that NMES1 might be a NF-κB-inducible negative regulator of the electron transport chain. The aim of this thesis was to elucidate the role of NMES1 in the innate immune response.

Genome editing itself affected electron transport chain activity and cytokine release in monocyte-derived macrophages. Moreover, we could not identify a monocyte-like cell line that endogenously expresses NMES1, and CRISPR activation only induced low levels of NMES1 expression in THP-1 cells. Hence, overexpression models were used for most experiments. The lack of a suitable cell culture model where NMES1 is expressed endogenously is a major limitation of this study.

Expression of either NMES1 or NDUFA4 was sufficient to restore complex IV activity in NDUFA4-deficient THP-1 cells. Thus, NMES1 and NDUFA4 seem to be redundant with regard to complex IV activity. Furthermore, we found that overexpression of NMES1 results in a two-fold, but non-significant increase in TNF release upon stimulation with TLR ligands. This suggests that NMES1 plays a pro-inflammatory role in macrophages. We are currently unable to provide a mechanism through which NMES1 exerts this pro-inflammatory function.

Interestingly, the squirrel pox homolog of NMES1 almost completely displaced NDUFA4 from complex IV when overexpressed in HEK293T cells. This *de facto* substitution had no effect on complex IV activity. In contrast to NMES1, over-expression of the squirrel pox homolog in THP-1 cells did not result in an increase in TNF release. Hence, viral homologs of NMES1 may have evolved to dampen antiviral responses. Additional data are required to support this hypothesis.

Proteomics and RNAseq experiments did not reveal any process other than the electron transport chain that NMES1 might be involved in: While we were able to identify and validate an interaction between NMES1 and MPC2, this interaction is possibly non-specific. Differences between the interactomes of NMES1 and NDUFA4 suggest that NDUFA4-containing complex IV may be more likely to form supercomplexes. However, further experiments required to support these findings.

Taken together, the function of NMES1 still remains elusive. The observed increase in TNF release was only moderate, and the relevance of this effect *in vivo* is yet to be determined. Ultimately, loss-of-function studies using cells that endogenously express NMES1 – possibly iPSC-derived macrophages – or an NMES1 knock-out mouse model may provide further insights into the function of NMES1.

7. REFERENCES

1. Slavik, K.M. and P.J. Kranzusch, *CBASS to cGAS-STING: The Origins and Mechanisms of Nucleotide Second Messenger Immune Signaling.* Annual Review of Virology, 2023. **10**(1): p. 423-453.

2. Rankin, L.C. and D. Artis, *Beyond Host Defense: Emerging Functions of the Immune System in Regulating Complex Tissue Physiology.* Cell, 2018. **173**(3): p. 554-567.

3. Medzhitov, R., *The spectrum of inflammatory responses.* Science, 2021. **374**(6571): p. 1070-1075.

4. Murphy, K. and C. Weaver, in *Janeway's Immunobiology.* 2017, Garland Science: New York, NY. Chapter 1, p. 1-36.

5. Murphy, K. and C. Weaver, in *Janeway's Immunobiology.* 2017, Garland Science: New York, NY. Chapter 2, p. 37-76.

6. Murphy, K. and C. Weaver, in *Janeway's Immunobiology.* 2017, Garland Science: New York, NY. Chapter 4, p. 139-172.

7. Murphy, K. and C. Weaver, in *Janeway's Immunobiology.* 2017, Garland Science: New York, NY. Chapter 9, p. 345-398.

8. Palm, N.W. and R. Medzhitov, *Pattern recognition receptors and control of adaptive immunity.* Immunol Rev, 2009. **227**(1): p. 221-33.

9. Murphy, K. and C. Weaver, in *Janeway's Immunobiology.* 2017, Garland Science: New York, NY. Chapter 3, p. 77-137.

10. Murphy, K. and C. Weaver, in *Janeway's Immunobiology.* 2017, Garland Science: New York, NY. Chapter 5, p. 173-212.

11. Netea, M.G., et al., *Trained immunity: A program of innate immune memory in health and disease.* Science, 2016. **352**(6284).

12. Murphy, K. and C. Weaver, in *Janeway's Immunobiology.* 2017, Garland Science: New York, NY. Chapter 13, p. 533-600.

13. Murphy, K. and C. Weaver, in *Janeway's Immunobiology.* 2017, Garland Science: New York, NY. Chapter 15, p. 643-700.

14. Lopes Fischer, N., et al., *Effector-triggered immunity and pathogen sensing in metazoans.* Nature Microbiology, 2020. **5**(1): p. 14-26.

15. Brubaker, S.W., et al., *Innate Immune Pattern Recognition: A Cell Biological Perspective.* Annual Review of Immunology, 2015. **33**(1): p. 257-290.

16. Sun, L., et al., *Cyclic GMP-AMP synthase is a cytosolic DNA sensor that activates the type I interferon pathway.* Science, 2013. **339**(6121): p. 786-91.

17. Hornung, V., et al., *OAS proteins and cGAS: unifying concepts in sensing and responding to cytosolic nucleic acids.* Nature Reviews Immunology, 2014. **14**(8): p. 521-528.

18. Schroder, K. and J. Tschopp, *The inflammasomes.* Cell, 2010. **140**(6): p. 821-32.

19. Nagashima, H., et al., *Toll-like Receptor 10 in Helicobacter pylori Infection.* J Infect Dis, 2015. **212**(10): p. 1666-76.

20. Oosting, M., et al., *Human TLR10 is an anti-inflammatory pattern-recognition receptor.* Proc Natl Acad Sci U S A, 2014. **111**(42): p. E4478-84.

21. Pohar, J., et al., *The Role of UNC93B1 Protein in Surface Localization of TLR3 Receptor and in Cell Priming to Nucleic Acid Agonists*.* Journal of Biological Chemistry, 2013. **288**(1): p. 442-454.

22.   Lind, N.A., et al., *Regulation of the nucleic acid-sensing Toll-like receptors.* Nature Reviews Immunology, 2022. **22**(4): p. 224-235.

23.   Miyake, K., *Innate immune sensing of pathogens and danger signals by cell surface Toll-like receptors.* Seminars in Immunology, 2007. **19**(1): p. 3-10.

24.   Motshwene, P.G., et al., *An oligomeric signaling platform formed by the Toll-like receptor signal transducers MyD88 and IRAK-4.* J Biol Chem, 2009. **284**(37): p. 25404-11.

25.   Sun, J., et al., *Comprehensive RNAi-based screening of human and mouse TLR pathways identifies species-specific preferences in signaling protein use.* Sci Signal, 2016. **9**(409).

26.   Fitzgerald, K.A. and J.C. Kagan, *Toll-like Receptors and the Control of Immunity.* Cell, 2020. **180**(6): p. 1044-1066.

27.   van Uden, P., N.S. Kenneth, and S. Rocha, *Regulation of hypoxia-inducible factor-1alpha by NF-kappaB.* Biochem J, 2008. **412**(3): p. 477-84.

28.   Wang, T., et al., *HIF1α-Induced Glycolysis Metabolism Is Essential to the Activation of Inflammatory Macrophages.* Mediators of inflammation, 2017. **2017**: p. 9029327-9029327.

29.   Honda, K., et al., *IRF-7 is the master regulator of type-I interferon-dependent immune responses.* Nature, 2005. **434**(7034): p. 772-777.

30.   Honda, K., et al., *Spatiotemporal regulation of MyD88-IRF-7 signalling for robust type-I interferon induction.* Nature, 2005. **434**(7036): p. 1035-40.

31.   Honda, K., et al., *Role of a transductional-transcriptional processor complex involving MyD88 and IRF-7 in Toll-like receptor signaling.* Proc Natl Acad Sci U S A, 2004. **101**(43): p. 15416-21.

32.   Kim, T.W., et al., *A critical role for IRAK4 kinase activity in Toll-like receptor-mediated innate immunity.* J Exp Med, 2007. **204**(5): p. 1025-36.

33.   Uematsu, S., et al., *Interleukin-1 receptor-associated kinase-1 plays an essential role for Toll-like receptor (TLR)7- and TLR9-mediated interferon-alpha induction.* J Exp Med, 2005. **201**(6): p. 915-23.

34.   Takaoka, A., et al., *Integral role of IRF-5 in the gene induction programme activated by Toll-like receptors.* Nature, 2005. **434**(7030): p. 243-9.

35.   Heinz, L.X., et al., *TASL is the SLC15A4-associated adaptor for IRF5 activation by TLR7-9.* Nature, 2020. **581**(7808): p. 316-322.

36.   Liu, S., et al., *Phosphorylation of innate immune adaptor proteins MAVS, STING, and TRIF induces IRF3 activation.* Science, 2015. **347**(6227): p. aaa2630.

37.   Cusson-Hermance, N., et al., *Rip1 Mediates the Trif-dependent Toll-like Receptor 3- and 4-induced NF-kB Activation but Does Not Contribute to Interferon Regulatory Factor 3 Activation.* Journal of Biological Chemistry, 2005. **280**(44): p. 36560-36566.

38.   Tanimura, N., et al., *Roles for LPS-dependent interaction and relocation of TLR4 and TRAM in TRIF-signaling.* Biochem Biophys Res Commun, 2008. **368**(1): p. 94-9.

39.   Kagan, J.C., et al., *TRAM couples endocytosis of Toll-like receptor 4 to the induction of interferon-beta.* Nat Immunol, 2008. **9**(4): p. 361-8.

40.   Zanoni, I., et al., *CD14 controls the LPS-induced endocytosis of Toll-like receptor 4.* Cell, 2011. **147**(4): p. 868-80.

41.   Brown, G.D., J.A. Willment, and L. Whitehead, *C-type lectins in immunity and homeostasis.* Nature Reviews Immunology, 2018. **18**(6): p. 374-389.

42.   van Asbeck, E.C., et al., *Mannose binding lectin plays a crucial role in innate immunity against yeast by enhanced complement activation and enhanced uptake of polymorphonuclear cells.* BMC Microbiology, 2008. **8**(1): p. 229.

43.   Nauta, A.J., et al., *Mannose-binding lectin engagement with late apoptotic and necrotic cells.* Eur J Immunol, 2003. **33**(10): p. 2853-63.

44.   Chou, W.-C., et al., *The NLR gene family: from discovery to present day.* Nature Reviews Immunology, 2023. **23**(10): p. 635-654.

45.   Heim, V.J., C.A. Stafford, and U. Nachbur, *NOD Signaling and Cell Death.* Frontiers in Cell and Developmental Biology, 2019. **7**.

46.   Laroui, H., et al., *L-Ala-γ-D-Glu-meso-diaminopimelic acid (DAP) interacts directly with leucine-rich region domain of nucleotide-binding oligomerization domain 1, increasing phosphorylation activity of receptor-interacting serine/threonine-protein kinase 2 and its interaction with nucleotide-binding oligomerization domain 1.* J Biol Chem, 2011. **286**(35): p. 31003-31013.

47.   Grimes, C.L., et al., *The innate immune protein Nod2 binds directly to MDP, a bacterial cell wall fragment.* J Am Chem Soc, 2012. **134**(33): p. 13535-7.

48.   Fernández Daniel, J. and M. Lamkanfi, *Inflammatory caspases: key regulators of inflammation and cell death*, in *Biological Chemistry*. 2015. p. 193.

49.   Broz, P. and V.M. Dixit, *Inflammasomes: mechanism of assembly, regulation and signalling.* Nature Reviews Immunology, 2016. **16**(7): p. 407-420.

50.   Martinon, F., K. Burns, and J. Tschopp, *The inflammasome: a molecular platform triggering activation of inflammatory caspases and processing of proIL-beta.* Mol Cell, 2002. **10**(2): p. 417-26.

51.   Johnson, D.C., et al., *DPP8/DPP9 inhibitor-induced pyroptosis for treatment of acute myeloid leukemia.* Nat Med, 2018. **24**(8): p. 1151-1156.

52.   Rehwinkel, J. and M.U. Gack, *RIG-I-like receptors: their regulation and roles in RNA sensing.* Nature Reviews Immunology, 2020. **20**(9): p. 537-551.

53.   Kowalinski, E., et al., *Structural Basis for the Activation of Innate Immune Pattern-Recognition Receptor RIG-I by Viral RNA.* Cell, 2011. **147**(2): p. 423-435.

54.   Luo, D., et al., *Structural insights into RNA recognition by RIG-I.* Cell, 2011. **147**(2): p. 409-22.

55.   Cui, S., et al., *The C-Terminal Regulatory Domain Is the RNA 5'-Triphosphate Sensor of RIG-I.* Molecular Cell, 2008. **29**(2): p. 169-179.

56.   Goubau, D., et al., *Antiviral immunity via RIG-I-mediated recognition of RNA bearing 5'-diphosphates.* Nature, 2014. **514**(7522): p. 372-375.

57.   Hornung, V., et al., *5'-Triphosphate RNA is the ligand for RIG-I.* Science, 2006. **314**(5801): p. 994-7.

58.   Peisley, A., et al., *RIG-I forms signaling-competent filaments in an ATP-dependent, ubiquitin-independent manner.* Mol Cell, 2013. **51**(5): p. 573-83.

59.   Gack, M.U., et al., *TRIM25 RING-finger E3 ubiquitin ligase is essential for RIG-I-mediated antiviral activity.* Nature, 2007. **446**(7138): p. 916-920.

60.   Wu, B. and S. Hur, *How RIG-I like receptors activate MAVS.* Curr Opin Virol, 2015. **12**: p. 91-8.

61.   Zeng, W., et al., *Reconstitution of the RIG-I pathway reveals a signaling role of unanchored polyubiquitin chains in innate immunity.* Cell, 2010. **141**(2): p. 315-30.

62.   Hou, F., et al., *MAVS forms functional prion-like aggregates to activate and propagate antiviral innate immune response.* Cell, 2011. **146**(3): p. 448-61.

63.   Seth, R.B., et al., *Identification and Characterization of MAVS, a Mitochondrial Antiviral Signaling Protein that Activates NF-κB and IRF3.* Cell, 2005. **122**(5): p. 669-682.

64.   Li, X., et al., *Structural basis of double-stranded RNA recognition by the RIG-I like receptor MDA5.* Archives of Biochemistry and Biophysics, 2009. **488**(1): p. 23-33.

65.   Kato, H., et al., *Length-dependent recognition of double-stranded ribonucleic acids by retinoic acid-inducible gene-I and melanoma differentiation-associated gene 5.* J Exp Med, 2008. **205**(7): p. 1601-10.

66.   Yu, Q., K. Qu, and Y. Modis, *Cryo-EM Structures of MDA5-dsRNA Filaments at Different Stages of ATP Hydrolysis.* Mol Cell, 2018. **72**(6): p. 999-1012.e6.

67.   Wu, B., et al., *Structural basis for dsRNA recognition, filament formation, and antiviral signal activation by MDA5.* Cell, 2013. **152**(1-2): p. 276-89.

68.   Berke, I.C. and Y. Modis, *MDA5 cooperatively forms dimers and ATP-sensitive filaments upon binding double-stranded RNA.* Embo j, 2012. **31**(7): p. 1714-26.

69.   Kranzusch, Philip J., et al., *Structure of Human cGAS Reveals a Conserved Family of Second-Messenger Enzymes in Innate Immunity.* Cell Reports, 2013. **3**(5): p. 1362-1368.

70.   Rebouillat, D., I. Marié, and A.G. Hovanessian, *Molecular cloning and characterization of two related and interferon-induced 56-kDa and 30-kDa proteins highly similar to 2'-5' oligoadenylate synthetase.* European Journal of Biochemistry, 1998. **257**(2): p. 319-330.

71.   Hur, S., *Double-Stranded RNA Sensors and Modulators in Innate Immunity.* Annu Rev Immunol, 2019. **37**: p. 349-375.

72.   Wang, Y., et al., *Length dependent activation of OAS proteins by dsRNA.* Cytokine, 2020. **126**: p. 154867.

73.   Rex, V., et al., *The two faces of oligoadenylate synthetase-like: effective antiviral protein and negative regulator of innate immunity.* Current Opinion in Virology, 2023. **60**: p. 101329.

74.   Ghosh, A., et al., *Oligoadenylate-Synthetase-Family Protein OASL Inhibits Activity of the DNA Sensor cGAS during DNA Virus Infection to Limit Interferon Production.* Immunity, 2019. **50**(1): p. 51-63.e5.

75.   Zhu, J., et al., *Antiviral Activity of Human OASL Protein Is Mediated by Enhancing Signaling of the RIG-I RNA Sensor.* Immunity, 2014. **40**(6): p. 936-948.

76.   Hartmann, R., et al., *p59OASL, a 2'–5' oligoadenylate synthetase like protein: a novel human gene related to the 2'–5' oligoadenylate synthetase family.* Nucleic acids research, 1998. **26**(18): p. 4121-4127.

77.   Zhang, X., et al., *The cytosolic DNA sensor cGAS forms an oligomeric complex with DNA and undergoes switch-like conformational changes in the activation loop.* Cell Rep, 2014. **6**(3): p. 421-30.

78.   Hopfner, K.-P. and V. Hornung, *Molecular mechanisms and cellular functions of cGAS–STING signalling.* Nature Reviews Molecular Cell Biology, 2020. **21**(9): p. 501-521.

79.   Dostert, C., et al., *The TNF Family of Ligands and Receptors: Communication Modules in the Immune System and Beyond.* Physiological Reviews, 2019. **99**(1): p. 115-160.

80. Black, R.A., et al., *A metalloproteinase disintegrin that releases tumour-necrosis factor-alpha from cells.* Nature, 1997. **385**(6618): p. 729-33.

81. Hofmann, S., et al., *The tumour necrosis factor-alpha induced vascular permeability is associated with a reduction of VE-cadherin expression.* European journal of medical research, 2002. **7**(4): p. 171-176.

82. Murphy, K. and C. Weaver, in *Janeway's Immmunobiology*. 2017, Garland Science: New York, NY. Chapter 11, p. 445-491.

83. Murphy, K. and C. Weaver, in *Janeway's Immunobiology*. 2017, Garland Science: New York, NY. Chapter 12, p. 493-531.

84. Hirano, T., *IL-6 in inflammation, autoimmunity and cancer.* International Immunology, 2020. **33**(3): p. 127-148.

85. Wang, X., et al., *Structural biology of shared cytokine receptors.* Annu Rev Immunol, 2009. **27**: p. 29-60.

86. Dinarello, C.A., *Overview of the IL-1 family in innate inflammation and acquired immunity.* Immunol Rev, 2018. **281**(1): p. 8-27.

87. Arango Duque, G. and A. Descoteaux, *Macrophage Cytokines: Involvement in Immunity and Infectious Diseases.* Frontiers in Immunology, 2014. **5**.

88. Bastian, D., et al., *The IL-12 Cytokine and Receptor Family in Graft-vs.-Host Disease.* Frontiers in Immunology, 2019. **10**.

89. Stern, A.S., et al., *Purification to homogeneity and partial characterization of cytotoxic lymphocyte maturation factor from human B-lymphoblastoid cells.* Proc Natl Acad Sci U S A, 1990. **87**(17): p. 6808-12.

90. Hard, G.C., *Some biochemical aspects of the immune macrophage.* British journal of experimental pathology, 1970. **51**(1): p. 97-105.

91. Mills, C.D., et al., *M-1/M-2 Macrophages and the Th1/Th2 Paradigm.* The Journal of Immunology, 2000. **164**(12): p. 6166.

92. Nathan, C.F., et al., *Identification of interferon-gamma as the lymphokine that activates human macrophage oxidative metabolism and antimicrobial activity.* The Journal of Experimental Medicine, 1983. **158**(3): p. 670-689.

93. Stein, M., et al., *Interleukin 4 potently enhances murine macrophage mannose receptor activity: a marker of alternative immunologic macrophage activation.* The Journal of Experimental Medicine, 1992. **176**(1): p. 287-292.

94. Biswas, S.K. and A. Mantovani, *Macrophage plasticity and interaction with lymphocyte subsets: cancer as a paradigm.* Nature Immunology, 2010. **11**(10): p. 889-896.

95. Viola, A., et al., *The Metabolic Signature of Macrophage Responses.* Frontiers in Immunology, 2019. **10**(1462).

96. Rodríguez-Prados, J.-C., et al., *Substrate Fate in Activated Macrophages: A Comparison between Innate, Classic, and Alternative Activation.* The Journal of Immunology, 2010. **185**(1): p. 605-614.

97. Ojaniemi, M., et al., *Phosphatidylinositol 3-kinase is involved in Toll-like receptor 4-mediated cytokine expression in mouse macrophages.* Eur J Immunol, 2003. **33**(3): p. 597-605.

98. Peyssonnaux, C., et al., *Cutting edge: Essential role of hypoxia inducible factor-1alpha in development of lipopolysaccharide-induced sepsis.* J Immunol, 2007. **178**(12): p. 7516-9.

99. Palsson-McDermott, E.M. and L.A. O'Neill, *The Warburg effect then and now: from cancer to inflammatory diseases.* Bioessays, 2013. **35**(11): p. 965-73.

100.   Freemerman, A.J., et al., *Metabolic reprogramming of macrophages: glucose transporter 1 (GLUT1)-mediated glucose metabolism drives a proinflammatory phenotype.* J Biol Chem, 2014. **289**(11): p. 7884-96.

101.   Kelly, B. and L.A.J. O'Neill, *Metabolic reprogramming in macrophages and dendritic cells in innate immunity.* Cell Research, 2015. **25**(7): p. 771-784.

102.   Altschul, S.F., et al., *Gapped BLAST and PSI-BLAST: a new generation of protein database search programs.* Nucleic Acids Res, 1997. **25**(17): p. 3389-402.

103.   Altschul, S.F., et al., *Protein database searches using compositionally adjusted substitution matrices.* Febs j, 2005. **272**(20): p. 5101-9.

104.   Lattin, J.E., et al., *Expression analysis of G Protein-Coupled Receptors in mouse macrophages.* Immunome Res, 2008. **4**: p. 5.

105.   Wu, C., et al., *BioGPS: an extensible and customizable portal for querying and organizing gene annotation resources.* Genome Biol, 2009. **10**(11): p. R130.

106.   Rieckmann, J.C., et al., *Social network architecture of human immune cells unveiled by quantitative proteomics.* Nat Immunol, 2017. **18**(5): p. 583-593.

107.   Obayashi, T., et al., *COXPRESdb v7: a gene coexpression database for 11 animal species supported by 23 coexpression platforms for technical evaluation and evolutionary inference.* Nucleic Acids Research, 2019. **47**(D1): p. D55-D62.

108.   Liu, G., et al., *miR-147, a microRNA that is induced upon Toll-like receptor stimulation, regulates murine macrophage inflammatory responses.* Proc Natl Acad Sci U S A, 2009. **106**(37): p. 15819-15824.

109.   Lee, C.Q.E., et al., *Coding and non-coding roles of MOCCI (C15ORF48) coordinate to regulate host inflammation and immunity.* Nature Communications, 2021. **12**(1): p. 2130.

110.   Sorouri, M., et al., *Signatures of host-pathogen evolutionary conflict reveal MISTR-A conserved MItochondrial STress Response network.* PLoS Biol, 2020. **18**(12): p. e3001045.

111.   Clayton, S.A., et al., *Inflammation causes remodeling of mitochondrial cytochrome c oxidase mediated by the bifunctional gene C15orf48.* Sci Adv, 2021. **7**(50): p. eabl5182.

112.   Tong, A.J., et al., *A Stringent Systems Approach Uncovers Gene-Specific Mechanisms Regulating Inflammation.* Cell, 2016. **165**(1): p. 165-179.

113.   Zhou, J., et al., *A novel gene, NMES1, downregulated in human esophageal squamous cell carcinoma.* Int J Cancer, 2002. **101**(4): p. 311-6.

114.   Spisák, S., et al., *Genome-wide screening of genes regulated by DNA methylation in colon cancer development.* PLoS One, 2012. **7**(10): p. e46215.

115.   Uhlén, M., et al., *Proteomics. Tissue-based map of the human proteome.* Science, 2015. **347**(6220): p. 1260419.

116.   Human Protein Atlas. *C15orf48 Tissue Expression Data*. 2020. [cited 12.10.2020]; Available from: https://www.proteinatlas.org/ENSG00000166920-C15orf48/tissue.

117.   Karlsson, M., et al., *A single–cell type transcriptomics map of human tissues.* Science Advances, 2021. **7**(31): p. eabh2169.

118.   Human Protein Atlas. *C15orf48 Single Cell Expression Data*. 2021. [cited 23.11.2023]; Available from:

https://www.proteinatlas.org/ENSG00000166920-C15orf48/single+cell+type.

119.   Arai, M., et al., *Analysis of the methylation status of genes up-regulated by the demethylating agent, 5-aza-2'-deoxycytidine, in esophageal squamous cell carcinoma.* Oncol Rep, 2008. **20**(2): p. 405-12.

120.   Endou, M., et al., *Coxfa4l3, a novel mitochondrial electron transport chain Complex 4 subunit protein, switches from Coxfa4 during spermatogenesis.* Mitochondrion, 2020. **52**: p. 1-7.

121.   Floyd, B.J., et al., *Mitochondrial Protein Interaction Mapping Identifies Regulators of Respiratory Chain Function.* Molecular cell, 2016. **63**(4): p. 621-632.

122.   Söding, J., A. Biegert, and A.N. Lupas, *The HHpred interactive server for protein homology detection and structure prediction.* Nucleic Acids Res, 2005. **33**(Web Server issue): p. W244-8.

123.   Zimmermann, L., et al., *A Completely Reimplemented MPI Bioinformatics Toolkit with a New HHpred Server at its Core.* Journal of Molecular Biology, 2018. **430**(15): p. 2237-2243.

124.   Gabler, F., et al., *Protein Sequence Analysis Using the MPI Bioinformatics Toolkit.* Current Protocols in Bioinformatics, 2020. **72**(1): p. e108.

125.   Jumper, J., et al., *Highly accurate protein structure prediction with AlphaFold.* Nature, 2021. **596**(7873): p. 583-589.

126.   Varadi, M., et al., *AlphaFold Protein Structure Database: massively expanding the structural coverage of protein-sequence space with high-accuracy models.* Nucleic Acids Research, 2021. **50**(D1): p. D439-D444.

127.   Hirst, J., et al., *The nuclear encoded subunits of complex I from bovine heart mitochondria.* Biochimica et Biophysica Acta (BBA) - Bioenergetics, 2003. **1604**(3): p. 135-150.

128.   Zong, S., et al., *Structure of the intact 14-subunit human cytochrome c oxidase.* Cell Res, 2018. **28**(10): p. 1026-1034.

129.   Balsa, E., et al., *NDUFA4 is a subunit of complex IV of the mammalian electron transport chain.* Cell Metab, 2012. **16**(3): p. 378-86.

130.   Tello, D., et al., *Induction of the mitochondrial NDUFA4L2 protein by HIF-1alpha decreases oxygen consumption by inhibiting Complex I activity.* Cell Metab, 2011. **14**(6): p. 768-79.

131.   Sanmarco, L.M., et al., *Lactate limits CNS autoimmunity by stabilizing HIF-1α in dendritic cells.* Nature, 2023. **620**(7975): p. 881-889.

132.   Agarwal, V., et al., *Predicting effective microRNA target sites in mammalian mRNAs.* Elife, 2015. **4**.

133.   Cui, S., et al., *LncRNA MAFG-AS1 promotes the progression of colorectal cancer by sponging miR-147b and activation of NDUFA4.* Biochem Biophys Res Commun, 2018. **506**(1): p. 251-258.

134.   Zhang, W.C., et al., *miR-147b-mediated TCA cycle dysfunction and pseudohypoxia initiate drug tolerance to EGFR inhibitors in lung adenocarcinoma.* Nature Metabolism, 2019. **1**(4): p. 460-474.

135.   McGeary, S.E., et al., *The biochemical basis of microRNA targeting efficacy.* Science, 2019. **366**(6472).

136.   Martier, R. and P. Konstantinova, *Gene Therapy for Neurodegenerative Diseases: Slowing Down the Ticking Clock.* Front Neurosci, 2020. **14**: p. 580179.

137. Li, C., et al., *The prognostic and immune significance of C15orf48 in pan-cancer and its relationship with proliferation and apoptosis of thyroid carcinoma.* Front Immunol, 2023. **14**: p. 1131870.

138. Wen, S., et al., *Four differentially expressed genes can predict prognosis and microenvironment immune infiltration in lung cancer: a study based on data from the GEO.* BMC Cancer, 2022. **22**(1): p. 193.

139. Zhao, R.Z., et al., *Mitochondrial electron transport chain, ROS generation and uncoupling (Review).* Int J Mol Med, 2019. **44**(1): p. 3-15.

140. Kobayashi, A., et al., *Roles of Noncoding RNAs in Regulation of Mitochondrial Electron Transport Chain and Oxidative Phosphorylation.* Int J Mol Sci, 2023. **24**(11).

141. Sirey, T.M. and C.P. Ponting, *Insights into the post-transcriptional regulation of the mitochondrial electron transport chain.* Biochem Soc Trans, 2016. **44**(5): p. 1491-1498.

142. Vogel , F., et al., *Dynamic subcompartmentalization of the mitochondrial inner membrane.* Journal of Cell Biology, 2006. **175**(2): p. 237-247.

143. Gilkerson, R.W., J.M.L. Selker, and R.A. Capaldi, *The cristal membrane of mitochondria is the principal site of oxidative phosphorylation.* FEBS Letters, 2003. **546**(2): p. 355-358.

144. Davies, K.M., et al., *Macromolecular organization of ATP synthase and complex I in whole mitochondria.* Proc Natl Acad Sci U S A, 2011. **108**(34): p. 14121-6.

145. Strauss, M., et al., *Dimer ribbons of ATP synthase shape the inner mitochondrial membrane.* Embo j, 2008. **27**(7): p. 1154-60.

146. Sinkler, C.A., et al., *Tissue- and Condition-Specific Isoforms of Mammalian Cytochrome c Oxidase Subunits: From Function to Human Disease.* Oxid Med Cell Longev, 2017. **2017**: p. 1534056.

147. Chicherin, I.V., et al., *Cytochrome c Oxidase on the Crossroads of Transcriptional Regulation and Bioenergetics.* Front Physiol, 2019. **10**: p. 644.

148. Shinzawa-Itoh, K., et al., *Monomeric structure of an active form of bovine cytochrome c oxidase.* Proceedings of the National Academy of Sciences of the United States of America, 2019. **116**(40): p. 19945-19951.

149. Schägger, H. and K. Pfeiffer, *Supercomplexes in the respiratory chains of yeast and mammalian mitochondria.* Embo j, 2000. **19**(8): p. 1777-83.

150. Jha, P., X. Wang, and J. Auwerx, *Analysis of Mitochondrial Respiratory Chain Supercomplexes Using Blue Native Polyacrylamide Gel Electrophoresis (BN-PAGE).* Current protocols in mouse biology, 2016. **6**(1): p. 1-14.

151. Schon, E.A. and N.A. Dencher, *Heavy breathing: energy conversion by mitochondrial respiratory supercomplexes.* Cell Metab, 2009. **9**(1): p. 1-3.

152. Cogliati, S., et al., *Mechanism of super-assembly of respiratory complexes III and IV.* Nature, 2016. **539**(7630): p. 579-582.

153. Cogliati, S., et al., *Mitochondrial Cristae Shape Determines Respiratory Chain Supercomplexes Assembly and Respiratory Efficiency.* Cell, 2013. **155**(1): p. 160-171.

154. Schägger, H. and K. Pfeiffer, *The Ratio of Oxidative Phosphorylation Complexes I-V in Bovine Heart Mitochondria and the Composition of Respiratory Chain Supercomplexes.* Journal of Biological Chemistry, 2001. **276**(41): p. 37861-37867.

155.   Fedor, J.G. and J. Hirst, *Mitochondrial Supercomplexes Do Not Enhance Catalysis by Quinone Channeling.* Cell Metab, 2018. **28**(3): p. 525-531.e4.
156.   Blaza, J.N., et al., *Kinetic evidence against partitioning of the ubiquinone pool and the catalytic relevance of respiratory-chain supercomplexes.* Proc Natl Acad Sci U S A, 2014. **111**(44): p. 15735-40.
157.   Berndtsson, J., et al., *Respiratory supercomplexes enhance electron transport by decreasing cytochrome c diffusion distance.* EMBO reports, 2020. **21**(12): p. e51015.
158.   Maranzana, E., et al., *Mitochondrial respiratory supercomplex association limits production of reactive oxygen species from complex I.* Antioxid Redox Signal, 2013. **19**(13): p. 1469-80.
159.   Lopez-Fabuel, I., et al., *Complex I assembly into supercomplexes determines differential mitochondrial ROS production in neurons and astrocytes.* Proc Natl Acad Sci U S A, 2016. **113**(46): p. 13063-13068.
160.   Kohler, A., et al., *The functional significance of mitochondrial respiratory chain supercomplexes.* EMBO reports, 2023. **24**(11): p. e57092.
161.   Turrens, J.F., *Mitochondrial formation of reactive oxygen species.* The Journal of physiology, 2003. **552**(Pt 2): p. 335-344.
162.   Murphy, M.P., *How mitochondria produce reactive oxygen species.* The Biochemical journal, 2009. **417**(1): p. 1-13.
163.   West, A.P., et al., *TLR signalling augments macrophage bactericidal activity through mitochondrial ROS.* Nature, 2011. **472**(7344): p. 476-480.
164.   Mills, E.L., et al., *Succinate Dehydrogenase Supports Metabolic Repurposing of Mitochondria to Drive Inflammatory Macrophages.* Cell, 2016. **167**(2): p. 457-470.e13.
165.   Wright, J.J., et al., *Reverse Electron Transfer by Respiratory Complex I Catalyzed in a Modular Proteoliposome System.* Journal of the American Chemical Society, 2022. **144**(15): p. 6791-6801.
166.   Mogilenko, D.A., et al., *Metabolic and Innate Immune Cues Merge into a Specific Inflammatory Response via the UPR.* Cell, 2019. **177**(5): p. 1201-1216.e19.
167.   Wang, Y., et al., *Mitochondrial ROS promote macrophage pyroptosis by inducing GSDMD oxidation.* J Mol Cell Biol, 2019. **11**(12): p. 1069-1082.
168.   Li, X., et al., *Targeting mitochondrial reactive oxygen species as novel therapy for inflammatory diseases and cancers.* Journal of Hematology & Oncology, 2013. **6**(1): p. 19.
169.   Finkel, T., *Signal transduction by mitochondrial oxidants.* J Biol Chem, 2012. **287**(7): p. 4434-40.
170.   *CD14 MicroBeads human*. Miltenyi Biotec, Bergisch Gladbach, Germany, 2020. accessed: 21.09.2023.[online]. Available at: https://static.miltenyibiotec.com/asset/150655405641/document_2evdm6e7jp7up842efgqdklc1c?content-disposition=inline
171.   *Pan Monocyte Isolation Kit human*. Miltenyi Biotec, Bergisch Gladbach, 2022. accessed: 21.09.2023.[online]. Available at: http://www.ulab360.com/files/prod/manuals/201611/17/598265001.pdf
172.   *QIAquick® Spin Handbook*. Qiagen, Venlo, Netherlands, 2020. accessed: 04.10.2023.[online]. Available at: https://www.qiagen.com/us/resources/resourcedetail?id=95f10677-aa29-453d-a222-0e19f01ebe17&lang=en

173.   Synthego. *CRISPR design tool*. 2023. [cited 04.10.2023]; Available from: https://www.synthego.com/products/bioinformatics/crispr-design-tool.

174.   Integrated DNA Technologies Inc. *Custom Alt-R™ CRISPR-Cas9 guide RNA*. 2023. [cited 04.10.2023]; Available from: https://eu.idtdna.com/site/order/designtool/index/CRISPR_CUSTOM.

175.   Benchling. *Benchling*. 2023. [cited 04.10.2023]; Available from: https://www.benchling.com/.

176.   *PureLink™ HiPure Plasmid DNA Purification Kits*. Thermo Fisher Scientific Inc., Darmstadt (Germany), 2015. Available at: https://www.thermofisher.com/document-connect/document-connect.html?url=https://assets.thermofisher.com/TFS-Assets%2FLSG%2Fmanuals%2Fpurelink_hipure_plasmid_qrc.pdf

177.   Untergasser, A. and H. Nijveen. *Primer3Plus*. 2007. [cited 04.10.2023]; Available from: https://www.bioinformatics.nl/cgi-bin/primer3plus/primer3plus.cgi.

178.   Untergasser, A., et al., *Primer3Plus, an enhanced web interface to Primer3.* Nucleic Acids Res, 2007. **35**(Web Server issue): p. W71-4.

179.   Synthego. *ICE CRISPR Analysis Tool*. 2023. [cited 04.10.2023]; Available from: https://www.synthego.com/products/bioinformatics/crispr-analysis.

180.   Schmid-Burgk, J.L., et al., *OutKnocker: a web tool for rapid and simple genotyping of designer nuclease edited cell lines.* Genome Res, 2014. **24**(10): p. 1719-23.

181.   RStudio Team. *RStudio: Integrated Development for R.* 2020. [cited 04.10.2023]; Available from: http://www.rstudio.com/.

182.   Kuut, G. *ELISA evaluation script*. 2020. [cited 04.10.2023]; Available from: https://github.com/Pestudkaru/Elisa-evaluation-script.

183.   *Pierce™ BCA Protein Assay Kit*. Thermo Fisher Scientific Inc., Rockford, IL (USA), 2020. accessed: 04.10.2023.[online]. Available at: https://assets.thermofisher.com/TFS-Assets/LSG/manuals/MAN0011430_Pierce_BCA_Protein_Asy_UG.pdf

184.   *NativePAGE™ Novex® Bis-Tris Gel System*. Life Technologies, Carlsbad, CA (USA), 2012. accessed: 04.10.2023.[online]. Available at: https://tools.thermofisher.com/content/sfs/manuals/nativepage_man.pdf

185.   *Agilent Seahorse XF Cell Mito Stress Test Kit*. Agilent Technologies Inc., Wilmington, DE (USA), 2019. accessed: 04.10.2023.[online]. Available at: https://www.agilent.com/cs/library/usermanuals/public/XF_Cell_Mito_Stres_Test_Kit_User_Guide.pdf

186.   Salabei, J.K., A.A. Gibb, and B.G. Hill, *Comprehensive measurement of respiratory activity in permeabilized cells using extracellular flux analysis.* Nature protocols, 2014. **9**(2): p. 421-438.

187.   *Agilent Seahorse XF Plasma Membrane Permeabilizer (PMP) Quickstart Guide*. Agilent Technologies Inc., Wilmington, DE (USA), 2017. accessed: 04.10.2023.[online]. Available at: https://www.agilent.com/cs/library/usermanuals/public/insert-xf-pmp-reagent-web.pdf

188.   *Agilent Seahorse XF Glycolysis Stress Test Kit*. Agilent Technologies Inc., Wilmington, DE (USA), 2019. accessed: 04.10.2023.[online]. Available at: https://www.agilent.com/cs/library/usermanuals/public/XF_Glycolysis_Stress_Test_Kit_User_Guide.pdf

189. Rath, S., et al., *MitoCarta3.0: an updated mitochondrial proteome now with sub-organelle localization and pathway annotations.* Nucleic Acids Res, 2021. **49**(D1): p. D1541-d1547.

190. Janjic, A., et al., *Prime-seq, efficient and powerful bulk RNA sequencing.* Genome Biology, 2022. **23**(1): p. 88.

191. Integrated DNA Technologies Inc. *RealTime qPCR Assay Entry*. 2023. [cited 04.10.2023]; Available from: https://eu.idtdna.com/scitools/Applications/RealTimePCR/.

192. Human Protein Atlas. *TBX21 Immune Cell Expression Data*. 2023. [cited 23.04.2023]; Available from: https://www.proteinatlas.org/ENSG00000073861-TBX21/immune+cell.

193. Wang, Y., et al., *M-CSF Induces Monocyte Survival by Activating NF-κB p65 Phosphorylation at Ser276 via Protein Kinase C.* PLOS ONE, 2011. **6**(12): p. e28081.

194. Platanias, L.C., *Mechanisms of type-I- and type-II-interferon-mediated signalling.* Nature Reviews Immunology, 2005. **5**(5): p. 375-386.

195. Human Protein Atlas. *C15orf48 Cell Line Expression Data*. 2020. [cited 14.10.2020]; Available from: https://www.proteinatlas.org/ENSG00000166920-C15orf48/cell.

196. Chavez, A., et al., *Highly efficient Cas9-mediated transcriptional programming.* Nat Methods, 2015. **12**(4): p. 326-8.

197. The ENCODE Project Consortium, *A user's guide to the encyclopedia of DNA elements (ENCODE).* PLoS Biol, 2011. **9**(4): p. e1001046.

198. The ENCODE Project Consortium, *An integrated encyclopedia of DNA elements in the human genome.* Nature, 2012. **489**(7414): p. 57-74.

199. Abascal, F., et al., *Expanded encyclopaedias of DNA elements in the human and mouse genomes.* Nature, 2020. **583**(7818): p. 699-710.

200. Rauluseviciute, I., et al., *JASPAR 2024: 20th anniversary of the open-access database of transcription factor binding profiles.* Nucleic Acids Research, 2023.

201. Doench, J.G., et al., *Optimized sgRNA design to maximize activity and minimize off-target effects of CRISPR-Cas9.* Nature Biotechnology, 2016. **34**(2): p. 184-191.

202. Sanson, K.R., et al., *Optimized libraries for CRISPR-Cas9 genetic screens with multiple modalities.* Nature Communications, 2018. **9**(1): p. 5416.

203. Tannahill, G.M., et al., *Succinate is an inflammatory signal that induces IL-1β through HIF-1α.* Nature, 2013. **496**(7444): p. 238-242.

204. de Kok, M.J.C., et al., *Circumventing the Crabtree effect in cell culture: A systematic review.* Mitochondrion, 2021. **59**: p. 83-95.

205. Wang, J., et al., *iCn3D, a web-based 3D viewer for sharing 1D/2D/3D representations of biomolecular structures.* Bioinformatics, 2020. **36**(1): p. 131-135.

206. Zhang, X., et al., *Methane limit LPS-induced NF-κB/MAPKs signal in macrophages and suppress immune response in mice by enhancing PI3K/AKT/GSK-3β-mediated IL-10 expression.* Scientific Reports, 2016. **6**(1): p. 29359.

207. Schioppa, T., et al., *Inhibition of Class I Histone Deacetylase Activity Blocks the Induction of TNFAIP3 Both Directly and Indirectly via the Suppression of Endogenous TNF-&alpha.* International Journal of Molecular Sciences, 2022. **23**(17): p. 9752.

208. Cogliati, S., et al., *Digitonin concentration is determinant for mitochondrial supercomplexes analysis by BlueNative page.* Biochimica et Biophysica Acta (BBA) - Bioenergetics, 2021. **1862**(1): p. 148332.

209. Tavoulari, S., et al., *The yeast mitochondrial pyruvate carrier is a hetero-dimer in its functional state.* Embo j, 2019. **38**(10).

210. Muri, J., et al., *Thioredoxin-1 distinctly promotes NF-κB target DNA binding and NLRP3 inflammasome activation independently of Txnip.* eLife, 2020. **9**: p. e53627.

211. Montalbetti, N., et al., *Mammalian iron transporters: Families SLC11 and SLC40.* Molecular Aspects of Medicine, 2013. **34**(2): p. 270-287.

212. Paradkar, P.N., et al., *Iron depletion limits intracellular bacterial growth in macrophages.* Blood, 2008. **112**(3): p. 866-874.

213. Winn, N.C., et al., *Myeloid-specific deletion of ferroportin impairs macrophage bioenergetics but is disconnected from systemic insulin action in adult mice.* Am J Physiol Endocrinol Metab, 2021. **321**(3): p. E376-e391.

214. de Arao Tan, I., C. Ricciardelli, and D.L. Russell, *The metalloproteinase ADAMTS1: A comprehensive review of its role in tumorigenic and metastatic pathways.* International Journal of Cancer, 2013. **133**(10): p. 2263-2276.

215. Danileviciene, V., et al., *The Role of C21orf91 in Herpes Simplex Virus Keratitis.* Medicina (Kaunas), 2019. **55**(12).

216. Foltz, D.R., et al., *The human CENP-A centromeric nucleosome-associated complex.* Nat Cell Biol, 2006. **8**(5): p. 458-69.

217. Rodriguez-Pascual, F. and T. Rosell-Garcia, *Lysyl Oxidases: Functions and Disorders.* J Glaucoma, 2018. **27 Suppl 1**: p. S15-s19.

218. Ruttkay-Nedecky, B., et al., *The role of metallothionein in oxidative stress.* Int J Mol Sci, 2013. **14**(3): p. 6044-66.

219. Castagliuolo, I., et al., *Neurotensin is a proinflammatory neuropeptide in colonic inflammation.* The Journal of Clinical Investigation, 1999. **103**(6): p. 843-849.

220. da Silva, L., et al., *Neurotensin downregulates the pro-inflammatory properties of skin dendritic cells and increases epidermal growth factor expression.* Biochim Biophys Acta, 2011. **1813**(10): p. 1863-71.

221. Wang, B., et al., *Fatty acid-binding protein 4 is a therapeutic target for septic acute kidney injury by regulating inflammatory response and cell apoptosis.* Cell Death & Disease, 2022. **13**(4): p. 333.

222. Hui, X., et al., *Adipocyte fatty acid-binding protein modulates inflammatory responses in macrophages through a positive feedback loop involving c-Jun NH2-terminal kinases and activator protein-1.* J Biol Chem, 2010. **285**(14): p. 10273-80.

223. Haro, H., et al., *Matrix metalloproteinase-7-dependent release of tumor necrosis factor-alpha in a model of herniated disc resorption.* J Clin Invest, 2000. **105**(2): p. 143-50.

224. Quarles, L.D., *FGF23, PHEX, and MEPE regulation of phosphate homeostasis and skeletal mineralization.* American Journal of Physiology-Endocrinology and Metabolism, 2003. **285**(1): p. E1-E9.

225. Aldo, P.B., et al., *Effect of culture conditions on the phenotype of THP-1 monocyte cell line.* Am J Reprod Immunol, 2013. **70**(1): p. 80-6.

226. Moullan, N., et al., *Tetracyclines Disturb Mitochondrial Function across Eukaryotic Models: A Call for Caution in Biomedical Research.* Cell Reports, 2015. **10**(10): p. 1681-1691.

227.   Takata, K., et al., *Induced-Pluripotent-Stem-Cell-Derived Primitive Macrophages Provide a Platform for Modeling Tissue-Resident Macrophage Differentiation and Function.* Immunity, 2017. **47**(1): p. 183-198.e6.

228.   Schmacke, N.A., et al., *IKKβ primes inflammasome formation by recruiting NLRP3 to the trans-Golgi network.* Immunity, 2022. **55**(12): p. 2271-2284.e7.

229.   Eubel, H., H.P. Braun, and A.H. Millar, *Blue-native PAGE in plants: a tool in analysis of protein-protein interactions.* Plant Methods, 2005. **1**(1): p. 11.

230.   Szczepanowska, K. and A. Trifunovic, *Tune instead of destroy: How proteolysis keeps OXPHOS in shape.* Biochimica et Biophysica Acta (BBA) - Bioenergetics, 2021. **1862**(4): p. 148365.

231.   Schmidt, C.A., K.H. Fisher-Wellman, and P.D. Neufer, *From OCR and ECAR to energy: Perspectives on the design and interpretation of bioenergetics studies.* Journal of Biological Chemistry, 2021. **297**(4).

232.   Sorouri, M., T. Chang, and D.C. Hancks, *Mitochondria and Viral Infection: Advances and Emerging Battlefronts.* mBio, 2022. **13**(1): p. e0209621.

233.   Pizarro-Cerdá, J. and P. Cossart, *Listeria monocytogenes: cell biology of invasion and intracellular growth*, in *Gram-Positive Pathogens*. 2019. Chapter 851-863.

234.   Nunez, N., et al., *The unforeseen intracellular lifestyle of Enterococcus faecalis in hepatocytes.* Gut Microbes, 2022. **14**(1): p. 2058851.

235.   Peyrusson, F., et al., *Intracellular Staphylococcus aureus persisters upon antibiotic exposure.* Nature Communications, 2020. **11**(1): p. 2200.

236.   Kracke, F., I. Vassilev, and J.O. Krömer, *Microbial electron transport and energy conservation - the foundation for optimizing bioelectrochemical systems.* Front Microbiol, 2015. **6**: p. 575.

237.   Galván-Peña, S., et al., *Malonylation of GAPDH is an inflammatory signal in macrophages.* Nat Commun, 2019. **10**(1): p. 338.

238.   Clayer, E., et al., *Severe Impairment of TNF Post-transcriptional Regulation Leads to Embryonic Death.* iScience, 2020. **23**(11): p. 101726.

239.   Rapino, F., et al., *C/EBPα induces highly efficient macrophage transdifferentiation of B lymphoma and leukemia cell lines and impairs their tumorigenicity.* Cell Rep, 2013. **3**(4): p. 1153-63.

8. LIST OF ABBREVIATIONS

Table 27. List of abbreviations.

Abbreviation	Description
AA	antimycin A
ADAM17	a disintegrin and metalloproteinase 17
ADAMTS1	a disintegrin and metalloproteinase with a thrombospondin motif 1
Ago	argonaut protein
AIM2	Absent In Melanoma 2
AP-1	activator protein 1
ASC	apoptosis-associated speck-like protein containing a CARD
ATP5	ATP synthase-coupling factor
Azide	potassium azide
BMDMs	bone marrow-derived macrophages
BN PAGE	Blue native PAGE
BSA	bovine serum albumin
CAA	2-Chloroacetamide
CARD	caspase recruitment domain
CARD8	CARD-containing protein 8
CBASS	cyclic nucleotide-based antiphage signaling system
CD	cluster of differentiation
CDH2	cadherin 2
CDS	coding sequence
CENPT	centromere protein T
cGAMP	cyclic GMP-AMP
cGAS	cyclic GMP-AMP synthetase
CI	complex I of the electron transport chain
CII	complex II of the electron transport chain
CIII	complex III of the electron transport chain
CIV	complex IV of the electron transport chain
ClpXP	ATP-dependent Clp protease
COX	cytochrome C oxidase subunit
CRISPRa	CRISPR activation
crRNA	crisprRNA
CTD	C-terminal domain
CTLA4	cytotoxic T-lymphocyte associated protein 4
CV	complex V of the electron transport chain
CXCL	CXC motif chemokine ligand
CXCR	CXC chemokine receptor
DAMP	damage-associated molecular pattern
DC	dendritic cell
dCas9-VPR	endonuclease-dead Cas9 fused to a hybrid VP64-p65-Rta transcriptional activator

Abbreviation	Description
DCs	dendritic cells
DDA	data-dependent acquisition
DMEM	Dulbecco's Modified Eagle Medium
dNTPs	deoxynucleotide triphosphates
Do	PBMC donor
dox	doxycycline
DPBS	Dulbecco's Phosphate Buffered Saline
dsDNA	double-stranded DNA
dsRNA	double-stranded RNA
ELISA	enzyme-linked immunosorbent assay
ETC	electron transport chain
ETI	effector triggered immunity
FABP4	fatty acid binding protein 4
FACS	fluorescence activated cell sorting
FCCP	Carbonyl cyanide 4-(trifluoromethoxy)phenylhydrazone
FCS	fetal calf serum
gp	glycoprotein
gRNA	guide RNA
GSDMD	gasdermin D
HAECs	human aortic endothelial cells
HIF-1α	hypoxia inducible factor 1α
HMW	high molecular weight
hs	human (homo sapiens)
HSC	hematopoietic stem cell
ICAM	intercellular adhesion molecule
ICE	Interference of CRISPR Edits
IFN	interferon
IFNAR	IFN-α/β receptor alpha chain
Ig	immunoglobulin
IKK	IκB kinase complex
IL	interleukin
IL-12R	IL-12 receptor
IL-1R	IL-1 receptor
IL-6R	IL-6 receptor
ILC	innate lymphoid cell
IMDM	Iscove's Modified Dulbecco's Medium
inj.	injection
IRAK	IL-1 receptor-activated protein kinase
IRF	interferon regulatory factor
IκB	inhibitor of nuclear factor B
JAK	Janus kinase

Abbreviation	Description
JNK	Jun N-terminal kinase
LGP2	laboratory of genetics and physiology 2
LONP	Lon protease
LOXL4	lysyl oxidase-like protein 4
LPS	lipopolysaccharide
LRR	leucin-rich repeat
M-CSF	Macrophage colony-stimulating factor
M1	classically activated
M2	alternatively activated
mAb	monoclonal antibody
MACS	magnetic-activated cell sorting
MAL	MyD88 adaptor-like protein
MAPK	mitogen-activated protein kinase
MAVS	mitochondrial antiviral signaling protein
MD2	myeloid differentiation factor 2
MDA5	melanoma differentiation-associated protein 5
MDMs	monocyte-derived macrophages
MEPE	matrix extracellular phosphoglycoprotein
MHC	major histocompatibility complex
MLS	mitochondrial localization signal
MMP7	matrix metalloproteinase 7
MPC	mitochondrial pyruvate carrier
MT	metallothionein
MT-ATP6	ATP synthetase subunit a
MT-ATP8	ATP synthetae protein 8
MT-ND2	NADH-ubiquinone oxidoreductase chain 2
MTCO	mitochondrially encoded cytochrome C oxidase subunit
mtROS	mitochondrial reactive oxygen species
MyD88	myeloid differentiation primary response gene 88
NDUFA11	NADH-ubiquinone oxidoreductase subunit A11
NDUFA4	cytochrome C oxidase subunit NDUFA4
NDUFA4L2	NDUFA4-like protein 2
NF-κB	nuclear factor kappa-light-chain-enhancer of activated B cells
NK cells	natural killer cells
NLR	nucleotide-binding domain, leucine-rich repeat-containing receptor
NLRC	NLR family CARD domain-containing protein
NLRP	NACHT, LRR and PYD domains-containing protein
NMES1	normal mucosa of esophagus-specific gene 1
nTPM	normalized transcripts per million
NTS	neurotensin
OAS	oligoadenylate synthetase

Abbreviation	Description
OASL	OAS like protein
Oligo	oligomycin A
OPA1	optic atrophy 1
OXPHOS	oxidative phosphorylation
pAb	polyclonal antibody
PAMP	pathogen-associated molecular pattern
PBMCs	peripheral blood mononuclear cells
PCR	polymerase chain reaction
PEI	Polyethylenimine HCl MAX
PKC	protein kinase C
PMA	phorbol 12-myristate 13-acetate
PRR	pattern recognition receptor
PVDF	polyvinylidene fluoride
PYD	pyrin domain
qPCR	quantitative PCR
RIG-I	retinoic acid-inducible gene I
RIPK	receptor-interacting serine/threonine protein kinase
RLR	RIG-I like receptor
RNAse L	ribonuclease L
RNAseq	RNA sequencing
RNP	ribonucleoproteins
ROS	reactive oxygen species
RPMI	Roswell Park Memorial Institute
RT	room temperature
SCAF1	supercomplex assembly factor 1
SD	standard deviation
SLC	solute carrier
SLC40A1	ferroportin-1
sqp	squirrel pox virus
STAT	signal transducer and activator of transcription
STING	stimulator of interferon genes
SYK	spleen tyrosine kinase
T/A/F	TMPD, ascorbate and FCCP
TAB	TAK1 binding protein
TAK1	TGF-β activated kinase 1
TASL	TLR adaptor interacting with SLC15A4 on the lysosome
TBK1	TANK-binding kinase 1
TBX21	T-box transcription factor 21
TCA	tricarboxylic acid
TCEP	Tris(2-carboxyethyl)phosphin
T_{FH}	T follicular helper cells

Abbreviation	Description
TGF-β	transforming growth factor-β
T_H cells	T helper cells
TIR domain	Toll-IL-1 receptor domain
TLR	toll-like receptor
TMEM	transmembrane protein
TMPD	N,N,N',N'-Tetramethyl-1,4-phenylendiamine
TNF	tumor necrosis factor α
TNFAIP	TNF-α induced protein
TNFR	TNF receptor
TRAF	TNF receptor associated factor
TRAM	TRIF related adaptor molecule
T_{reg}	regulatory T cells
TRIF	TIR domain containing adaptor protein inducing IFN-β
TSS	transcription start site
TXN	thioredoxin
UTR	untranslated region
VDAC	voltage-dependent anion channel
VHL	Von Hippel-Lindau tumor suppressor
wt	wildtype

9. LIST OF FIGURES

10. LIST OF TABLES

11. ACKNOWLEDGMENTS